Negative ions

Date: 23 Apr 2010
Satellite: Hubble Space Telescope
Depicts: Detail of the Carina Nebula

Negative ions

Formation of negative ions - **attachment**

Interaction of electrons with atoms and molecules

Photoelectron spectrometer

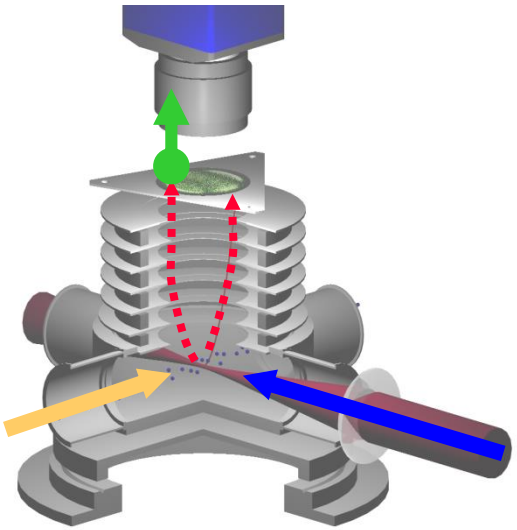

Photoelectron spectrum

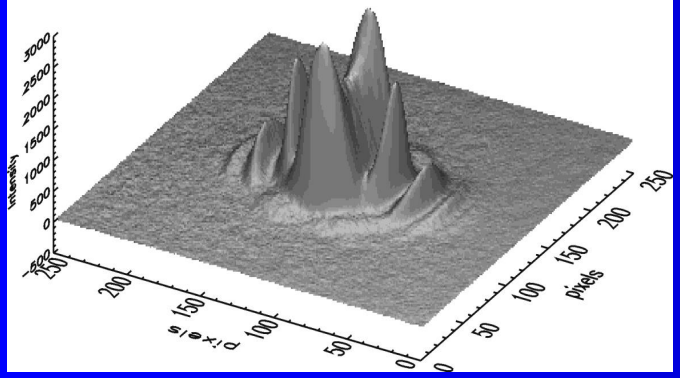

Date: 23 Apr 2010
Satellite: Hubble Space Telescope
Depicts: Detail of the Carina Nebula

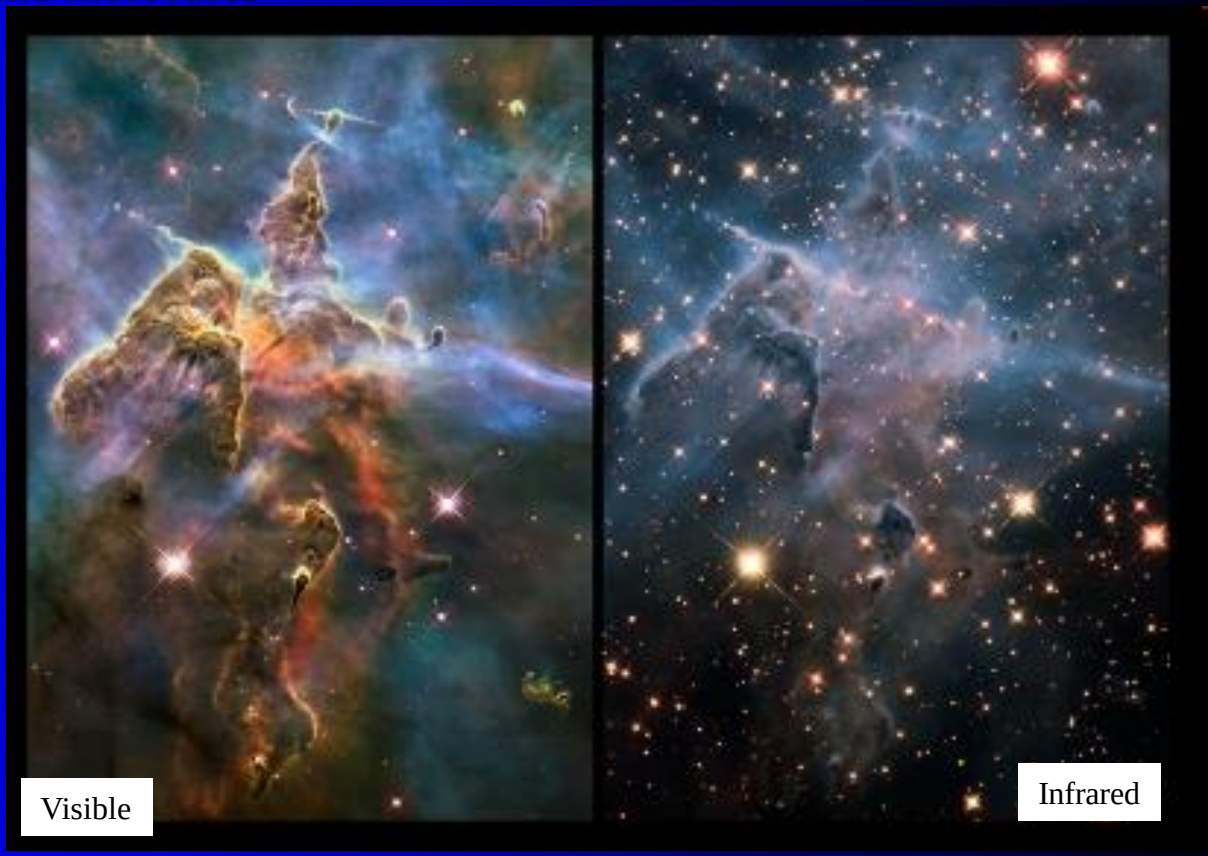

De Broglie wave length

$$\lambda = \frac{h}{p} = \frac{h}{mv}\sqrt{1 - \frac{v^2}{c^2}}$$

$$\lambda_e(4K) \sim 540\,A \sim 54x10^{-9}\,m$$

$$\lambda_e(1eV) \sim 11.6\,A \sim 1.16x10^{-9}\,m$$

$$\lambda_e(mK) \sim 3x10^{4}\,A \sim 3x10^{-6}\,m$$

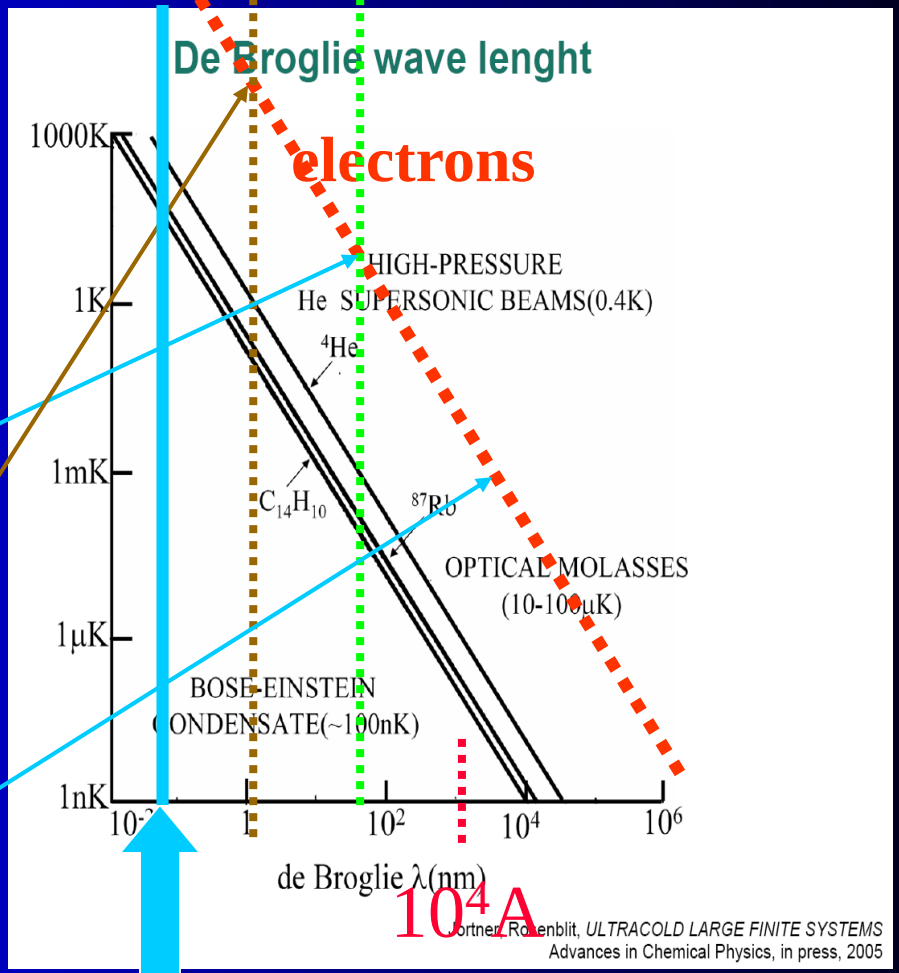

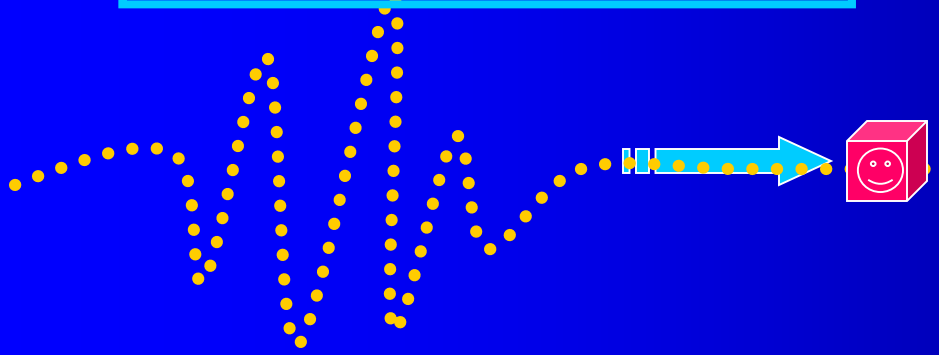

a_0

Jednorozměrný rozptyl

Parametry jsou E, V_0 , a

T+R=1

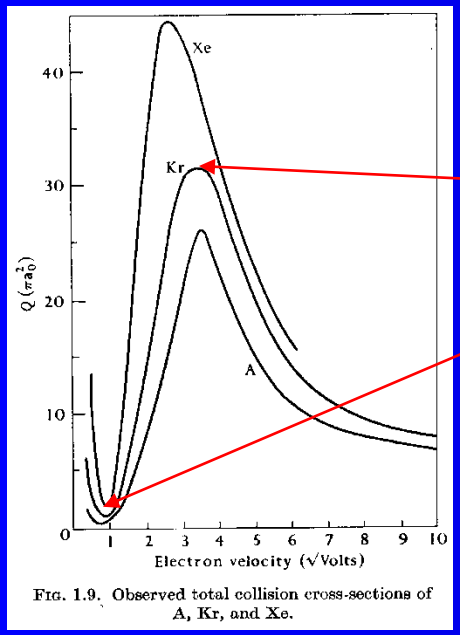

FIG. 1.9. Observed total collision cross-sections of A, Kr, and Xe.


Рис. 5.12. Диффузионное сечение столкновения электрона с атомом криптона.
Эксперимент (подвижность электронов при малых полях и температурах): [31]; [21]; [47]; [63].
Теория: [87].

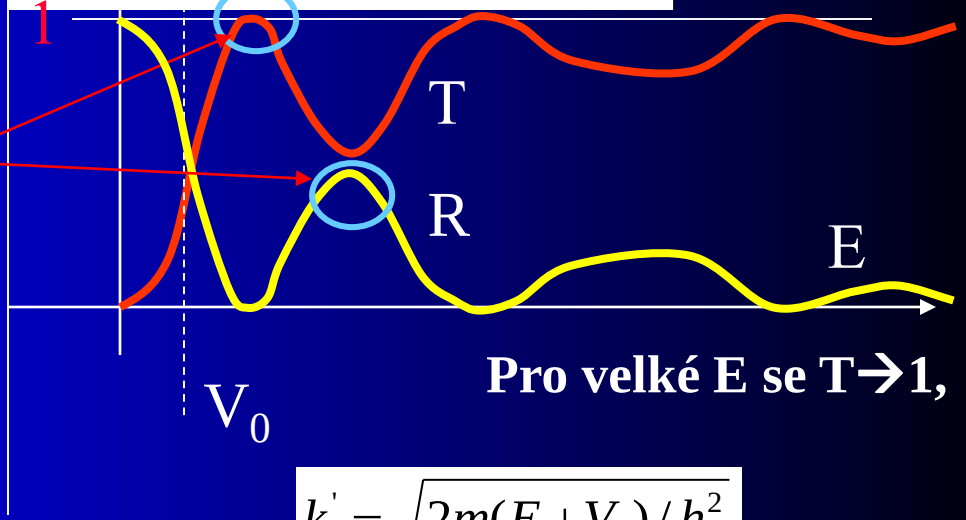

Pro velké E se T→1,

$$2k_n' n = n\pi$$

$$k' = \sqrt{2m(E+V_0)/h^2}$$

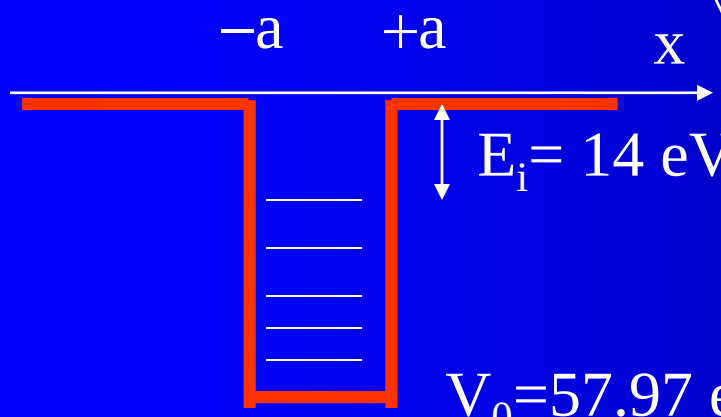

V_0=57.97 eV

Kr; a=2Å

E_i= 14 eV ➔ V_0=57.97 eV

E=0.013 V_0=0.75 eV

Kvantovka na každý deň

$H^+ + e^- + e^- \rightarrow H + e^-$

PRL 98, 133201 (2007) PHYSICAL REVIEW LETTERS week ending 30 MARCH 2007

Three-Body Recombination of Atomic Ions with Slow Electrons

S. X. Hu
Laboratory for Laser Energetics, University of Rochester, 250 East River Road, Rochester, New York 14623, USA

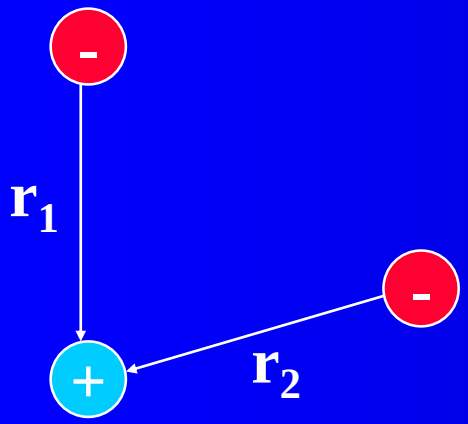

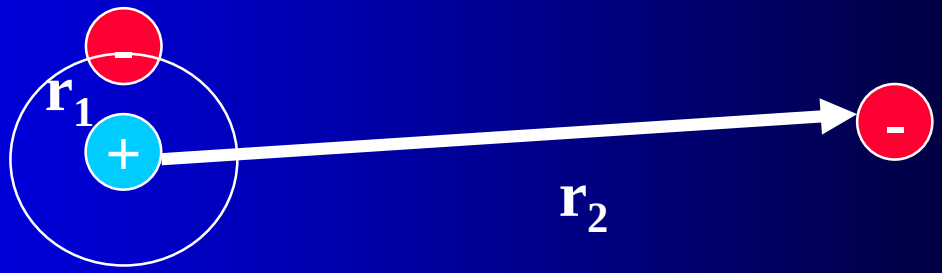

We consider the simplest TBR in the case of hydrogen formation, in which two free electrons interact with a proton. To investigate the three-body interaction dynamics, we numerically solve the six-dimensional (6D) time-dependent Schrödinger equation, which has the following form (atomic units are used throughout):

$$i\frac{\partial}{\partial t}\Phi(\mathbf{r}_1,\mathbf{r}_2,t)=\left[-\frac{1}{2}(\Delta_{\mathbf{r}_1}+\Delta_{\mathbf{r}_2})-\frac{1}{r_1}-\frac{1}{r_2}+\frac{1}{|\mathbf{r}_1-\mathbf{r}_2|}\right]\Phi(\mathbf{r}_1,\mathbf{r}_2,t), \quad (1)$$

where $\mathbf{r}_1$ and $\mathbf{r}_2$ are the position vectors of each electron, with respect to the proton. We obtain a more tractable with respect to the proton. We obtain a more tractable solution by using the close-coupling recipe [12]: expanding the 6D wave function $\Phi(\mathbf{r}_1,\mathbf{r}_2|t)$ in terms of bipolar spherical harmonics $Y^{LS}_{l_1l_2}(\Omega_1,\Omega_2)$, $\Phi(\mathbf{r}_1,\mathbf{r}_2|t)=\sum_{LS}\sum_{l_1l_2}[\Psi^{(LS)}_{l_1l_2}(r_1,r_2|t)/r_1r_2]Y^{LS}_{l_1l_2}(\Omega_1,\Omega_2)$, for a specific symmetry (LS). We can also expand the Coulomb repulsion term $1/|\mathbf{r}_1-\mathbf{r}_2|$ in terms of spherical harmonics. Substituting these expansions into the above Schrödinger Eq. (1) and integrating over the angles Ω_1 and Ω_2 yields a set of coupled partial differential equations with only two radial variables r_1 and r_2 left:

$$i\frac{\partial}{\partial t}\Psi_j(r_1,r_2|t)=[\hat{T}_1+\hat{T}_2+\hat{V}_c]\Psi_j(r_1,r_2|t)+\sum_k\hat{V}^I_{j,k}(r_1,r_2|t)\Psi_k(r_1,r_2|t), \quad (2)$$

where the partial-wave index j runs from 1 to the total number N of partial waves used for expansion. In Eq. (2),

Kvantovka na každý deň

$$i\frac{\partial}{\partial t}\Psi_j(r_1, r_2|t) = [\hat{T}_1 + \hat{T}_2 + \hat{V}_c]\Psi_j(r_1, r_2|t) + \sum_k \hat{V}^I_{j,k}(r_1, r_2|t)\Psi_k(r_1, r_2|t), \quad (2)$$

$H^+ + e^- + e^- \rightarrow H + e^-$

$$P_{nl}(E_2) = 2\sum_{LS}\sum_{l_2}\left|\int dr_1 \int dr_2 \phi^*_{nl}(r_1)\phi^*_{k_2 l_2}(r_2)\Psi^{(LS)}_{ll_2}(r_1, r_2, t = t_f)\right|^2,$$

K_E=0.1 eV

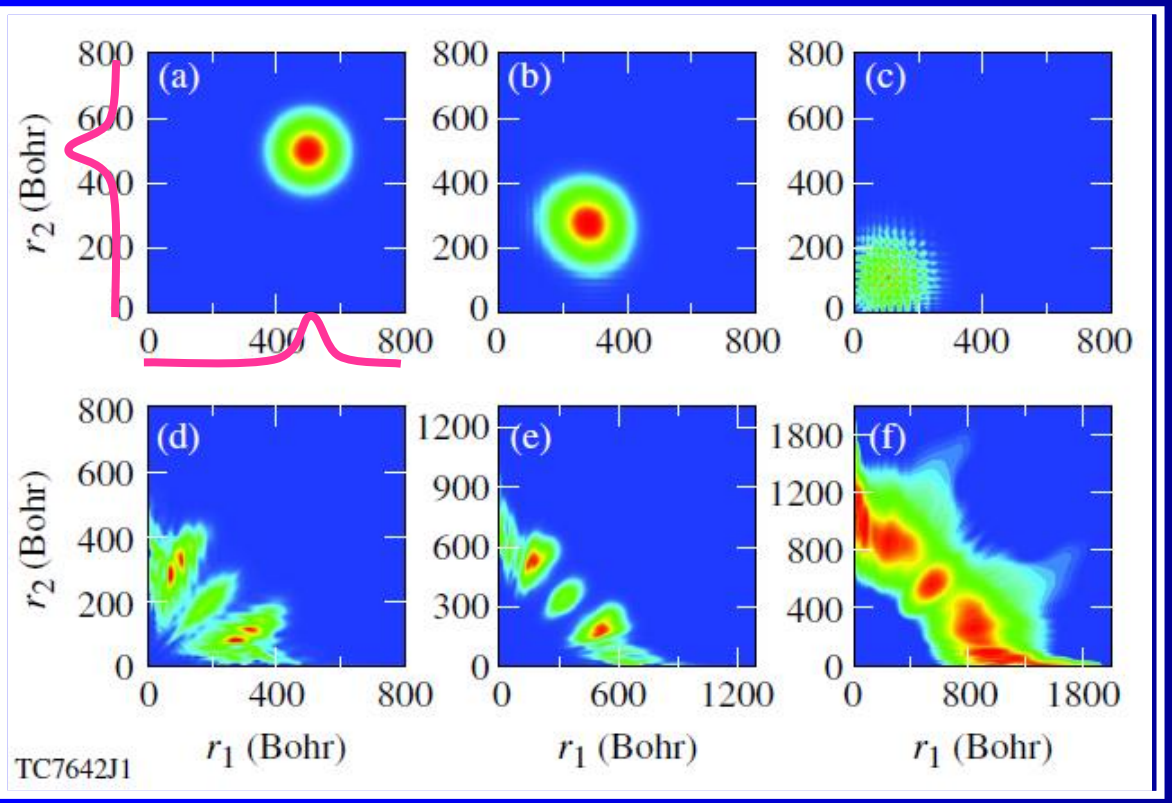

FIG. 1 (color online). Snapshots of electron probability distribution on the plane spanned by the radial coordinates r_1 and r_2 for different times: (a) $t = 0.0$ fs, (b) $t = 60$ fs, (c) $t = 100$ fs, (d) $t = 150$ fs, (e) $t = 194$ fs, and (f) (in log scale) $t = 260$ fs.

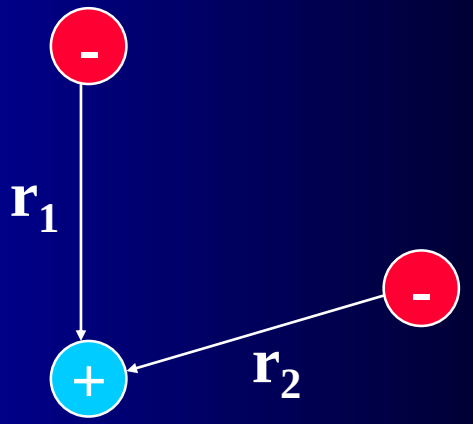

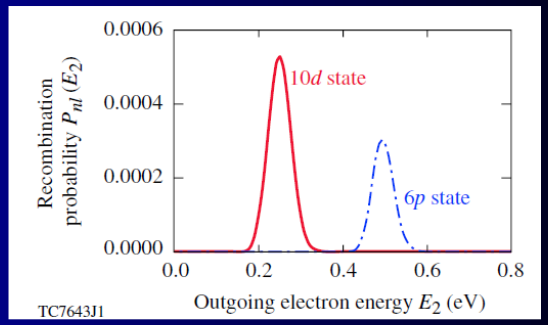

Thus, for the case of $K_E = 0.1$ eV considered in Figs. 1 and 2, the total system energy is about $E_{tot} \sim 0.12$ eV instead of $2K_E$. Hence, when one electron recombines to the 10d state ($|E_{10d}| \approx 0.136$ eV) of the H atom, the outgoing electron takes an initial total energy of 0.12 eV plus $|E_{10d}|$, thereby $P_{10d}(E_2)$ peaks at $E_2 \sim 0.256$ eV, as shown by the (red) solid line of Fig. 2. Similar energy conservation is also well satisfied for the recombination to the 6p state, as is illustrated by the (blue) dash-dotted line in Fig. 2. Our quantum calculations unambiguously reveal the essential feature of a TBR process.

Kvantovka na každý deň

$H^+ + e^- + e^- \rightarrow H + e^-$

$K_E = 0.1$ eV

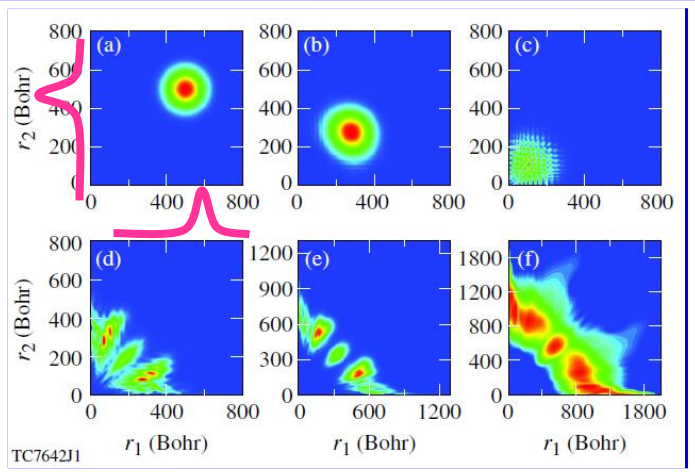

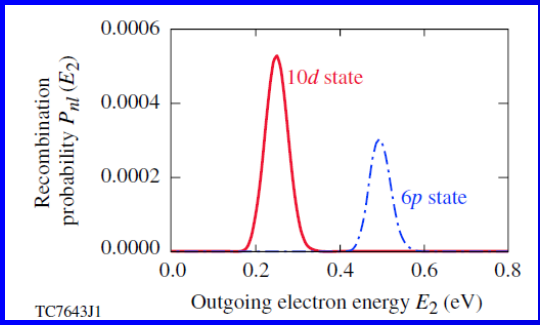

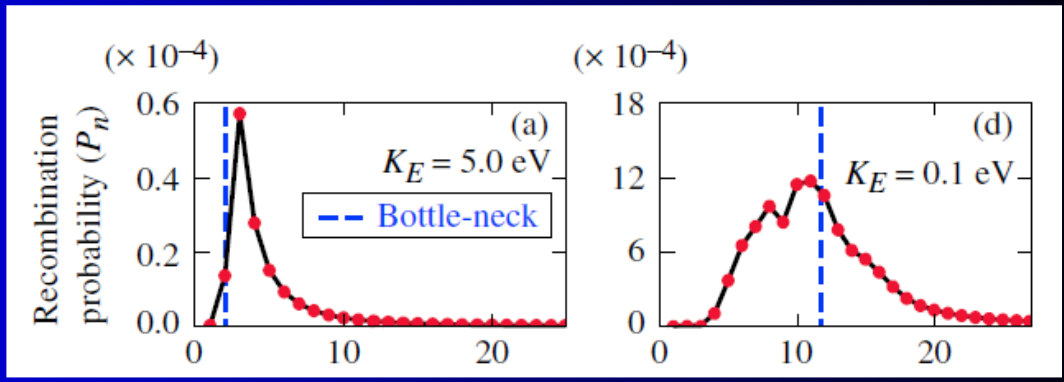

FIG. 3 (color online). The recombination probability P_n as a function of the energy level n, for different electron kinetic energies K_E marked in each panel.

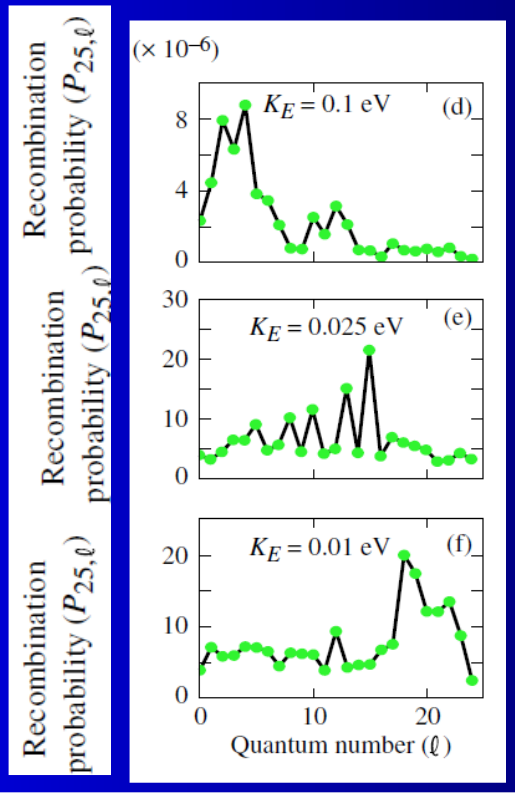

FIG. 4 (color online). The recombination probability $P_{n=25,l}$ as a function of the angular-momentum quantum number l, for different electron kinetic energies K_E marked in each panel.

Negative ions 2006

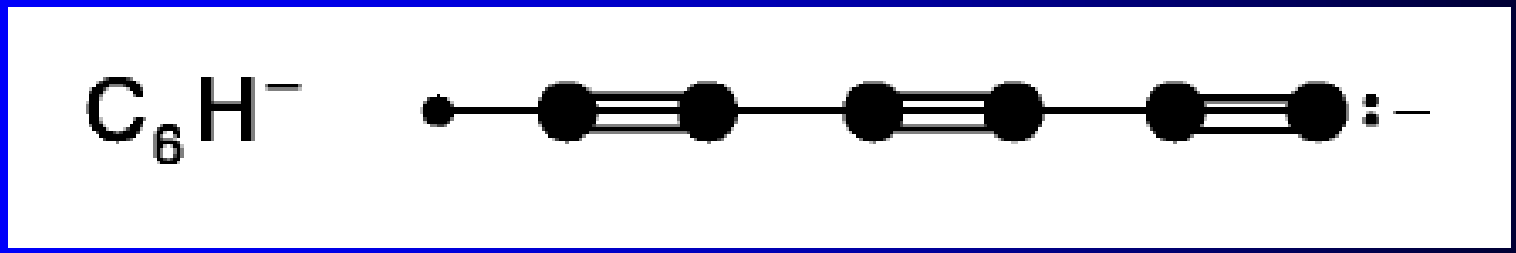

THE ASTROPHYSICAL JOURNAL, 652: L141–L144, 2006 December 1

LABORATORY AND ASTRONOMICAL IDENTIFICATION OF THE NEGATIVE MOLECULAR ION C_6H^-

M. C. MCCARTHY,[1] C. A. GOTTLIEB,[1] H. GUPTA,[1,2] AND P. THADDEUS[1]

Received 2006 September 28; accepted 2006 October 17; published 2006 November 20

ABSTRACT

The negative molecular ion C_6H^- has been detected in the radio band in the laboratory and has been identified in the molecular envelope of IRC +10216 and in the dense molecular cloud TMC-1. The spectroscopic constants derived from laboratory measurements of 17 rotational lines between 8 and 187 GHz are identical to those derived from the astronomical data, establishing unambiguously that C_6H^- is the carrier of the series of lines with rotational constant 1377 MHz first observed by K. Kawaguchi et al. in IRC +10216. The column density of C_6H^- toward both sources is 1%–5% that of neutral C_6H. These surprisingly high abundances for a negative ion imply that if other molecular anions are similarly abundant with respect to their neutral counterparts, they may be detectable both in the laboratory at high resolution and in interstellar molecular clouds.

Note added in proof.—A third member in the series, C_4H^-, has now been detected in the laboratory at centimeter and millimeter wavelengths. A full account of this work will be presented elsewhere.

Interstellar Molecules

2 atoms	3 atoms	4 atoms	5 atoms	6 atoms	7 atoms	8 atoms	9 atoms	10 atoms	11 atoms	12 atoms	13 atoms
H_2	C_3*	c-C_3H	C_5*	C_5H	C_6H	CH_3C_3N	CH_3C_4H	CH_3C_5N	HC_9N	C_6H_6	$HC_{11}N$
AlF	C_2H	l-C_3H	C_4H	l-H_2C_4	CH_2CHCN	$HC(O)OCH_3$	CH_3CH_2CN	$(CH_3)_2CO$	CH_3C_6H	$C_2H_5OCH_3$	
AlCl	C_2O	C_3N	C_4Si	C_2H_4*	CH_3C_2H	CH_3COOH	$(CH_3)_2O$	$(CH2OH)_2$	C_2H_5OCHO	n-C_3H_7CN	
C_2**	C_2S	C_3O	l-C_3H_2	CH_3CN	HC_5N	C_7H	CH_3CH_2OH	CH_3CH_2CHO			
CH	CH_2	C_3S	c-C_3H_2	CH_3NC	CH_3CHO	H_2C_6	HC_7N				
CH^+	HCN	C_2H_2*	H2CCN	CH_3OH	CH_3NH_2	CH_2OHCHO	C_8H				
CN	HCO	NH_3	CH_4*	CH_3SH	c-C_2H_4O	l-HC_6H*	$CH_3C(O)NH_2$				
CO	HCO^+	HCCN	HC_3N	HC_3NH^+	H_2CCHOH	CH_2CHCHO	C_8H^-				
CO^+	HCS^+	$HCNH^+$	HC_2NC	HC_2CHO	C_6H^-	CH_2CCHCN	C_3H_6				
CP	HOC^+	HNCO	HCOOH	NH_2CHO		H_2NCH_2CN					
SiC	H_2O	HNCS	H_2CNH	C_5N							
HCl	H_2S	$HOCO^+$	H_2C_2O	l-HC_4H*		Cations					
KCl	HNC	H_2CO	H_2NCN	l-HC_4N							
NH	HNO	H_2CN	HNC_3	c-H_2C_3O		Anions					
NO	MgCN	H_2CS	SiH_4*	H_2CCNH							
NS	MgNC	H_3O^+	H_2COH^+	C_5N^-							
NaCl	N_2H^+	c-SiC_3	C_4H^-								
OH	N_2O	CH_3*	HC(O)CN								
PN	NaCN	C_3N^-									
SO	OCS	PH3									
SO^+	SO_2	HCNO									
SiN	c-SiC_2	HOCN									
SiO	CO_2*	HSCN									
SiS	NH_2										
CS	H_3^+*										
HF	H_2D^+										
SH*	HD_2^+										
HD	SiCN										
FeO	AlNC										
O_2	SiNC										
CF^+	HCP										
SiH	CCP										
PO											
AlO											

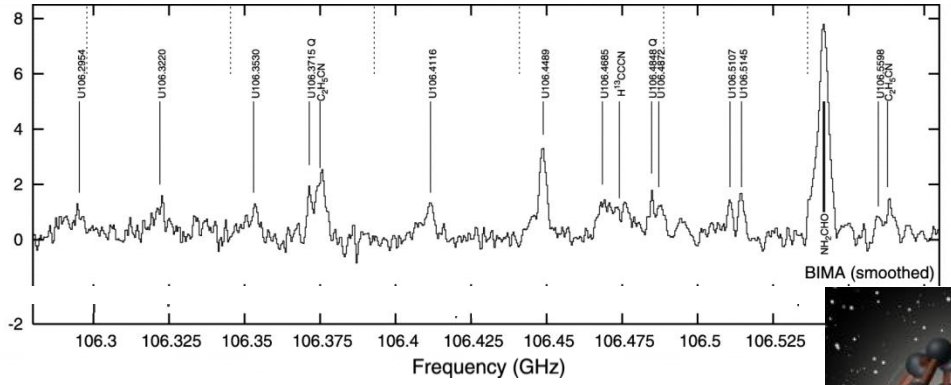

Friedel et al., ApJ 600, 234 (2004)

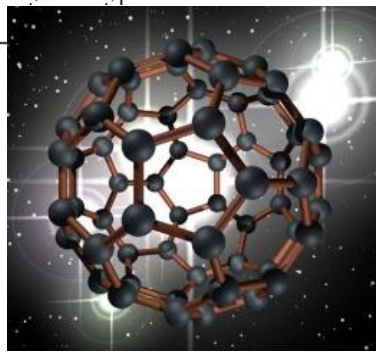

Very low collision energies

$$Kr(^1S_0) + \hbar\omega \rightarrow Kr^+(^2P_{1/2}) + e^-(\varepsilon)$$

$$e^- + SF_6 \rightarrow SF_6^{-*}$$

$$e^- + CCl_4 \rightarrow CCl_4^{-*} \rightarrow CCl_3 + Cl^-$$

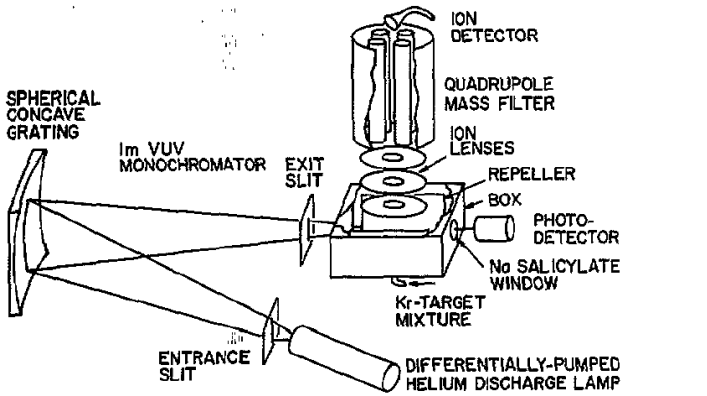

Figure 1. Schematic diagram of the VUV photoionization apparatus used for attachment studies (Chutjian and Alajajian 1985a, b).

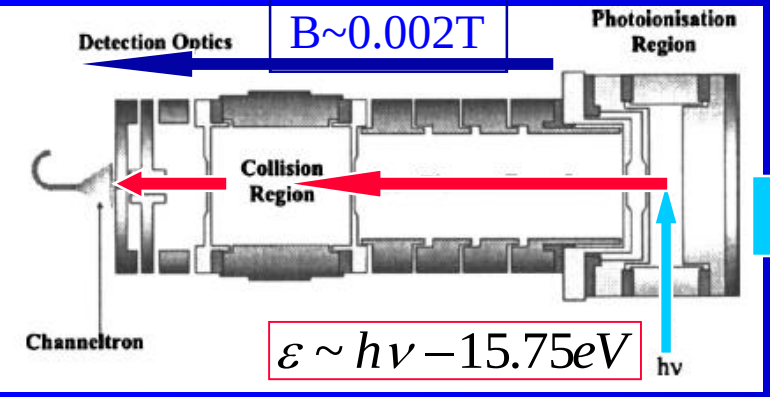

TOPICAL REVIEW

J. Phys. B: At. Mol. Opt. Phys. 28 (1995) 1645–1672. Printed in the UK

Electron–molecule collisions at very low electron energies

F B Dunning

Department of Physics and the Rice Quantum Institute, Rice University, PO Box 1892, Houston, TX 77251, USA

10^5 Å

1995

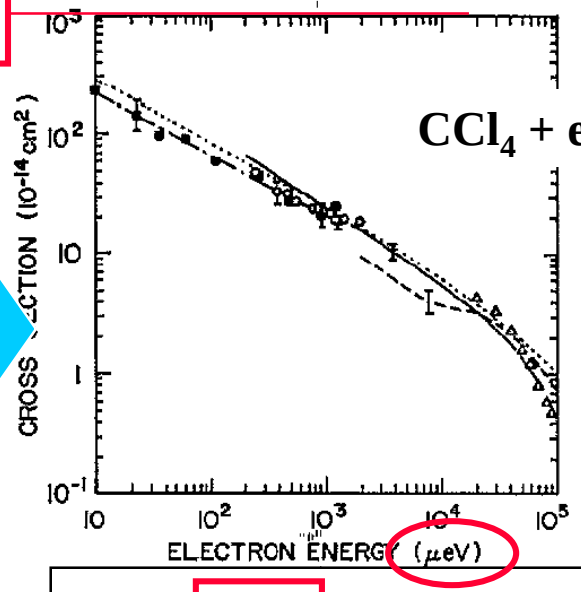

$CCl_4 + e(\varepsilon) \rightarrow Cl^- + \ldots$

10^3 Å^2

2004

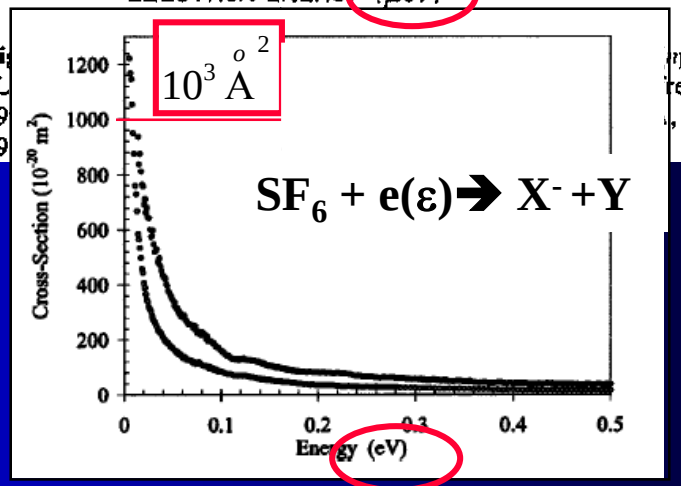

$SF_6 + e(\varepsilon) \rightarrow X^- + Y$

Negative ions

Interaction of electrons with atoms and molecules

Formation of negative ions **attachment**

Existence of negative ions

It is in case of H- second electron in the field of proton and first electron

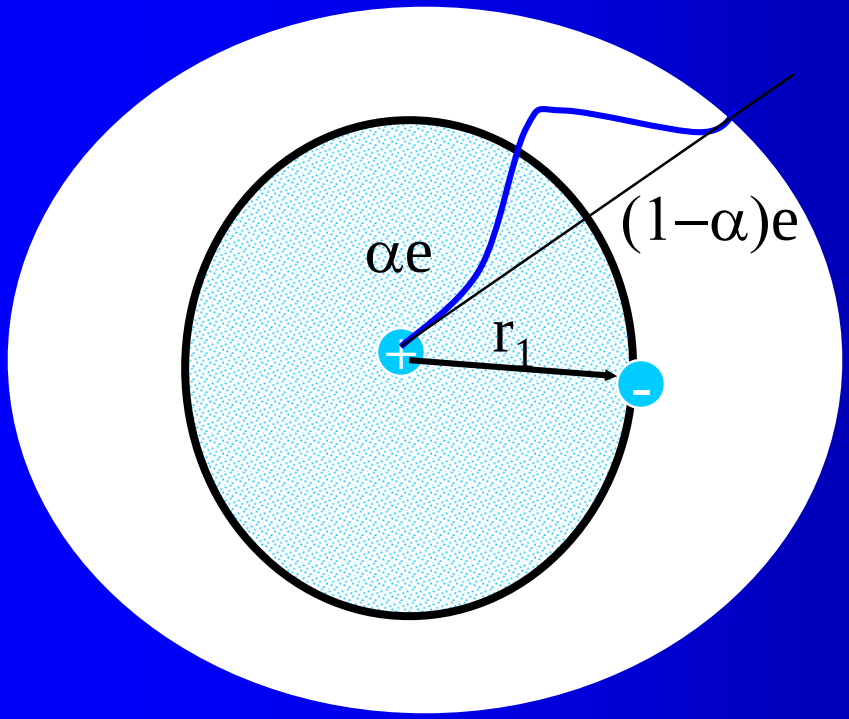

$+e$ $\quad -\alpha e$

$$V_{within} = -(1-\alpha)e/r_1$$

$\beta < 1$

$$V_{out} = \beta(1-\alpha)e/r_1$$

Total potential energy of electron of the charge -e

$$U(r_1)_{total} = -(1-\beta)(1-\alpha)e^2/r_1$$

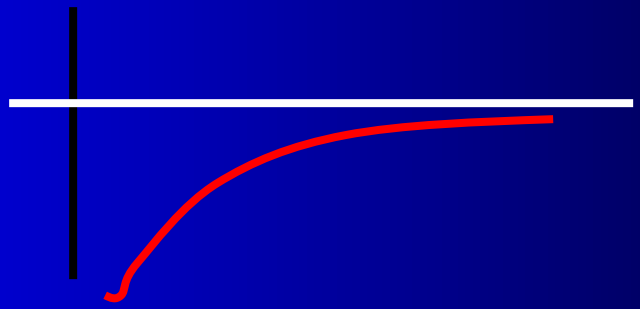

Calculation of H^- potential

The calculation of the potential energy of an electron in the field of a hydrogen atom may be carried out to a first approximation as follows. If we neglect polarization effects (which are actually decisive in determining the stability of H^-) the probability of finding the atomic electron at a distance between r and $r + dr$ from the nucleus is $4\pi r^2 \psi^2 \, dr$, where $\psi = (\pi a_0^3)^{-1/2} \exp(-r/a_0)$ is the wave function of the ground state of hydrogen. The potential energy due to the atomic electron at a point distant r_1 from the nucleus is

$$\frac{4\pi e^2}{r_1} \int_0^{r_1} \psi^2 r^2 \, dr + 4\pi e^2 \int_{r_1}^{\infty} \frac{\psi^2 r^2}{r} \, dr,$$

the first term arising from the charge within r_1, the second from that without. Carrying out the elementary integrations involved gives

$$e^2 \left\{ \frac{1}{r_1} - \exp(-2r_1/a_0) \left(\frac{1}{r_1} + \frac{1}{a_0} \right) \right\}.$$

Adding the potential energy $-e^2/r_1$ due to the nucleus we find for the total potential energy

$$-e^2 \exp(-2r_1/a_0) \left(\frac{1}{r_1} + \frac{1}{a_0} \right). \qquad (1.1)$$

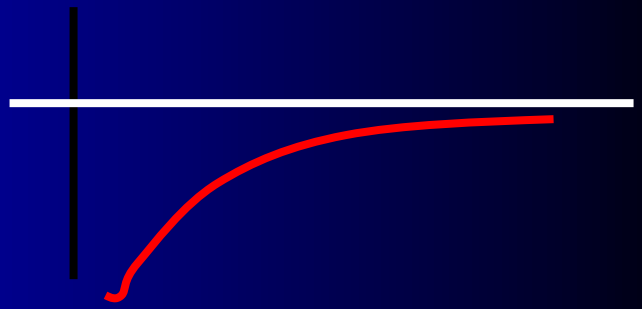

Electron Affinity : Attraction of e^- to neutral atom kJ/mol

96kJ/mol~1eV

Exceptions: Be **(EA < 0)**, N **(EA < 0)**

|EA(Cl)| > |EA(F)| ?

Small F atom, greater e^- repulsion

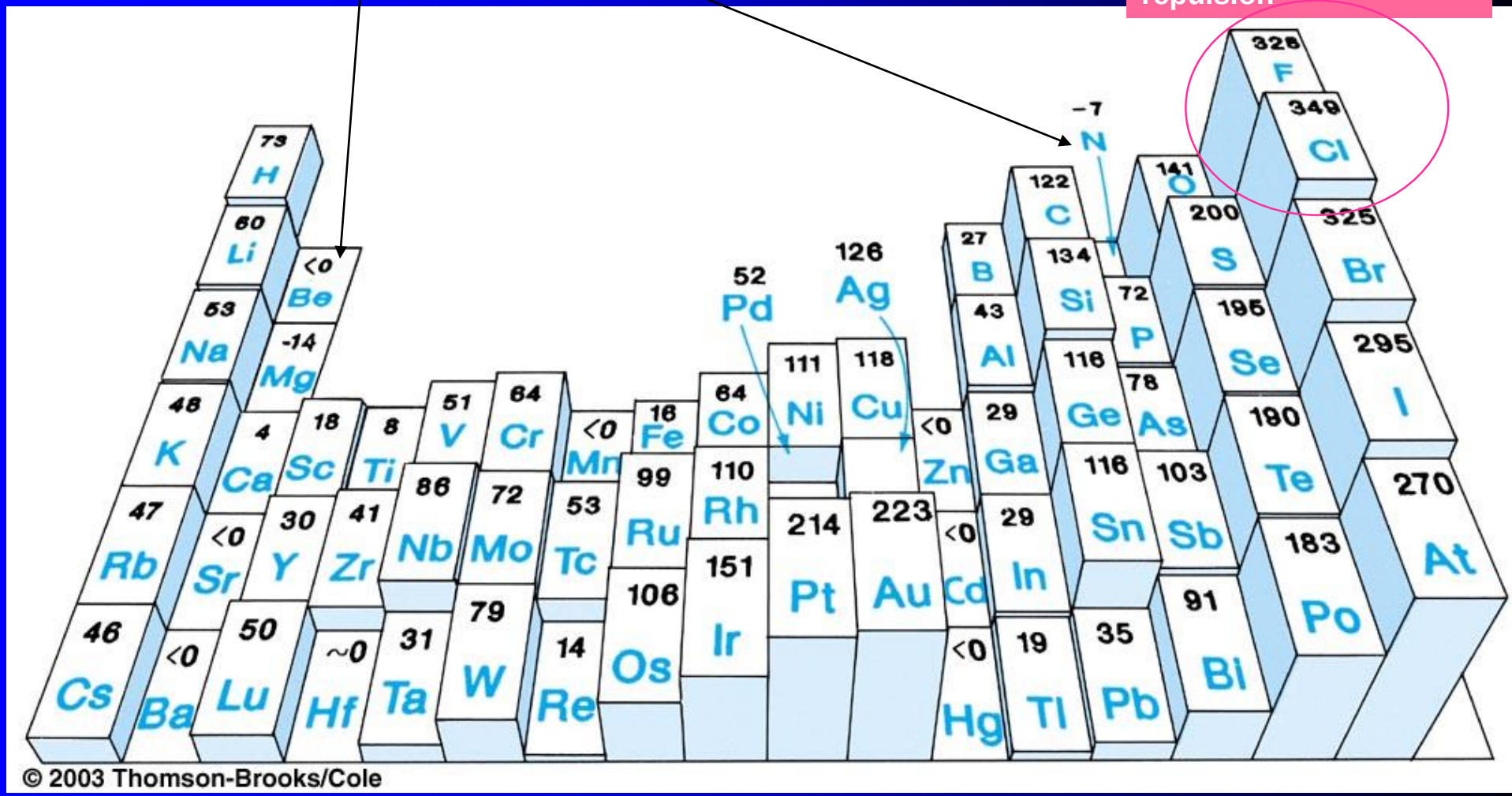

Attachment (to molecule) and detachment

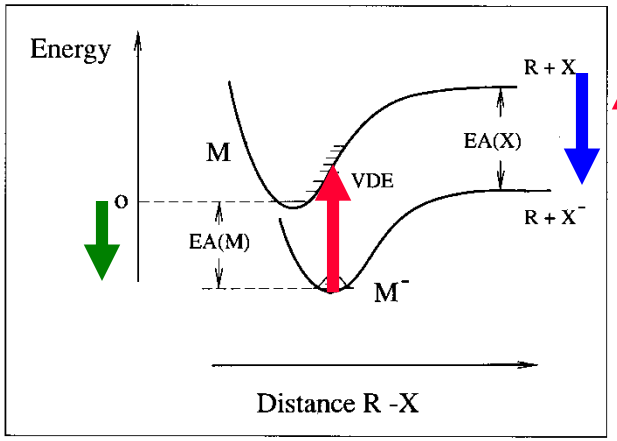

Fig. 1.1. Born-Oppenheimer potential energy curves illustrating electron affinity (EA) and vertical detachment energy (VDE).

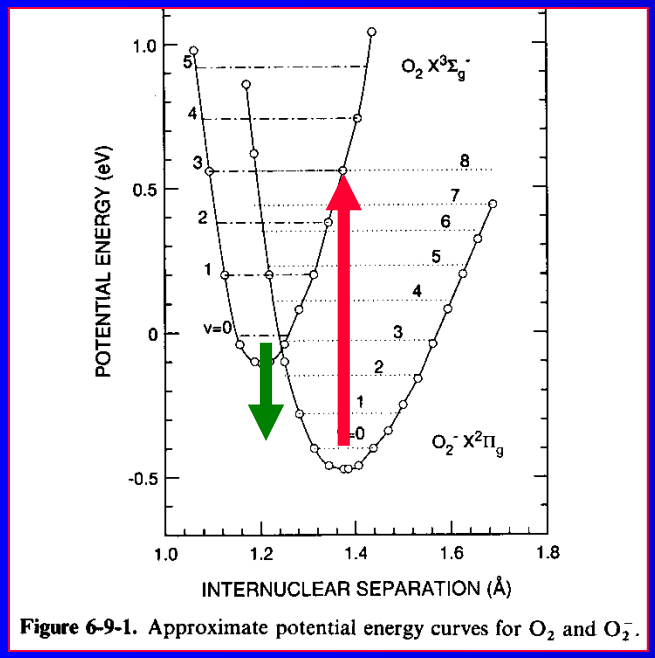

Figure 6-9-1. Approximate potential energy curves for O_2 and O_2^-.

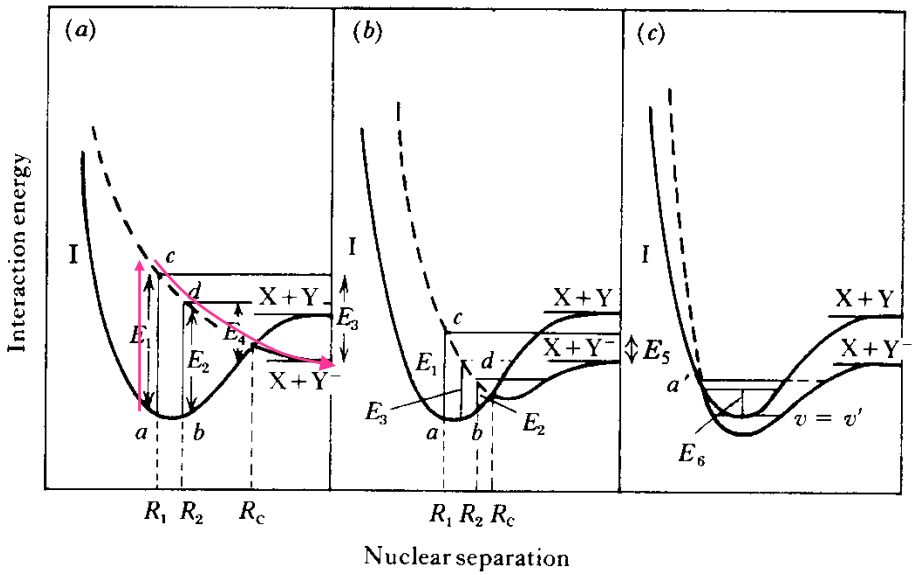

Fig. 9.1. Potential-energy curves illustrating three possible ways in which negative ions may be formed from a molecule XY by electron capture.

Vibrational predissociation

Figure 1.10 illustrates vibrational predissociation. The coordinates Q_1 and Q_2 represent different molecular motions in a polyatomic molecule. The anion M^- formed on electron attachment has sufficient energy to dissociate but the energy is initially in vibrational modes that do not correspond to the reaction coordinate Q_2.

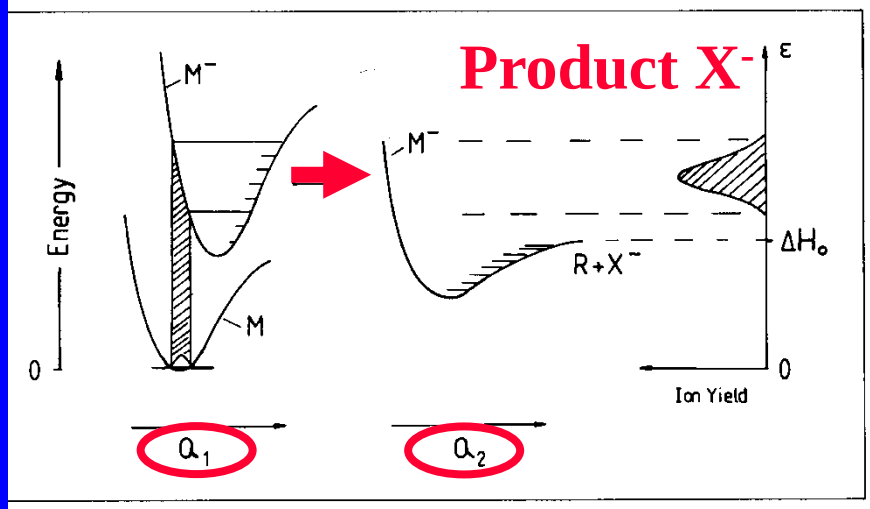

Fig. 1.10. Schematic potential energy curves illustrating dissociative electron attachment via vibrational predissociation. Q_1 and Q_2 represent different motions in a polyatomic ion.

Hydrogen molecule

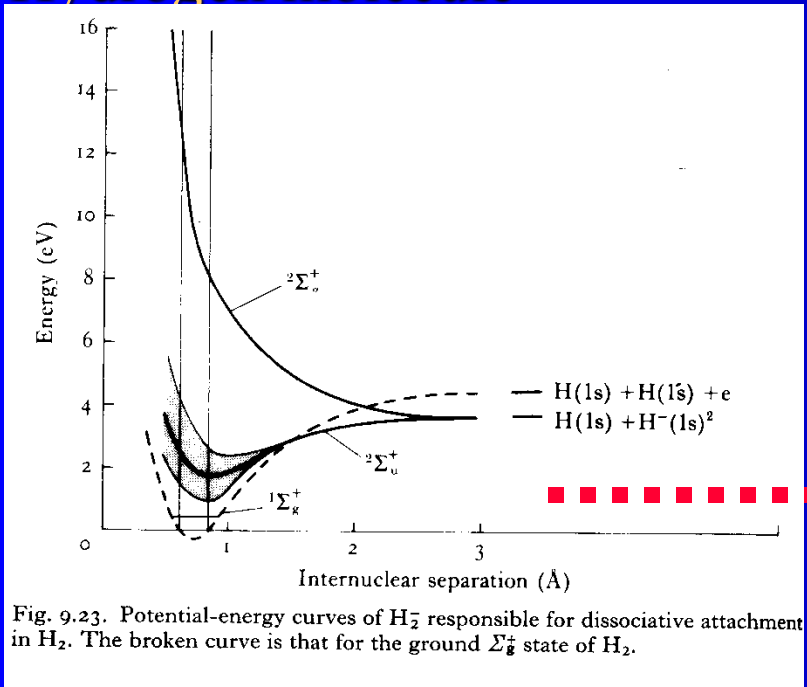

Fig. 9.23. Potential-energy curves of H_2^- responsible for dissociative attachment in H_2. The broken curve is that for the ground Σ_g^+ state of H_2.

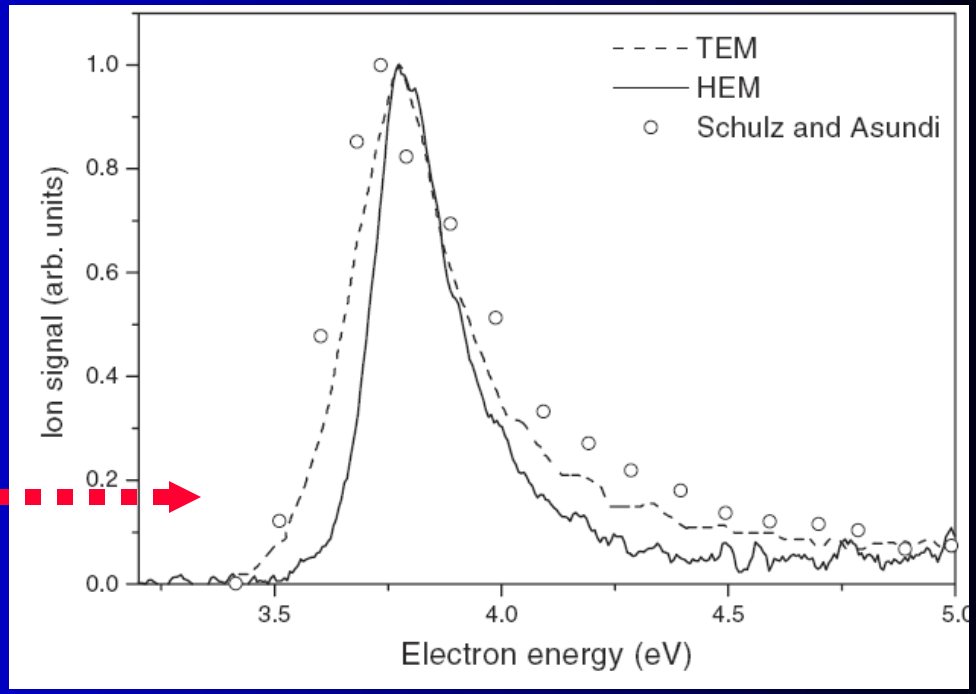

The discovery of large concentrations of H− ions (30%) in low-temperature hydrogen plasmas [1] has provided the possibility of producing intense beams of H− ion sources for neutral beam heating [2, 3] of thermonuclear fusion devices [4, 5]. Modelling of such plasmas requires a detailed knowledge of the mechanism of dissociative electron attachment (DEA) of electrons to molecular hydrogen. Schematically the process may be written as a two-step process:

$$e^- + H_2(v, J) \rightarrow H_2^- \rightarrow H^- + H$$

where v and J denote the vibrational and rotational quantum numbers of the target hydrogen molecule. The incident electron is trapped by the neutral molecule in a resonant state, this trapping increasing the electron residence time sufficiently to allow the relatively slow moving nuclei to dissociate. In the present case the H_2^- $(1\sigma_g^2\, 1\sigma_u^2 + {}^2\Sigma_u^+)$ resonance formed at a range of electron energies of around 4 eV is characterized by a very short lifetime against autodetachment when formed from the $v = 0$ level. Hence the cross section for product H− is low.

Hydrogen molecule EA calculated by J. Horacek

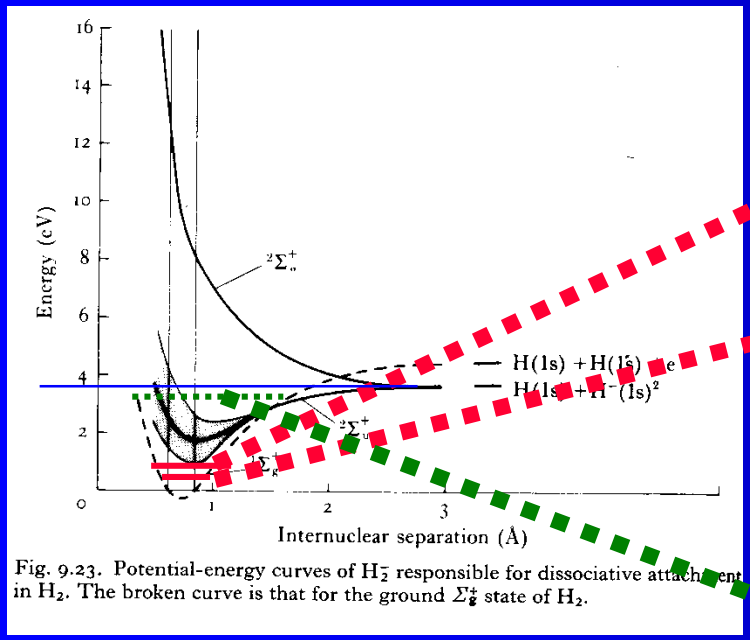

Fig. 9.23. Potential-energy curves of H_2^- responsible for dissociative attachment in H_2. The broken curve is that for the ground Σ_g^+ state of H_2.

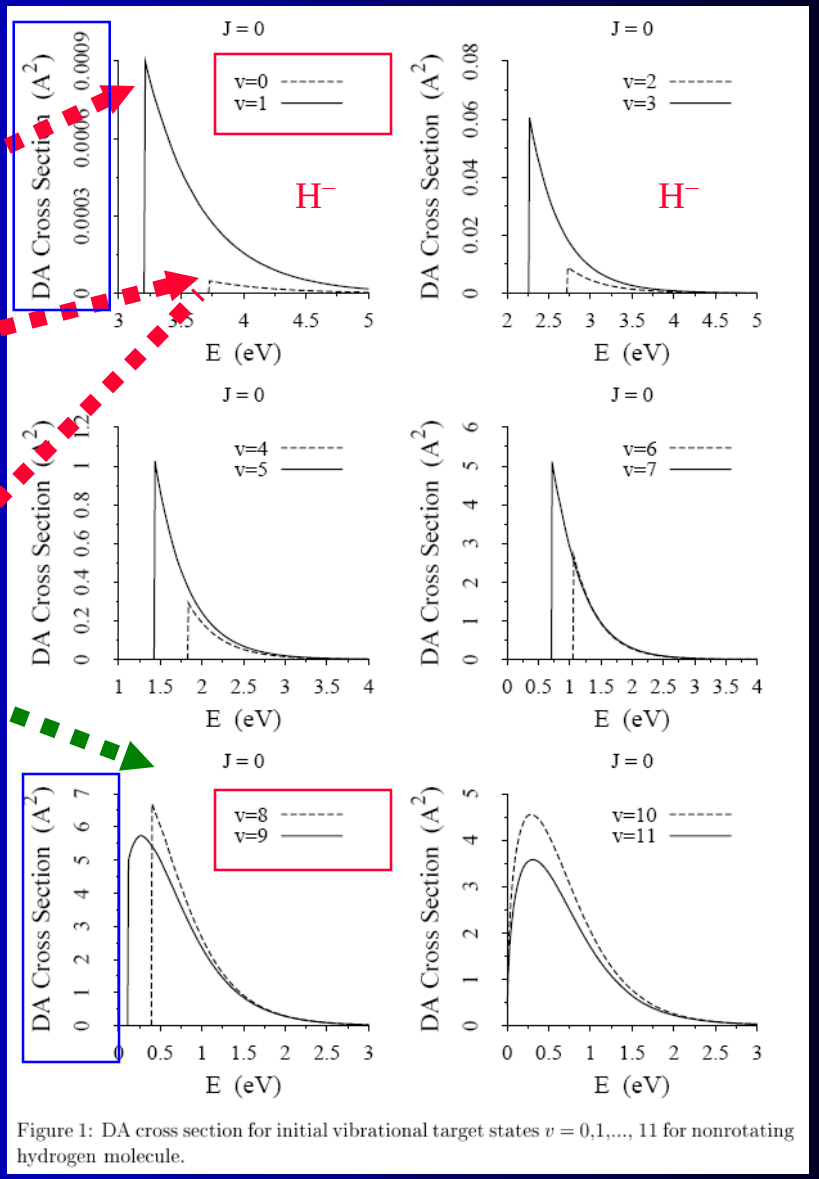

Figure 1: DA cross section for initial vibrational target states $v = 0,1,...,11$ for nonrotating hydrogen molecule.

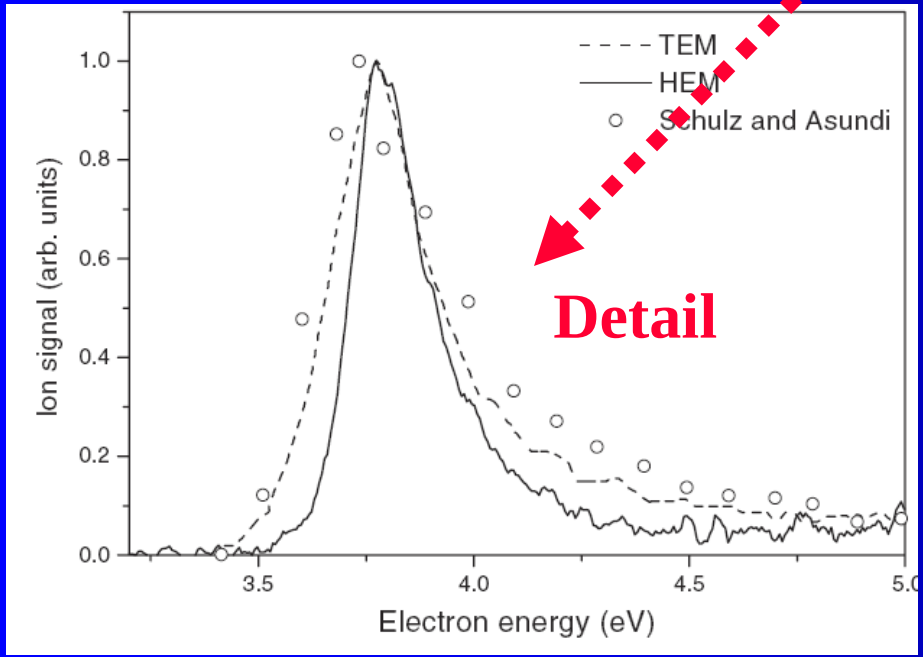

Vibrational excitation of H_2

$e^- + H_2(v, J) \rightarrow H_2^- \rightarrow H^- + H$

Hydrogen molecule

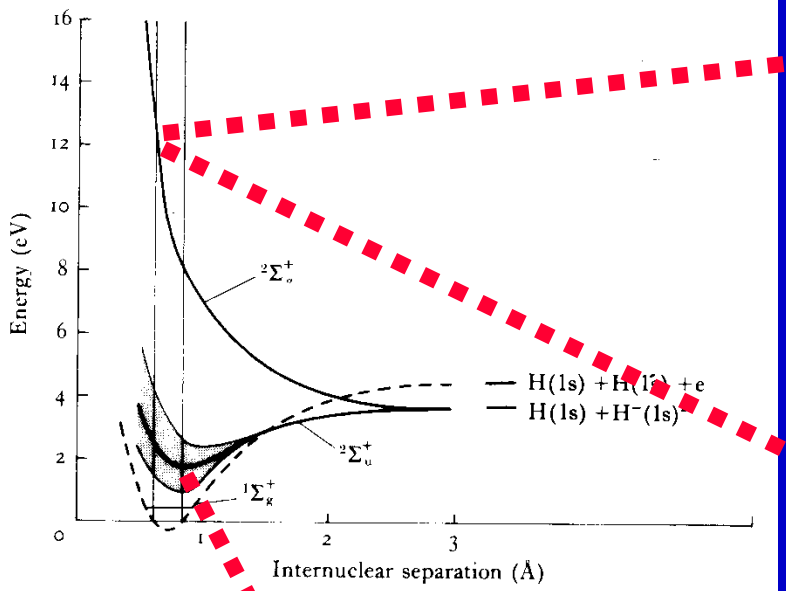

Fig. 9.23. Potential-energy curves of H_2^- responsible for dissociative attachment in H_2. The broken curve is that for the ground Σ_g^+ state of H_2.

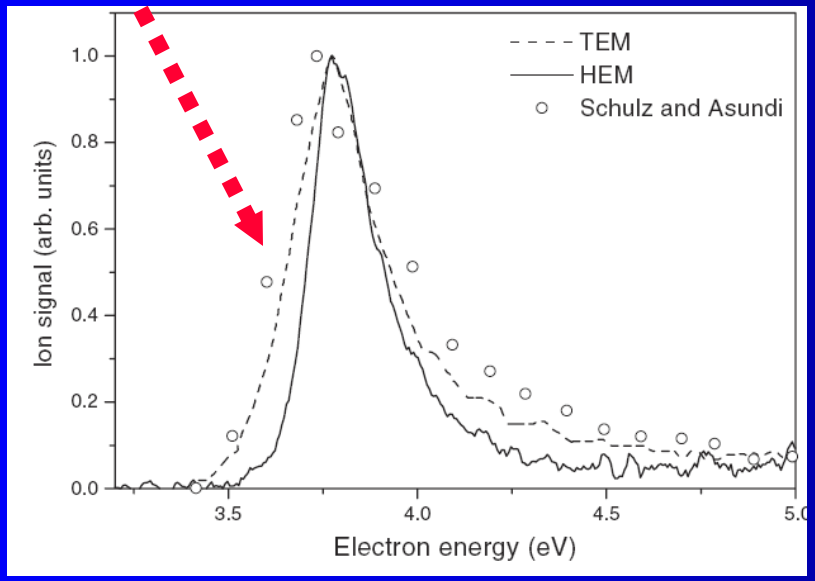

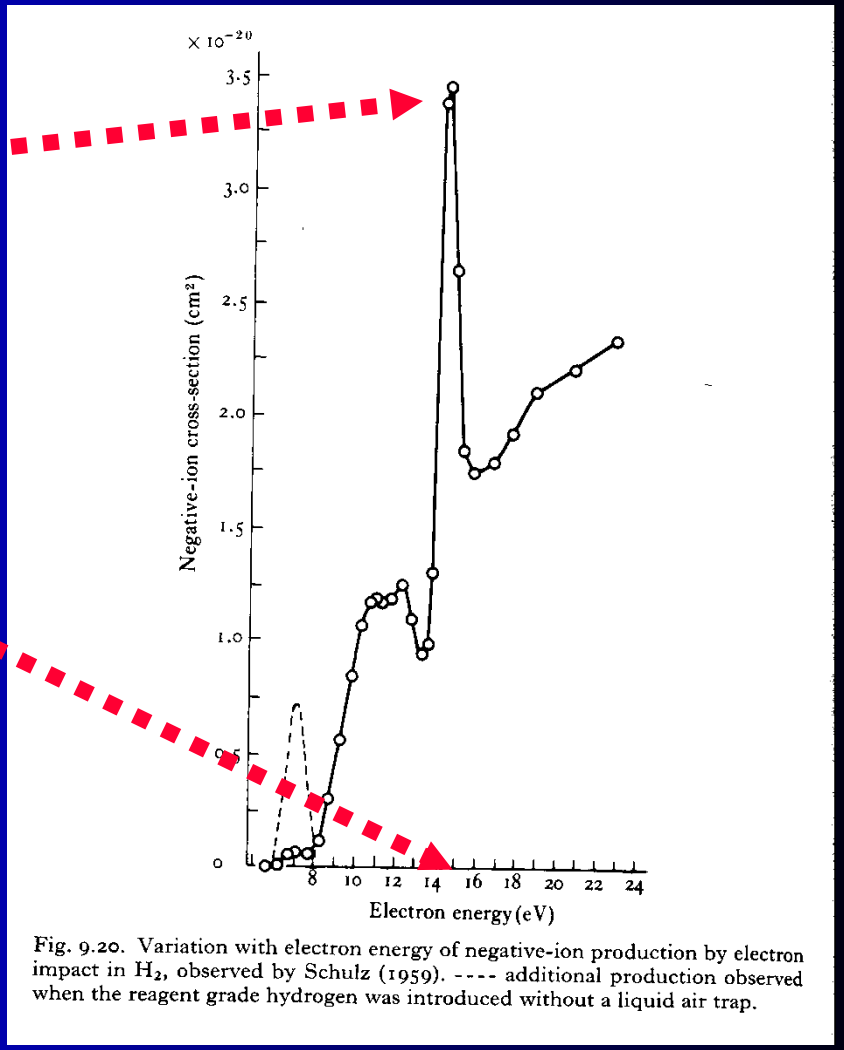

Fig. 9.20. Variation with electron energy of negative-ion production by electron impact in H_2, observed by Schulz (1959). ---- additional production observed when the reagent grade hydrogen was introduced without a liquid air trap.

Vibr. excitation of N_2 fine structure

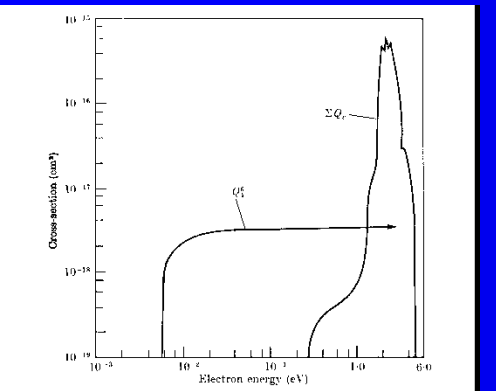

FIG. 11.31. Cross-sections for rotational and vibrational excitation of nitrogen. Q_4^6 is the cross-section for the rotational excitation $J = 4 \rightarrow J = 6$. $\Sigma_e Q_e$ is the sum of the cross-sections for vibrational excitation consistent with the swarm data.

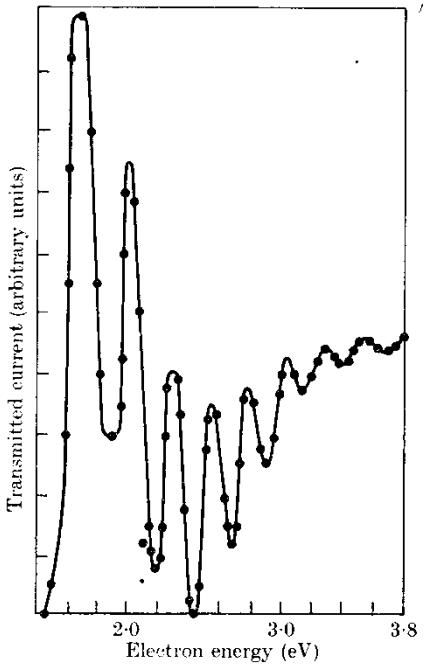

FIG. 10.32. Fine structure observed by Golden and Nakano in the transmission of electrons through N_2. The points are obtained from a number of plots of the transmitted current. Because of electron optical effects no significance attaches to the relative magnitudes of peaks and troughs.

of a theory such as that outlined above. Haas suggested that we must regard the collisions as taking place in two stages—the incident electron is first captured to form a negative ion N_2^- that is energetically unstable but has a lifetime greater than a vibrational period. It eventually breaks up, becoming a neutral molecule that may be in an excited vibrational state—in other words, the process is regarded as a resonance one of the same type as that found in elastic scattering of electrons by helium and other atoms and molecules (see Chap. 9).

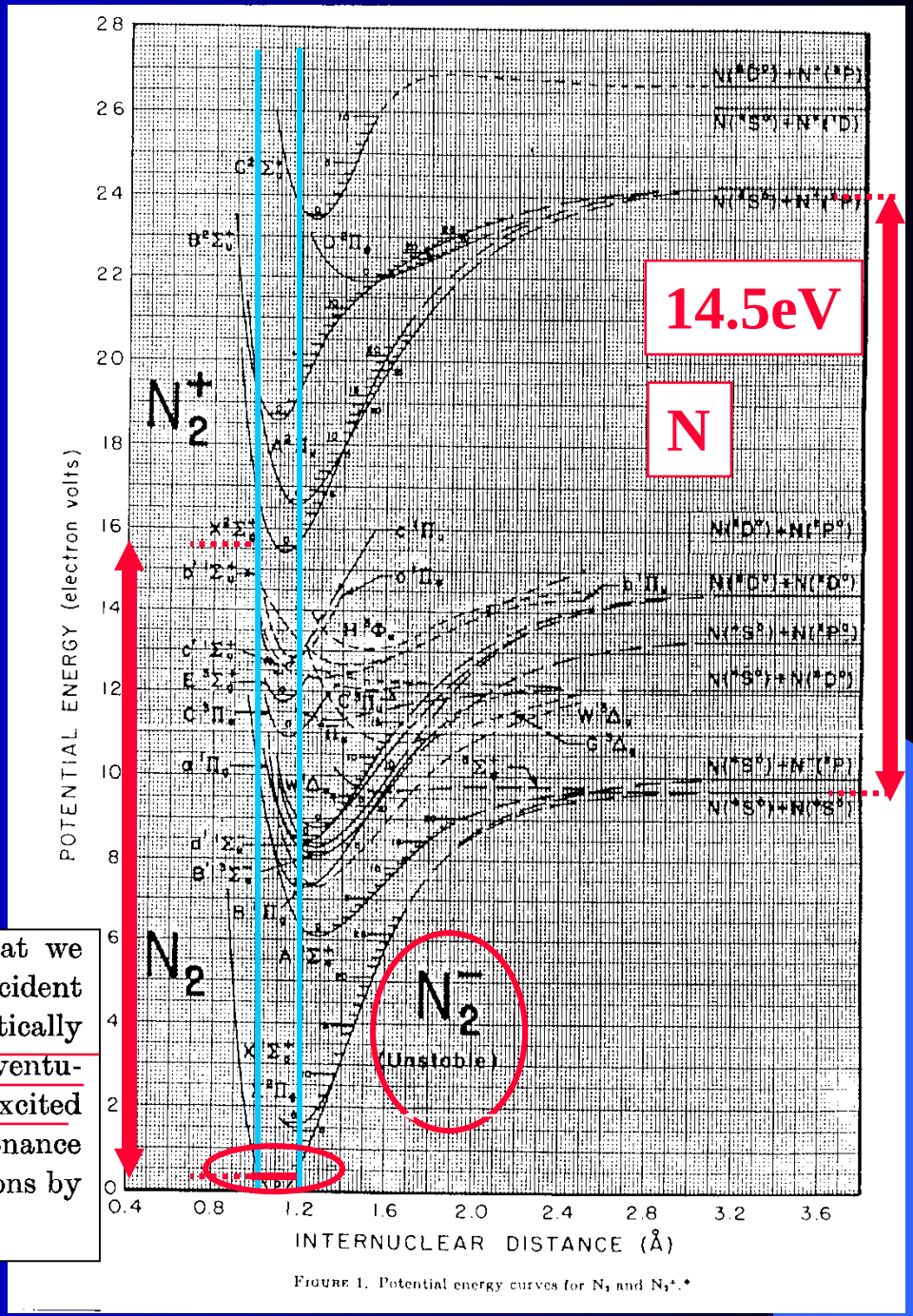

FIGURE 1. Potential energy curves for N_2 and N_2^+.*

Rotational excitation N_2

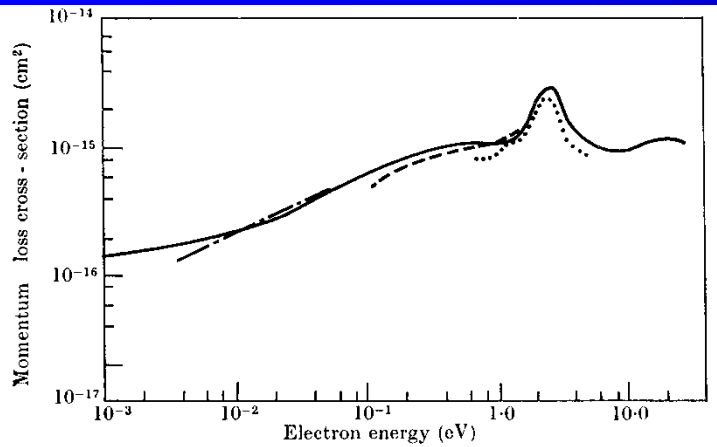

FIG. 11.30. Momentum-transfer cross-section for electrons in N_2. —— derived by Engelhardt, Phelps, and Risk from analysis of swarm data. —·—·— derived by Pack and Phelps from analysis of their drift velocity observations. — — — derived from drift velocity observations of Crompton and Sutton. ···· total cross-section measured by Ramsauer method.

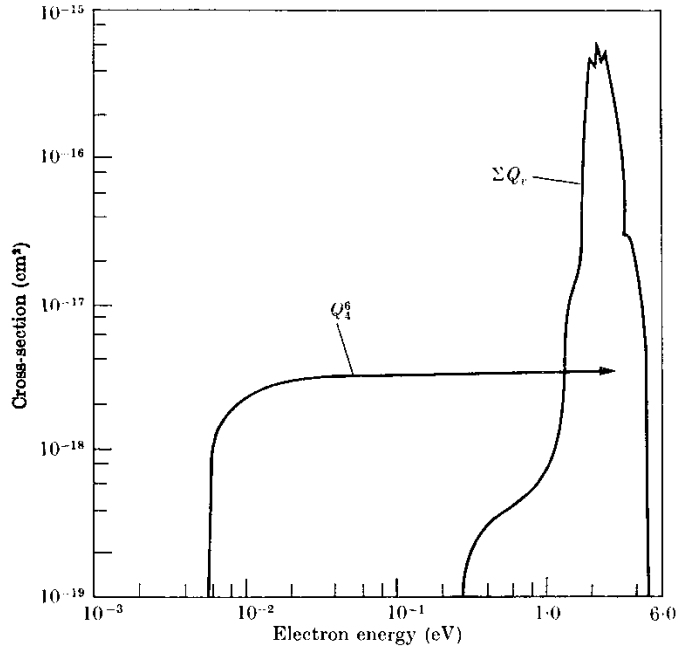

FIG. 11.31. Cross-sections for rotational and vibrational excitation of nitrogen. Q_4^6 is the cross-section for the rotational excitation $J = 4 \rightarrow J = 6$. $\Sigma_v Q_v$ is the sum of the cross-sections for vibrational excitation consistent with the swarm data.

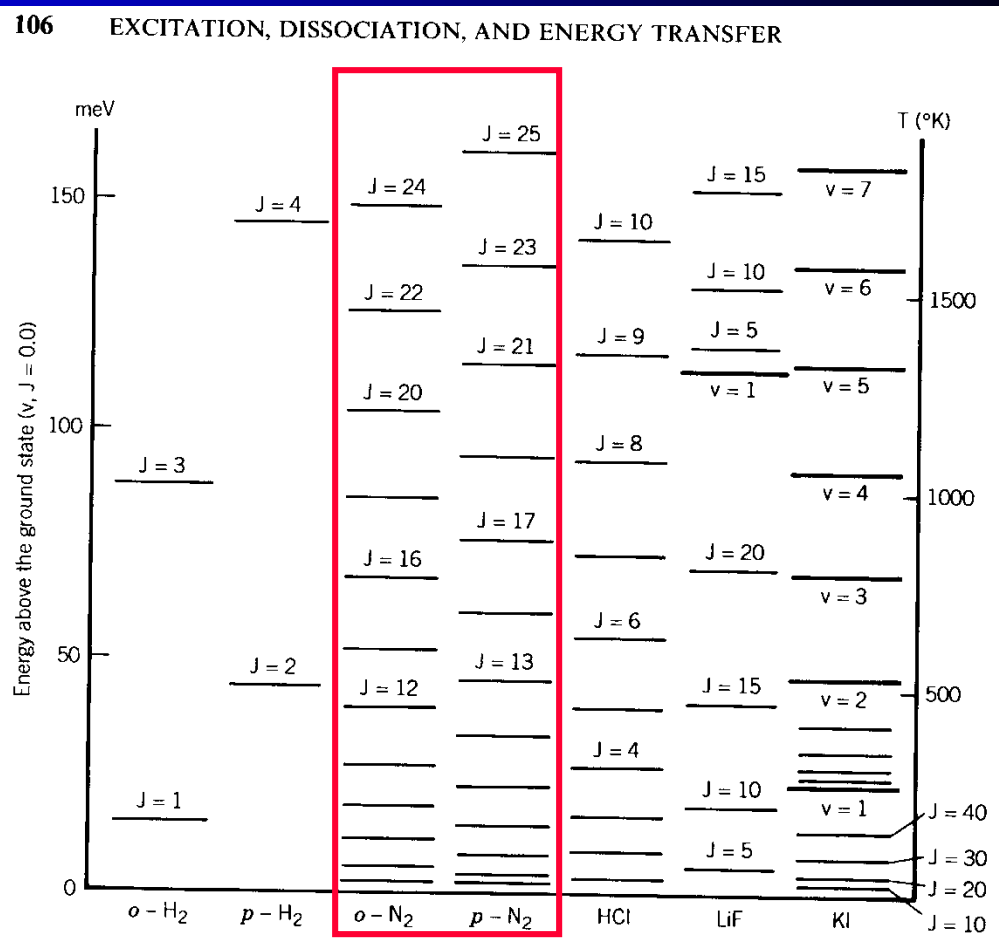

Figure 2-2-1. Vibrational–rotational levels (quantum numbers v and J) of a few diatomic molecules. The ($v = 1$, $J = 0$) level of H_2 lies 0.54 eV above the ground state ($v = 0$, $J = 0$). Rotational level spacings for H_2 are uniquely large, about $15J$ meV, where J is the quantum number for the upper level. For the ortho species of H_2(o-H_2), the nuclear spins are parallel; for the para version (p-H_2), the nuclear spins are antiparallel. [From Shimamura (1984).]

Cross section of electron attachment – idea of experiment

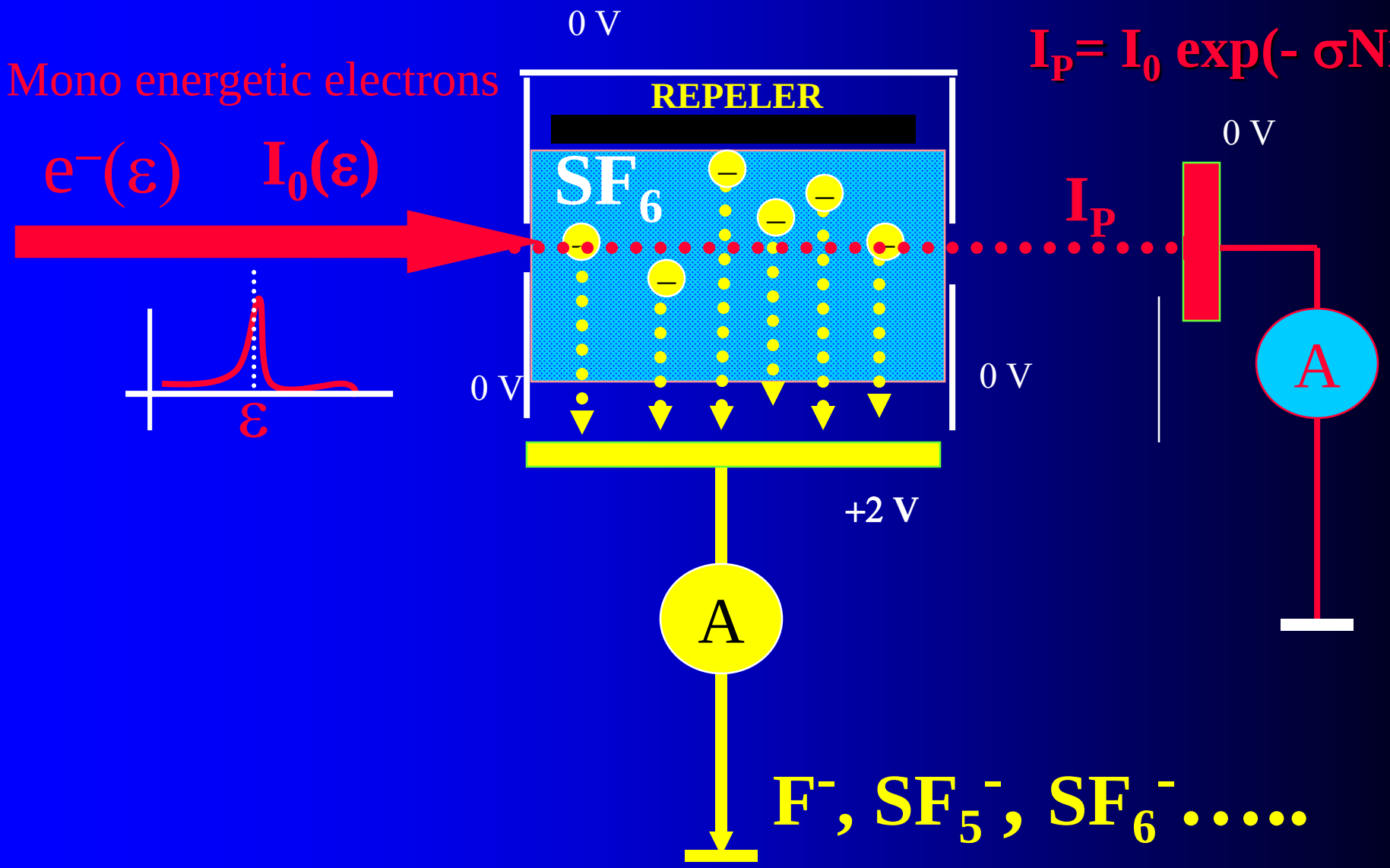

Electron attachment to HBr

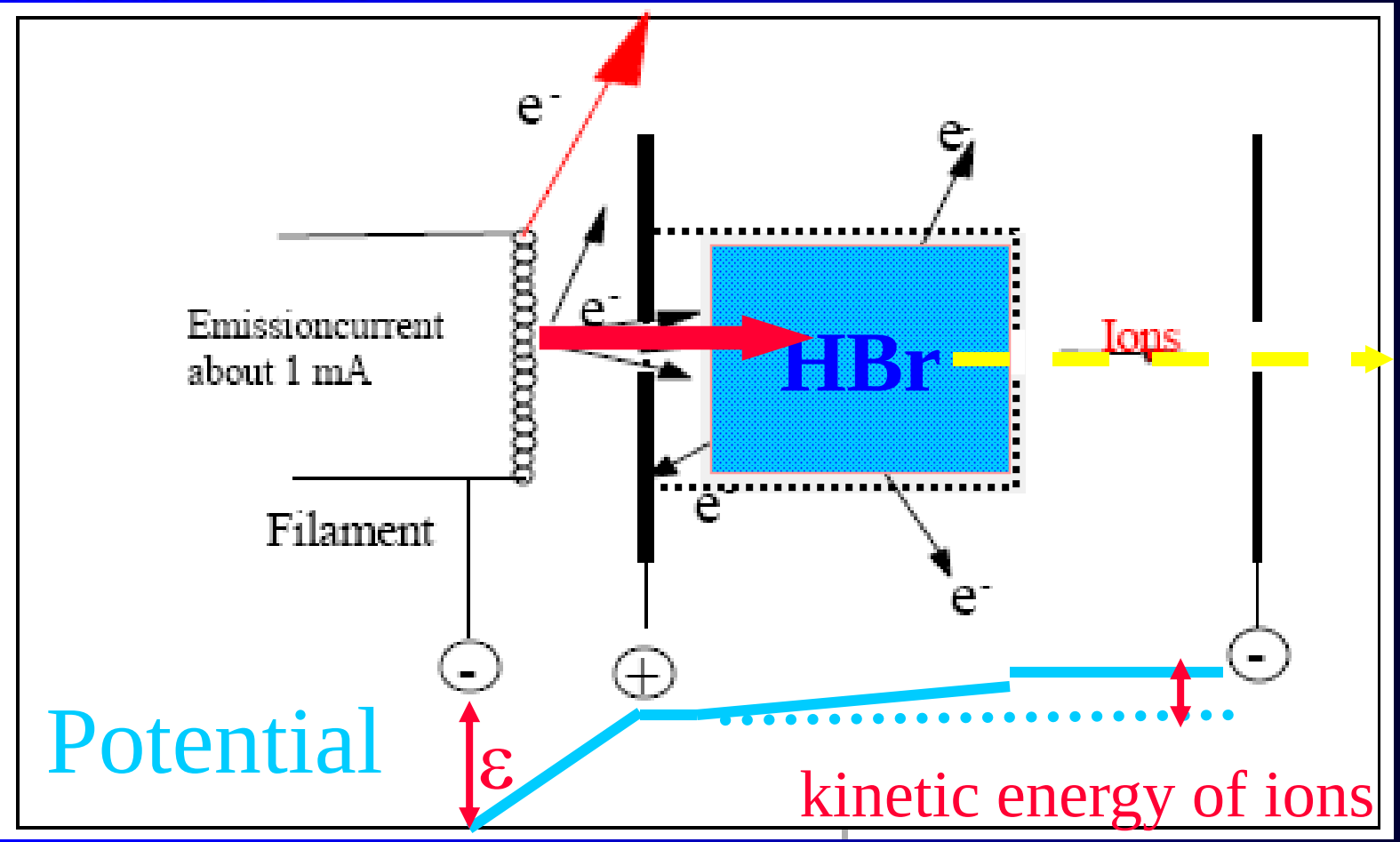

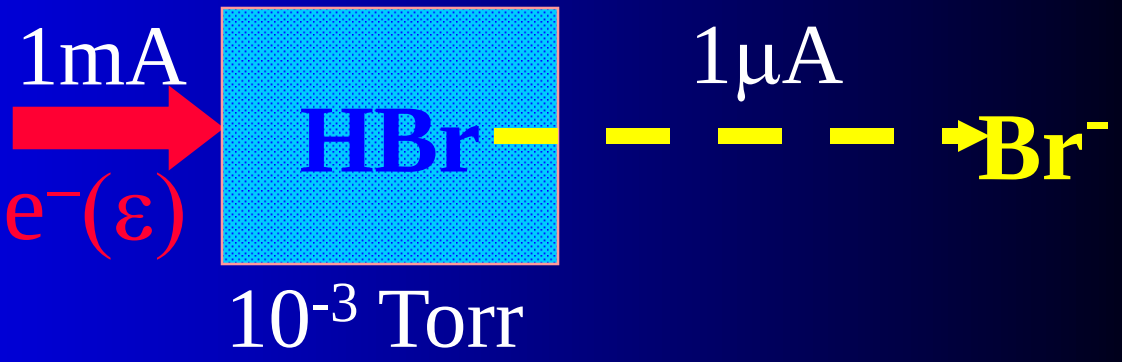

EA to CCl_2F_2 absolute cross section

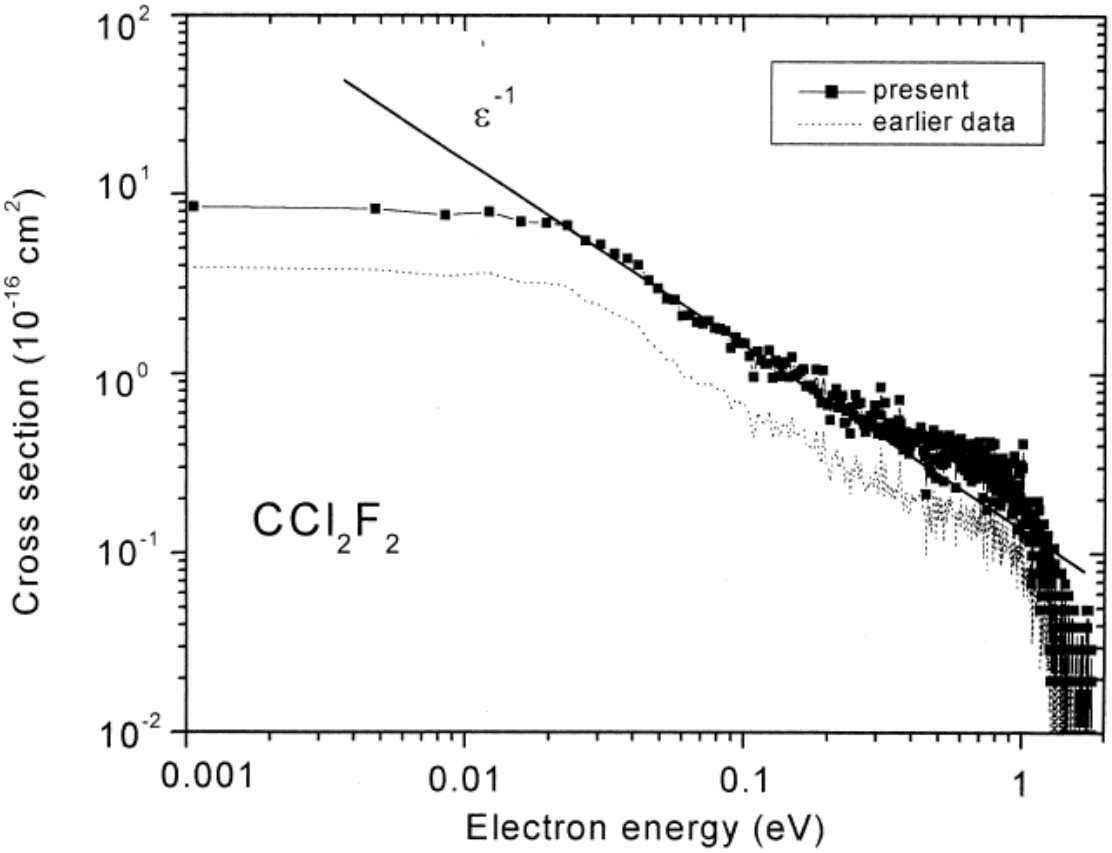

Fig. 1. Absolute electron attachment cross section vs. electron energy for the reaction $CCl_2F_2 + e \rightarrow Cl^-$. The present data (full line with full squares) were derived by using the calibration method outlined in the text [Eqs. (4) and (5)] involving integration of the measured anion signal. The earlier data (dashed line) are from [17] and have been obtained by [17] using the simple procedure employing Eq. (7). Also shown as full line designated ϵ^{-1} the predicted energy dependence for *s*-wave scattering.

Cross sections comparison

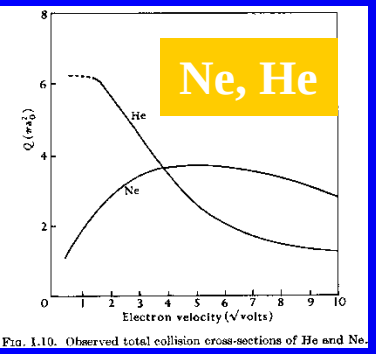

FIG. 1.10. Observed total collision cross-sections of He and Ne.

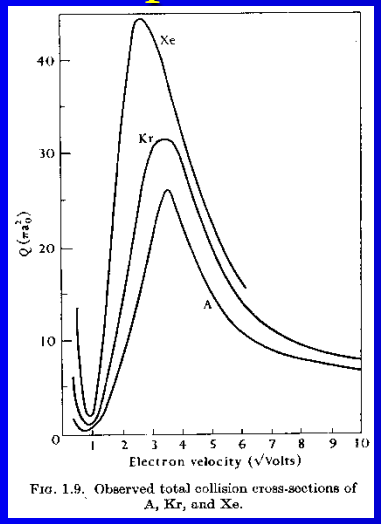

FIG. 1.9. Observed total collision cross-sections of A, Kr, and Xe.

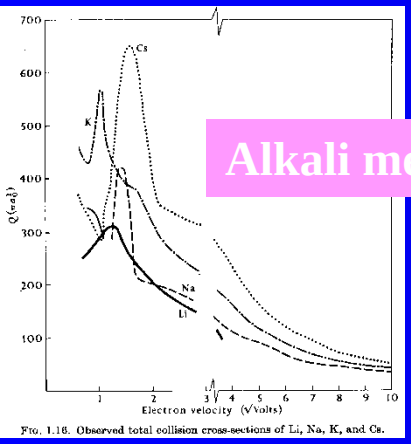

FIG. 1.18. Observed total collision cross-sections of Li, Na, K, and Cs.

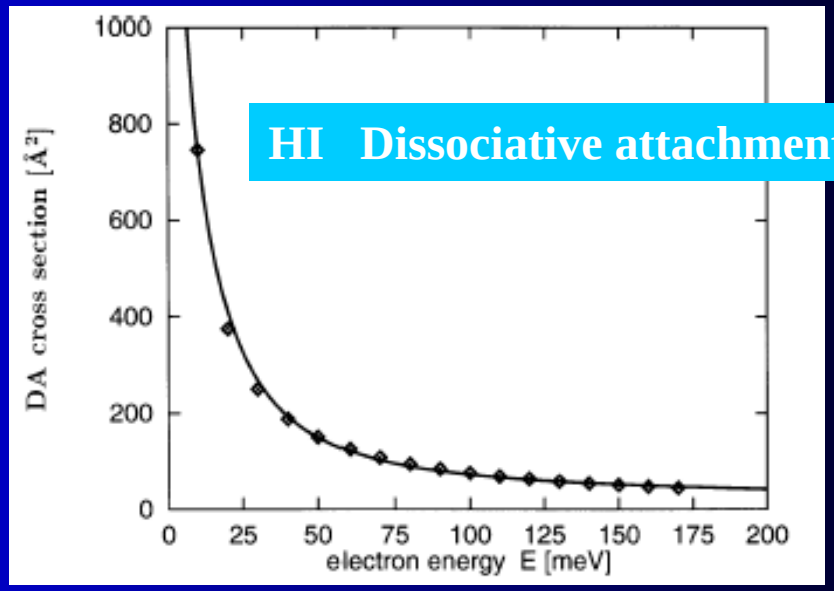

Calculated DA cross section in HI (*full curve*). *Diamonds* represent the experimental data of Klar et al. [24]

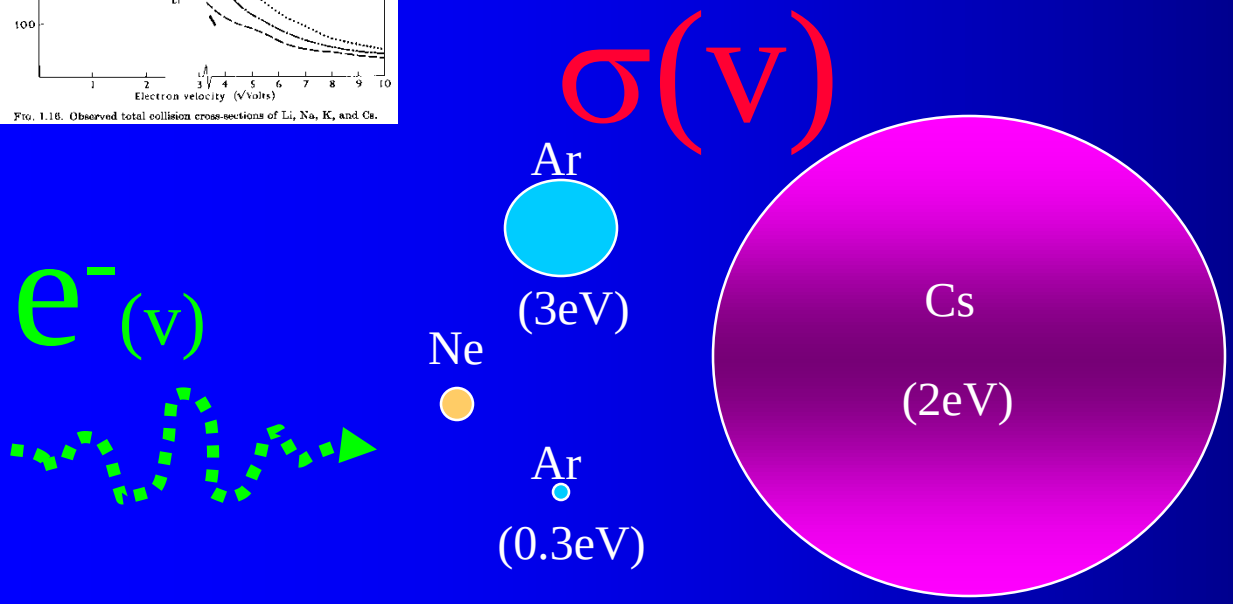

Attachment
HI
20meV

Electron Attachment Spectroscopy (EAS)

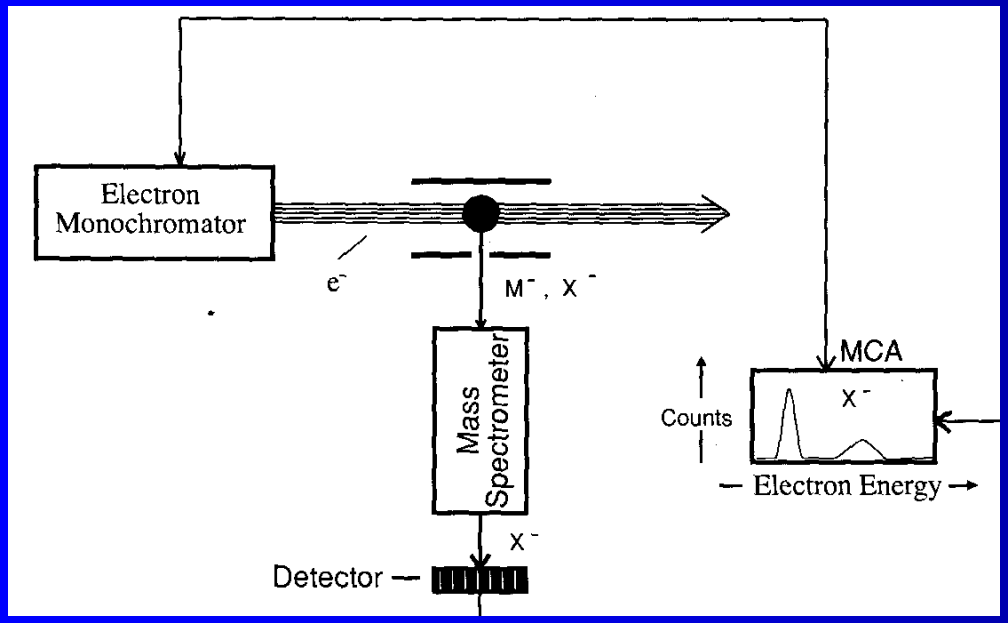

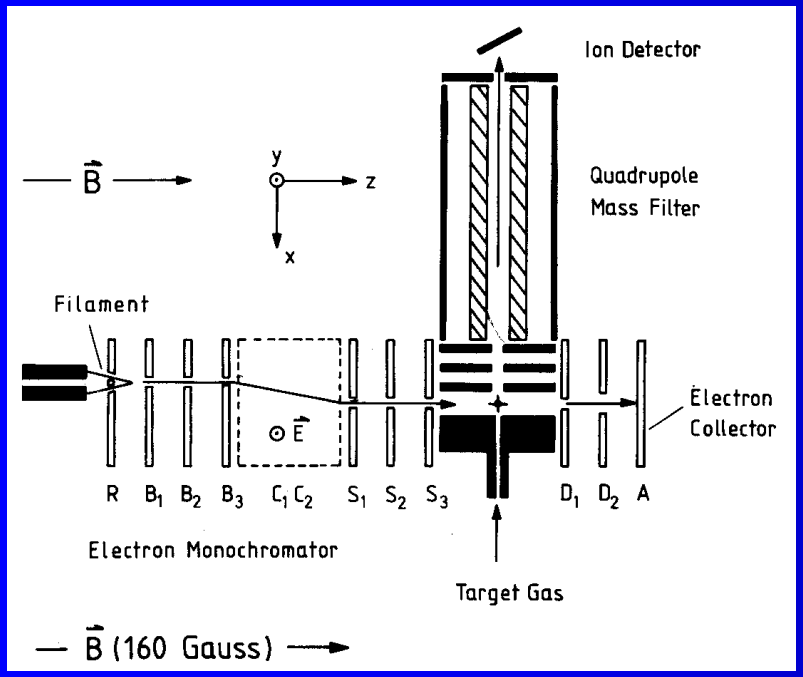

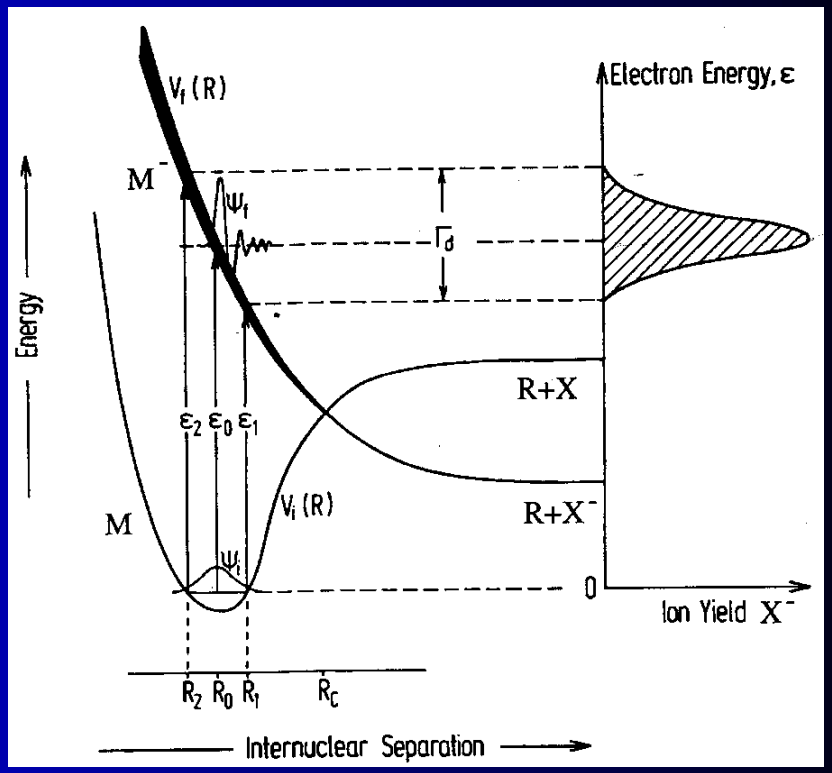

Electron Attachment Spectroscopy – electron energy distribution

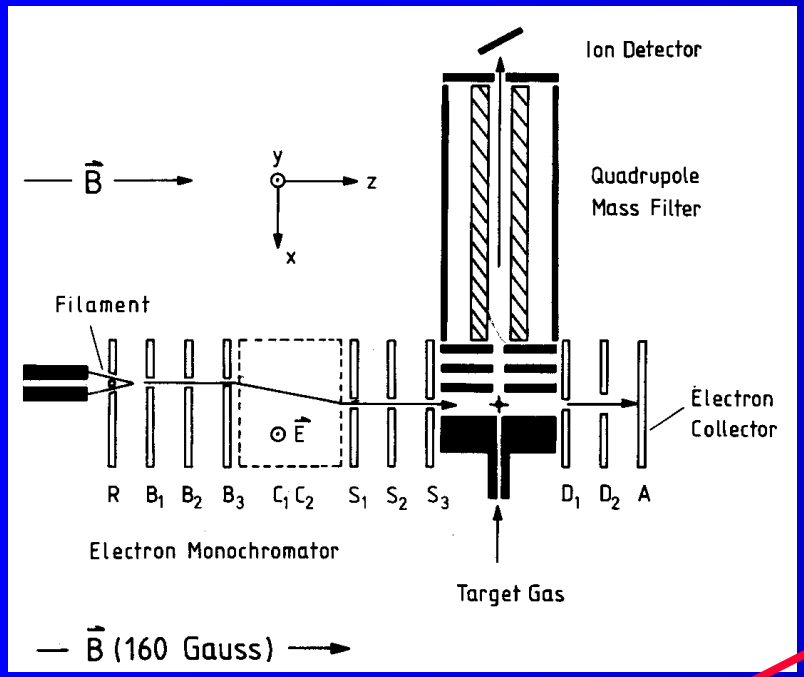

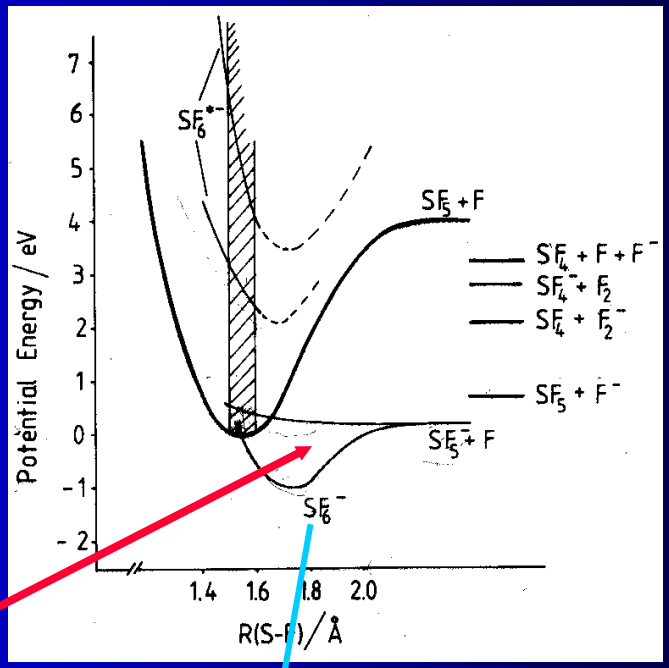

Three-body attachment

$SF_6 + e \rightarrow SF_6^-$

$SF_6 + e + M \rightarrow SF_6^- + M$

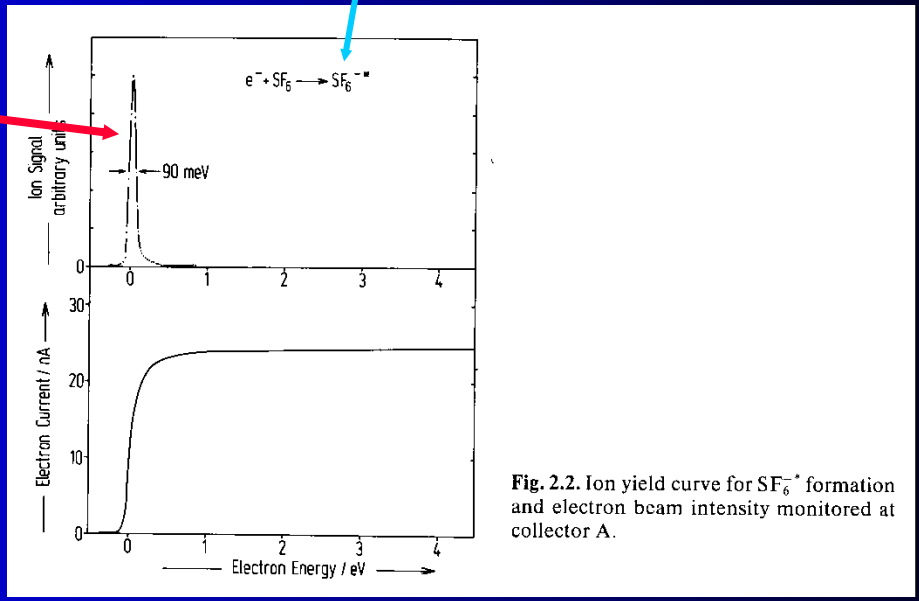

Fig. 2.2. Ion yield curve for SF_6^{-*} formation and electron beam intensity monitored at collector A.

EA SF_6

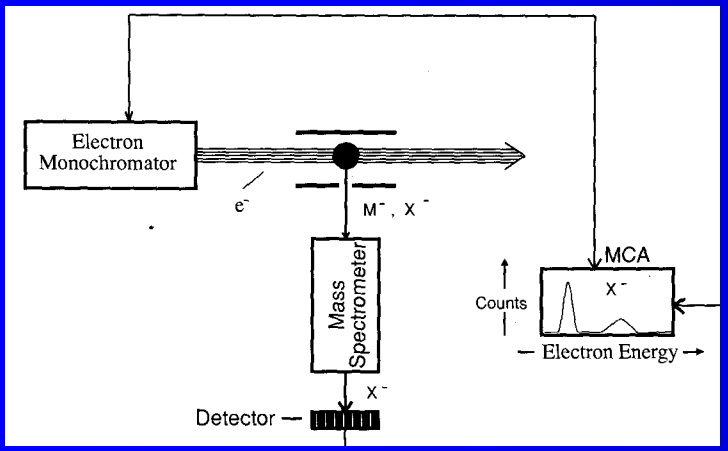
Electron Monochromator
e⁻
M⁻, X⁻
Mass Spectrometer
X⁻
Detector
MCA
X⁻
Counts
Electron Energy

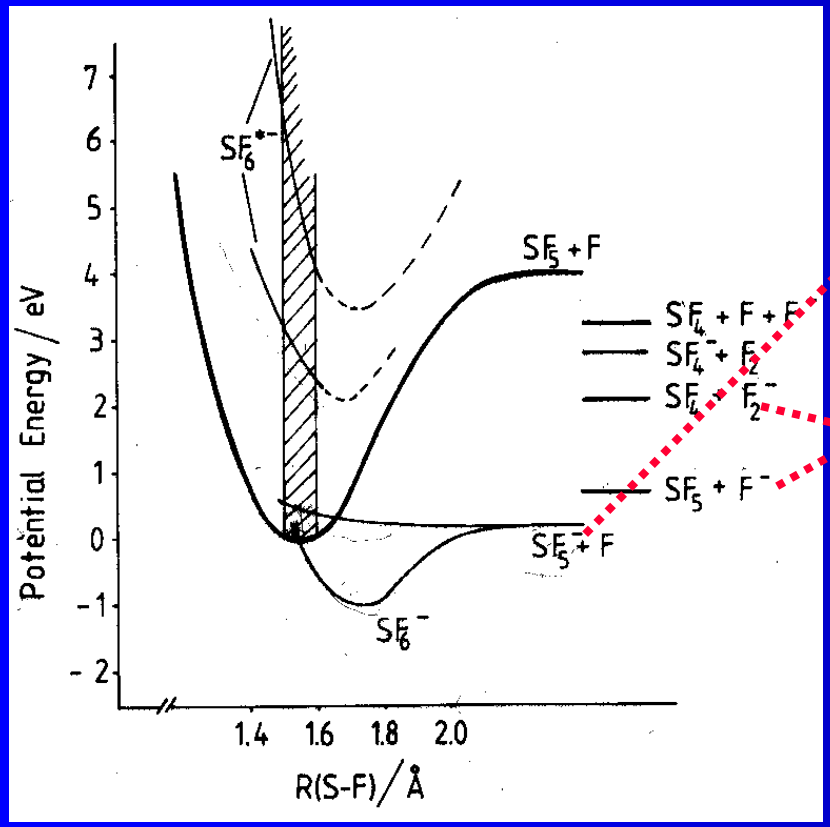
Potential Energy / eV
R(S-F) / Å
SF6*⁻
SF5 + F
SF4 + F + F
SF4⁻ + F2
SF4 + F2⁻
SF5 + F⁻
SF5⁻ + F
SF6⁻

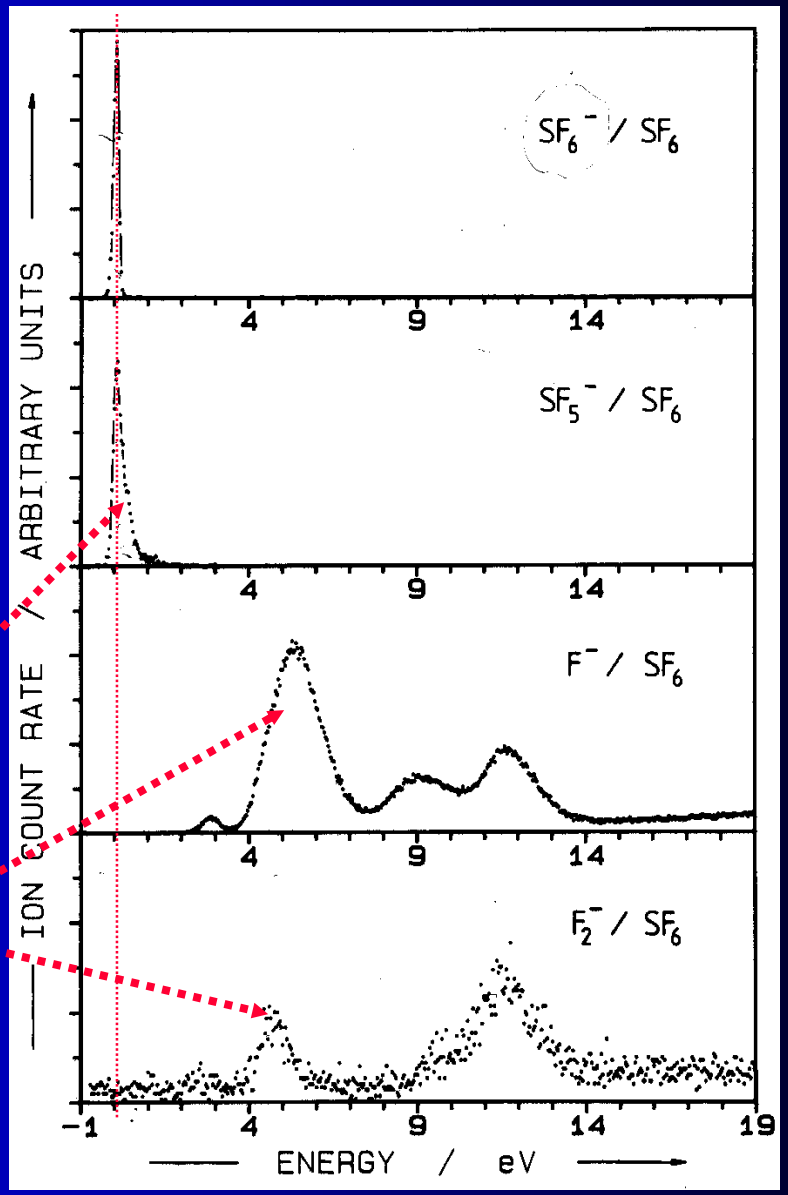
ION COUNT RATE / ARBITRARY UNITS
SF6⁻ / SF6
SF5⁻ / SF6
F⁻ / SF6
F2⁻ / SF6
ENERGY / eV

EA SF_6 temperature dependence

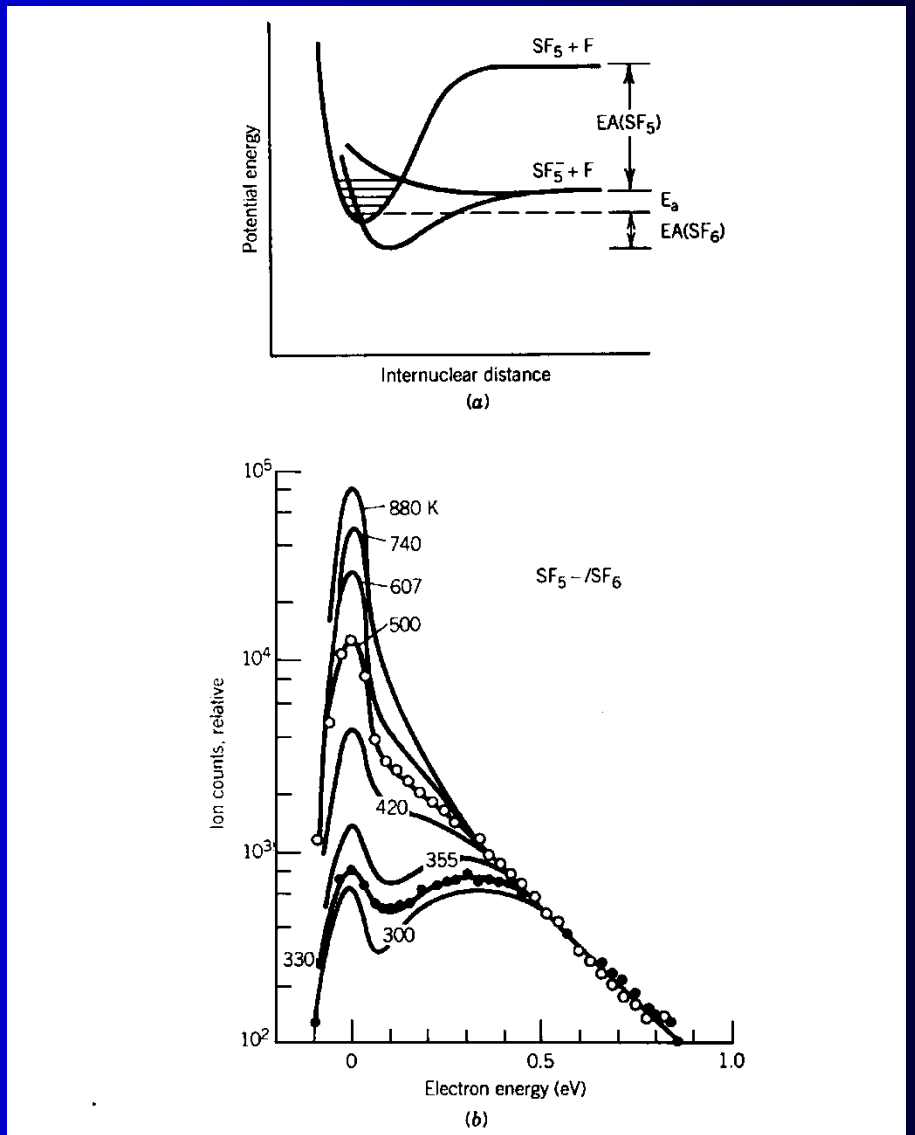

Figure 6-8-9. (*a*) Schematic potential energy curves for SF_6 and SF_6^-. (*b*) Electron attachment to form SF_5^- from SF_6 versus electron energy, for various gas temperatures. [From Chen and Chantry (1979).]

Attachment NO to particular channel

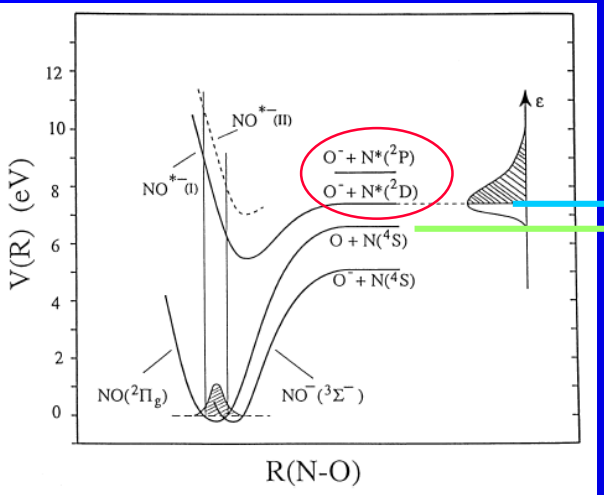

Fig. 5. Schematic potential energy curves for the ground states of NO and NO^- and two exited states of NO^{*-} after Ref. [8]. Also shown is the relative DA cross-section curve for the reaction $NO + e \rightarrow O^-(^2P) + N^*(^2D)$ obtained by applying the reflection principle.

Dissociative electron attachment to NO close to threshold may in principle proceed via the following channels:

$$NO + e \rightarrow O^-(^2P) + N(^4S), \quad (1a)$$

$$NO + e \rightarrow O^-(^2P) + N^*(^2D), \quad (1b)$$

$$NO + e \rightarrow O^-(^2P) + N^*(^2P). \quad (1c)$$

The threshold energies of 5.074, 7.457 and 8.650 eV, respectively, can be derived using the bond dissociation energy $D(N–O) = 6.535$ eV [10], the electron affinity $EA(O) = 1.461$ eV [11] and the excitation energies $E(N^*(^2D)) = 2.383$ eV and $E(^*N(^2P)) =$

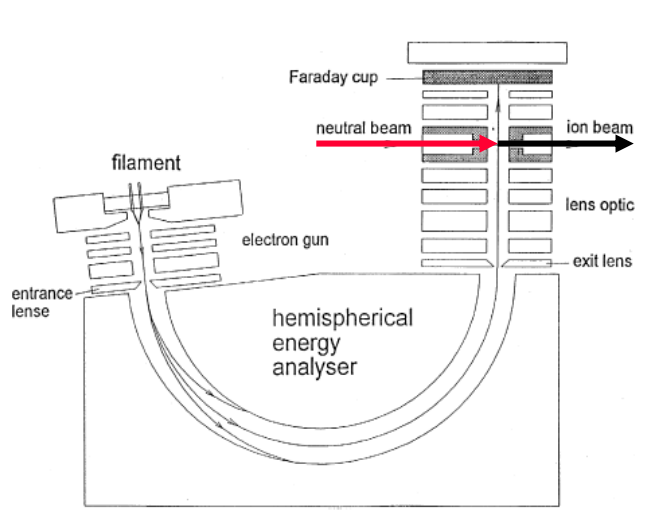

Fig. 1. Schematic diagram of the apparatus. Electrons are emitted from a hot filament, formed into a beam, pass the hemispherical energy selector at a constant energy of ~2 eV and are focused and brought to the final collision energy before they interact with the neutral beam and are collected at a Faraday cup.

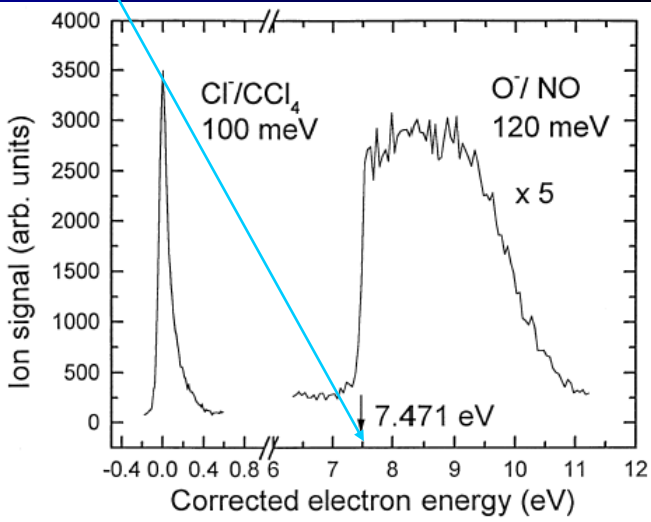

Fig. 4. Formation of O^- from NO by electron impact. The Cl^-/CCl_4 cross-section curve is used to calibrate the electron energy scale and to determine the electron energy resolution (120 meV). The arrow points to the presently determined threshold energy of the reaction $NO + e \rightarrow O^-(^2P) + N^*(^2P)$.

EA clusters and surface

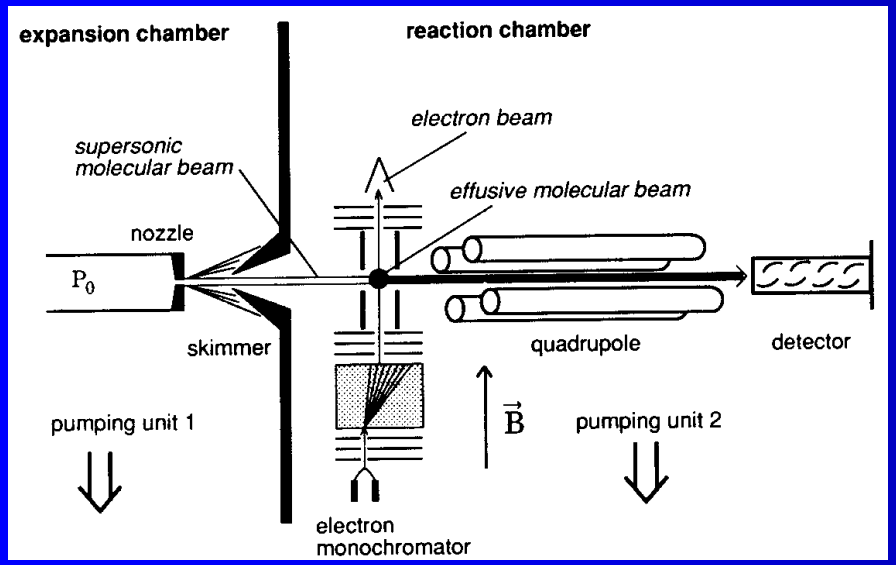

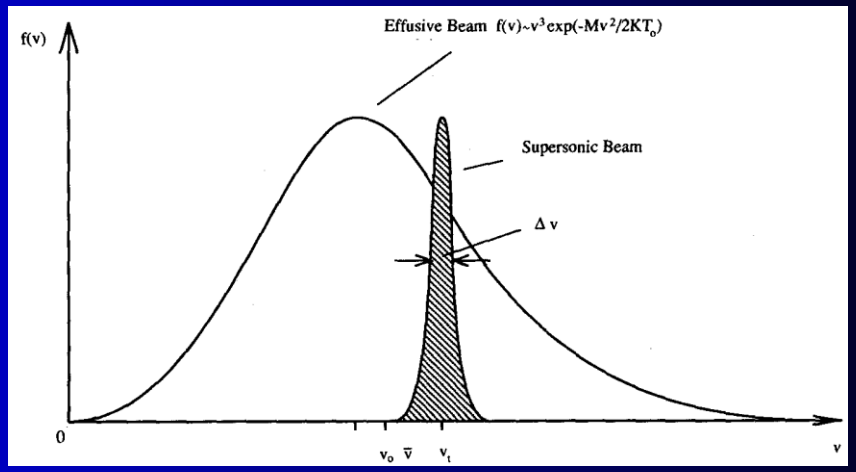

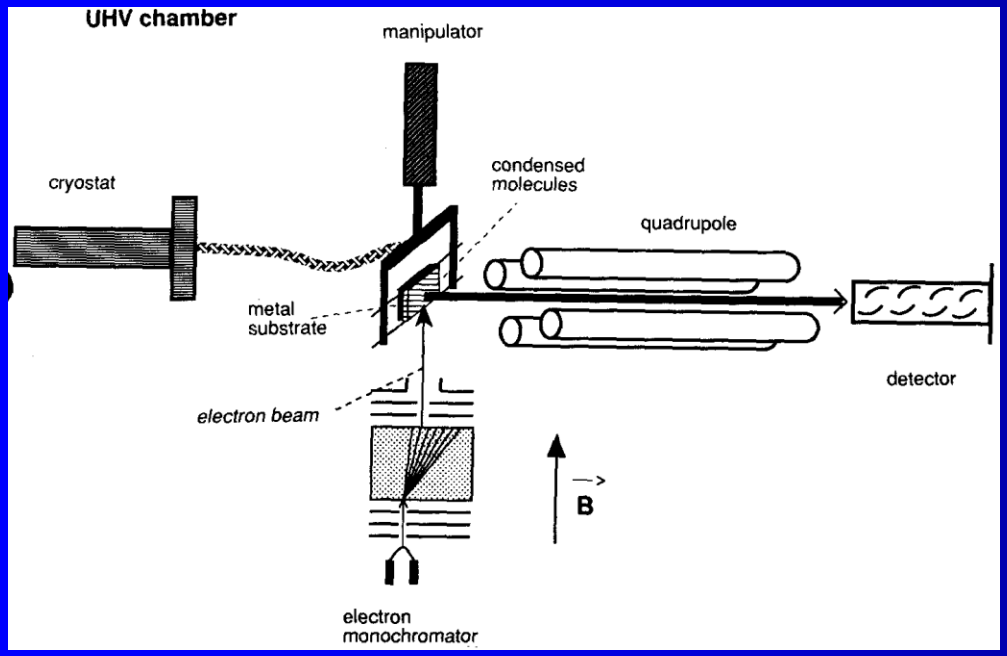

Energy levels in clusters

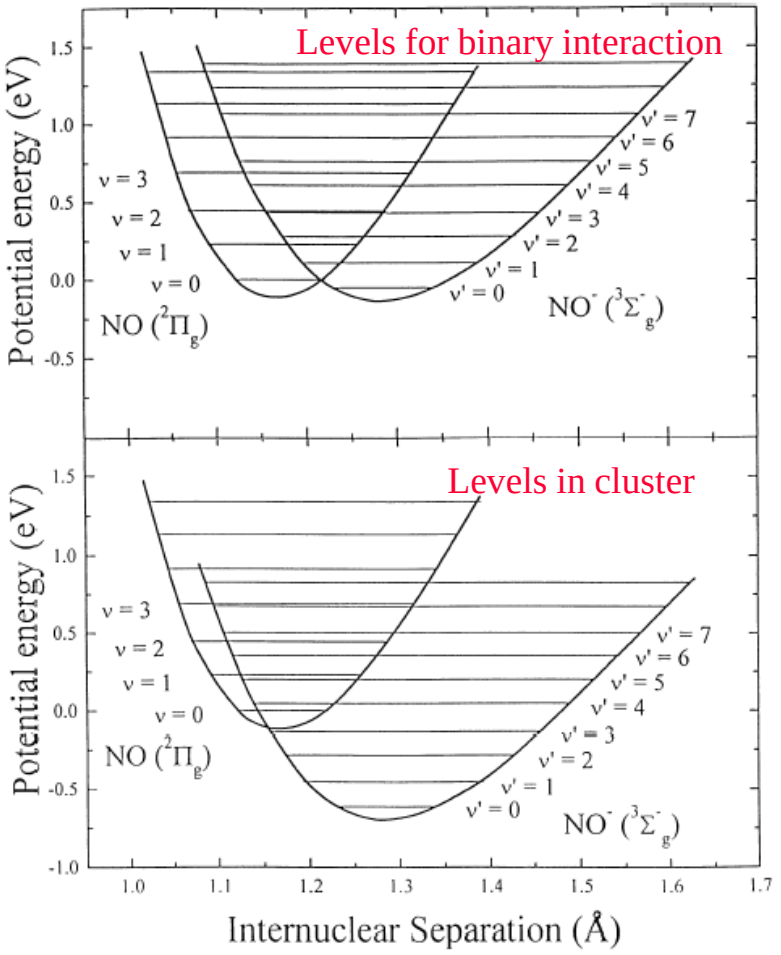

Fig. 3. Upper panel: approximate potential energy diagrams for NO and NO^- adapted from Ref. [5]. The $\acute{v} = 0$ level is located at 26 meV below the $v = 0$ level of neutral NO. Lower panel: potential energy curves as above but shifted for the anion due to the polarization interaction of the negative charge with surrounding NO molecules. The NO^- curve is positioned (arbitrarily) so that the $\acute{v} = 4$ level is accessible by 40 meV electrons, in accordance with the experiment.

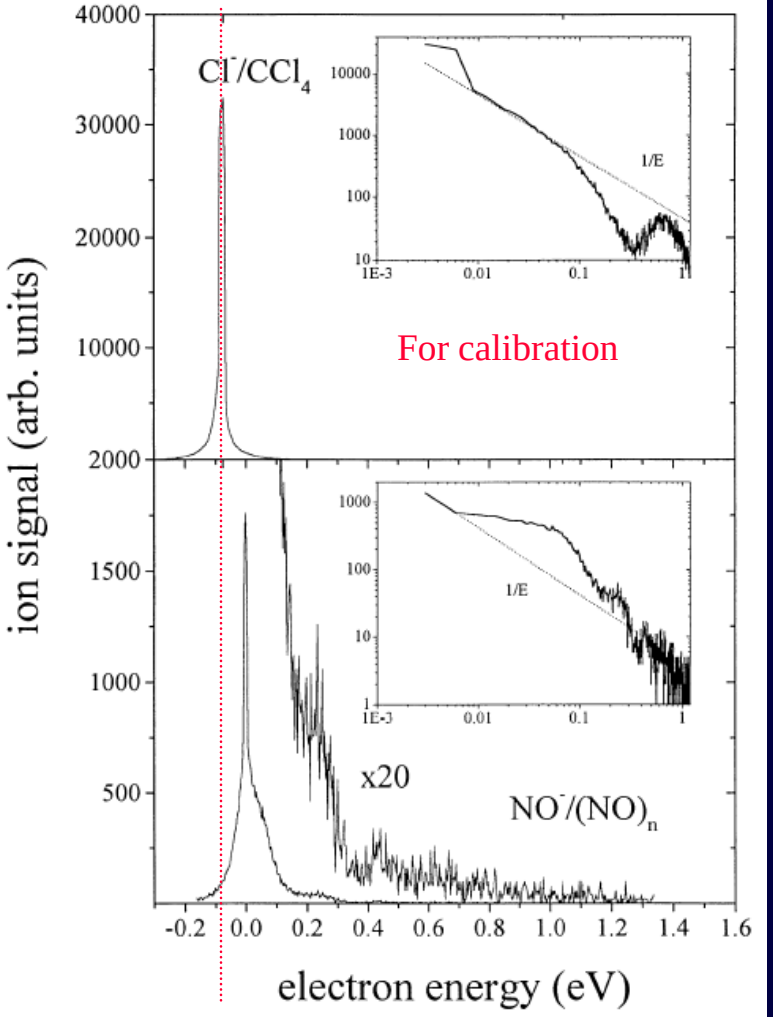

Fig. 1. NO^- signal observed from electron attachment to an NO cluster beam as a function of the electron energy. For comparison the energy calibration signal Cl^- from CCl_4 is also shown. Insets: count rate versus electron energy on a log–log scale. Dotted lines indicate the $1/E$ dependence predicted by s-wave scattering theory.

Negative ions, formation of negative clusters

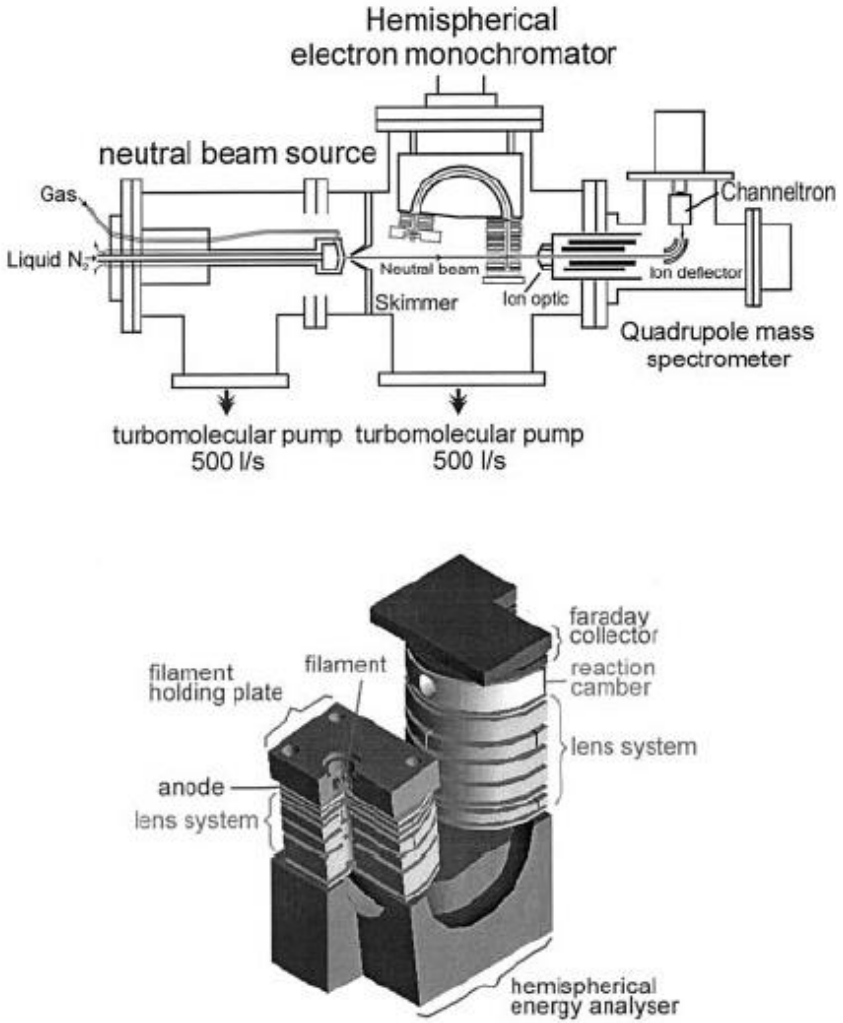

Fig. 1. Schematic diagram of the instrument. Electrons are emitted from a hot filament, and focused into a beam. They pass the hemispherical energy selector at a constant energy of about 4 eV and are focused and brought to the final collision energy before they interact with the neutral beam and are collected at a Faraday cup. Also shown is a close-up of the monochromator in a three dimensional view.

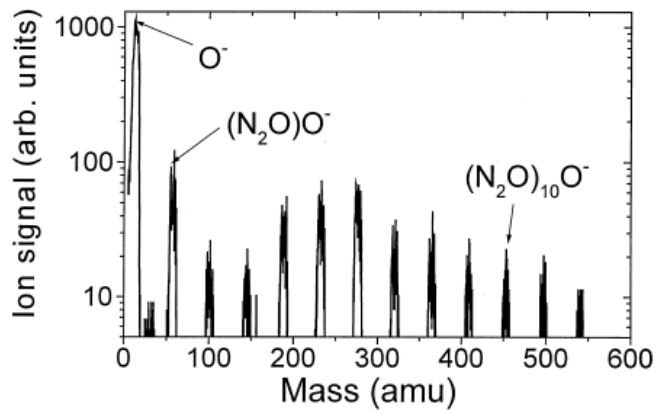

Fig. 2. Mass spectrum for $(N_2O)_nO^-$ cluster anions produced by electron attachment (using 2 eV electrons) to a N_2O cluster beam formed with the stagnation gas temperature at room temperature and the stagnation gas pressure of 3 bar.

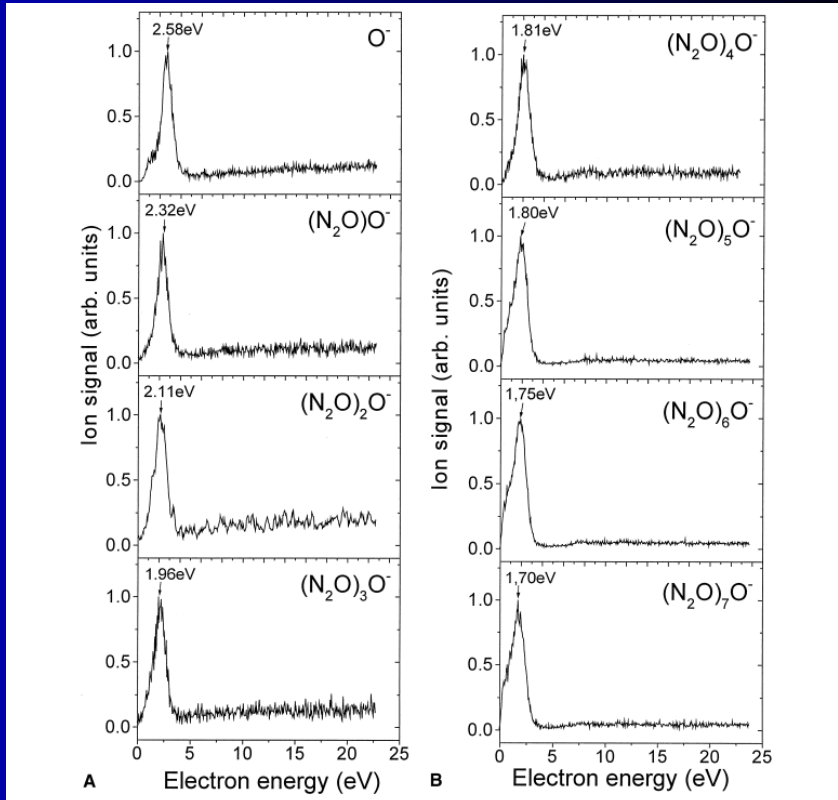

Fig. 6. Energy dependence of the $(N_2O)_nO^-$ yield for various cluster sizes (all curves are normalized to the same maximum value) for an extended range of electron energy (as compared to results shown in Fig. 4 which only cover the range up to 4 eV).

Rydberg atom attachment apparatus

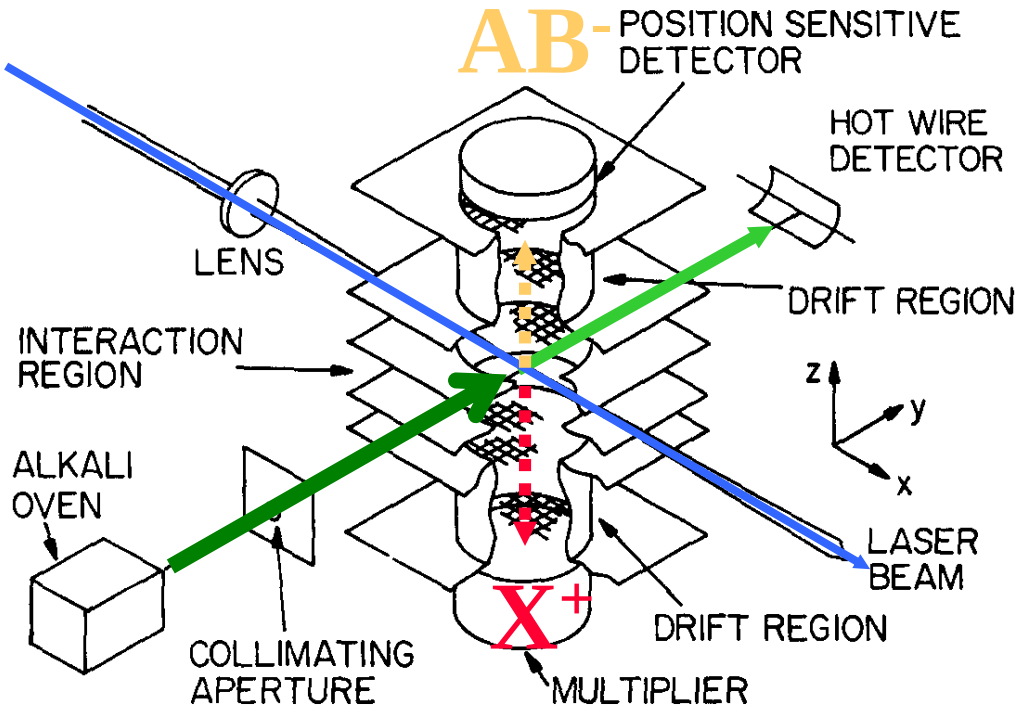

Figure 6-6-2. Dunning's Rydberg atom attachment apparatus. [From Dunning (1987).]

X^* are produced by laser excitation

$$X^* + AB \rightarrow X^+ + AB^-$$

X^+ and AB^- are detected by the pair of opposing detectors. Time-of-flight technique can be used to determine the mass of the negative ions The density of Rydberg atoms in the interaction region can be determined by applying sufficiently strong electric field to ionize the atoms and then counting the ions thus formed.

Electron attachment from laser excited Rydberg atoms - Hotop

X* are produced by laser excitation

$$X^* + AB \rightarrow X^+ + AB^-$$

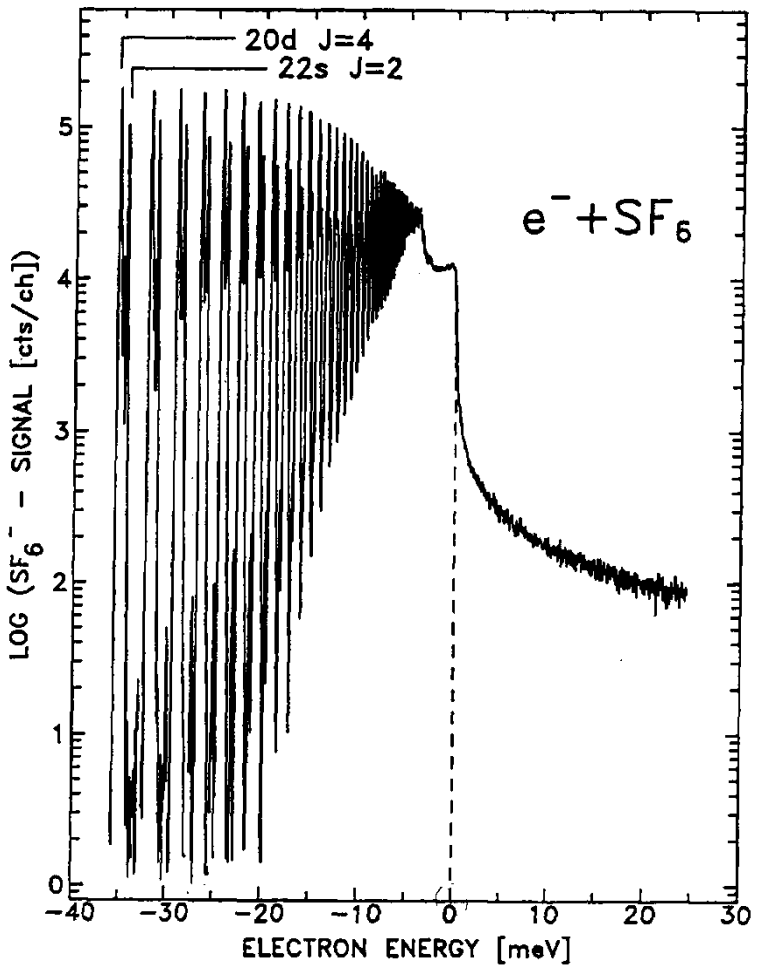

Figure 6-6-6. Results from Hotop's experiments on electron attachment from laser-excited Rydberg atoms and photodetached threshold electrons. [From Klar et al. (1991).]

Photodetachment of negative ions

Atomic Collisions – Heavy particle projectiles (1993)
E.W.McDaniel, J.B.A.Mitchell, M.E.Rudd,

6-10. DETACHMENT PROCESSES

A. Photodetachment of Negative Ions

The detachment of electrons from negative ions by photon impact has been the subject of intensive investigation since the pioneering work of Branscomb and collaborators in the 1950s and 1960s (Branscomb, 1962). Recent reviews of progress in this area have been given by Miller (1981), Drzaic et al. (1984), Mead et al. (1984), and Ervin and Lineberger (1991). By measuring the location of photodetachment thresholds, it is possible to obtain extremely accurate values of electron affinities for atomic and some molecular negative ions, as discussed in Section 6-2. The high photon flux available from laser light sources has led to improvements in accuracy of many orders of magnitude for such measurements.

A typical apparatus used for photodetachment studies is that shown in Fig. 6-10-1. Negative ions are produced in a hot-cathode arc discharge or cold-

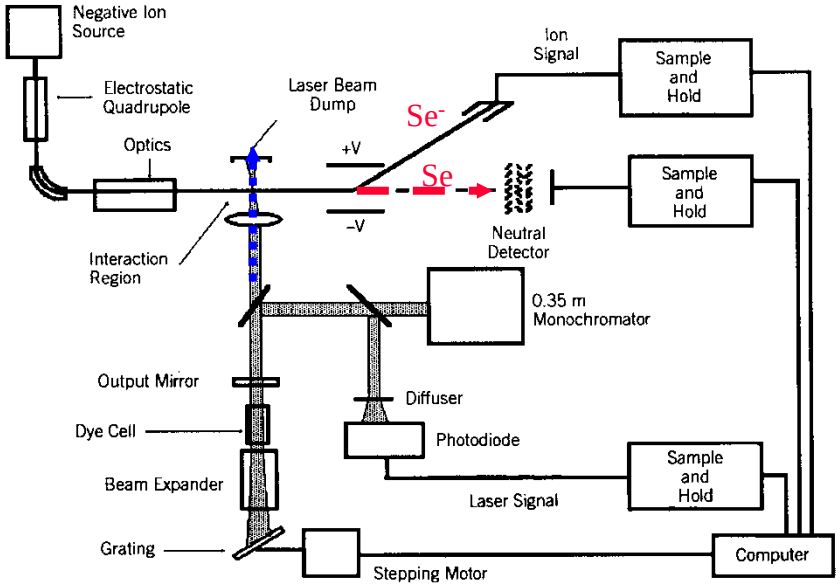

Figure 6-10-1. Apparatus used by Lineberger and Woodward (1970) for studying photodetachment with a tunable dye laser as a light source.

Threshol Studies

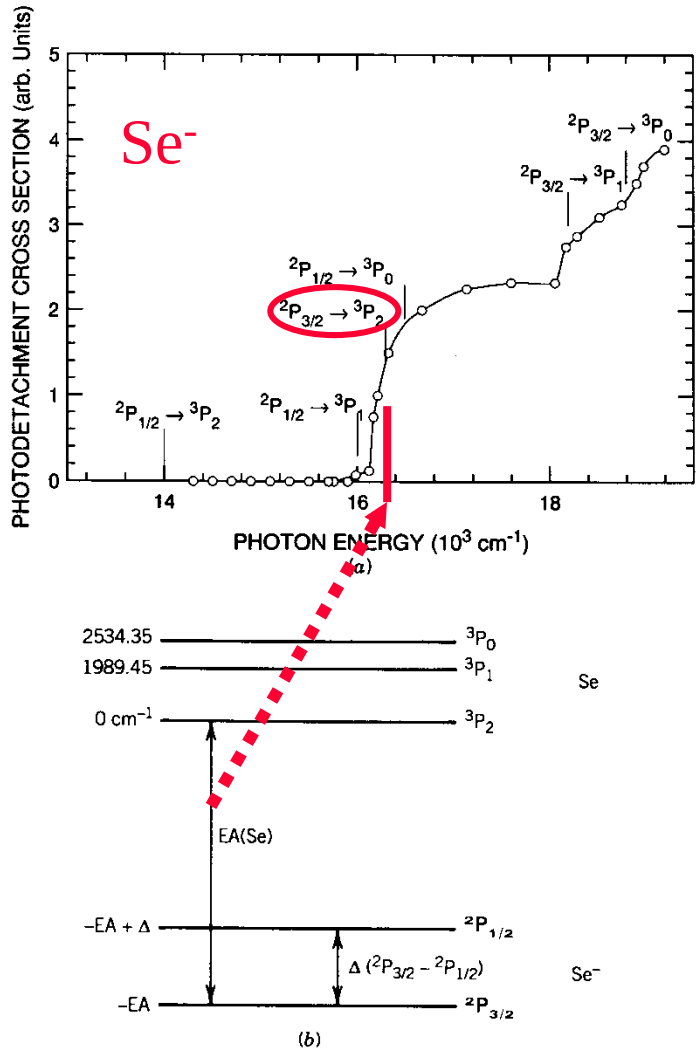

Figure 6-10-3. (*a*) Photodetachment cross sections for Se^-, measured with a tunable dye laser as a light source, by Lineberger and Woodward (1970) and by Hotop et al. (1973), respectively. (Not all measured data points are shown. (*b*) Energy levels of Se and Se^-.

Cross section

Photodetachment $O^- + h\nu \rightarrow O + e$

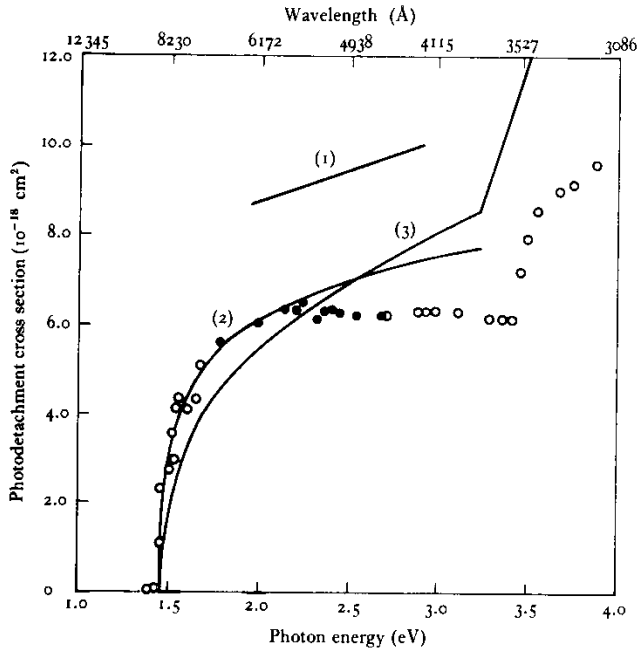

Fig. 11.15. Photodetachment cross-sections for O^-. ●, ○, observed by Branscomb *et al.* (1965), (1) derived from analysis of arc emission spectra by Boldt (1959) (see Chapter 8, p. 253), (2) calculated by Cooper and Martin (1962), (3) calculated by Robinson and Geltman (1967).

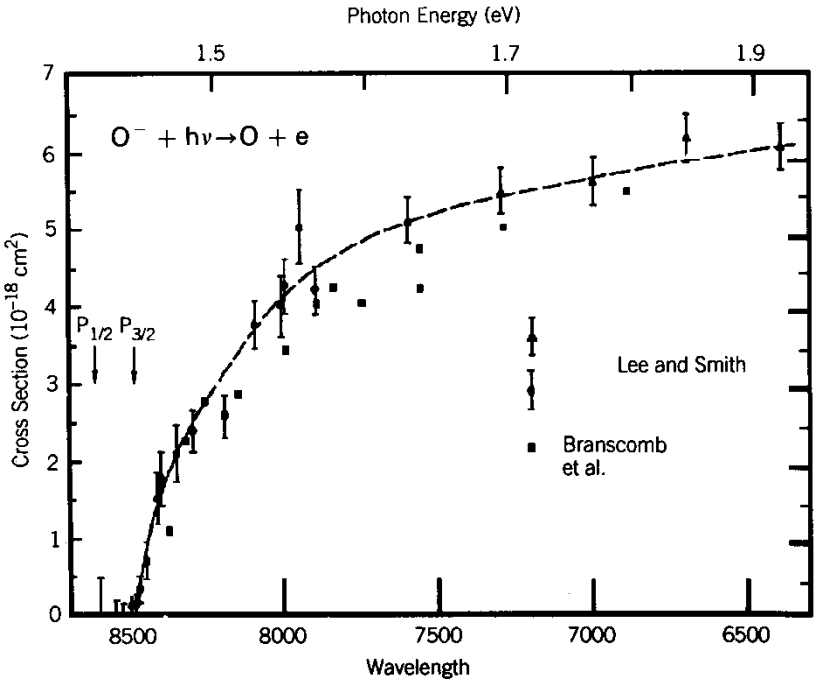

Figure 6-10-6. Photodetachment cross sections for O^-. [From Lee and Smith (1979).]

Electron affinity of O is 1.46eV

Cross section

Cross sections comparison

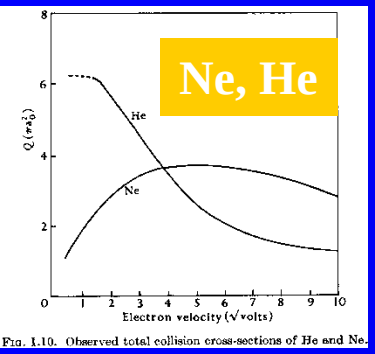

FIG. 1.10. Observed total collision cross-sections of He and Ne.

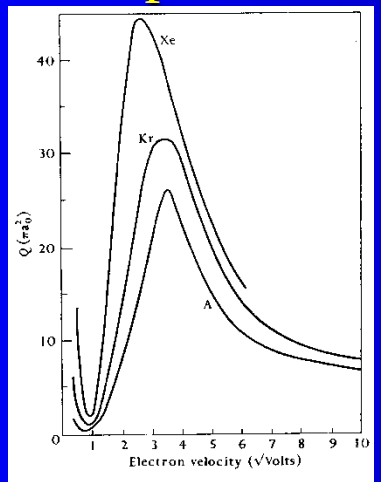

FIG. 1.9. Observed total collision cross-sections of A, Kr, and Xe.

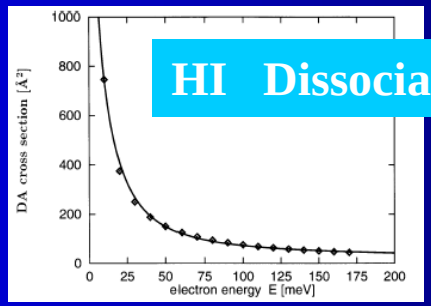

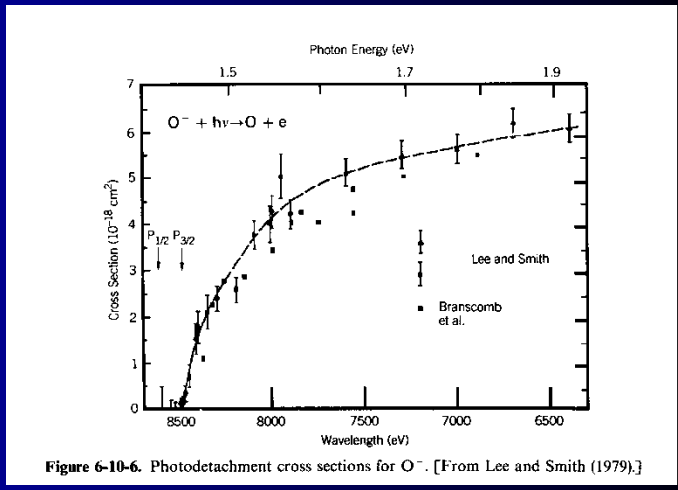

Figure 6-10-6. Photodetachment cross sections for O^-. [From Lee and Smith (1979).]

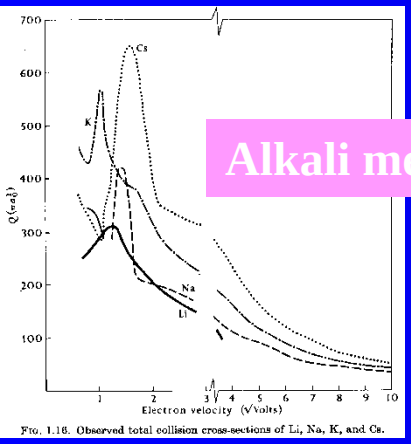

FIG. 1.18. Observed total collision cross-sections of Li, Na, K, and Cs.

$\sigma(v)$

Ar

(3eV)

Ne

Ar

(0.3eV)

$e^-(v)$

Cs

(2eV)

Attachment HI

Photodetachment x10^{-2}

Photodetachment $H^- + h\nu \rightarrow H(n) + e$ Cross section

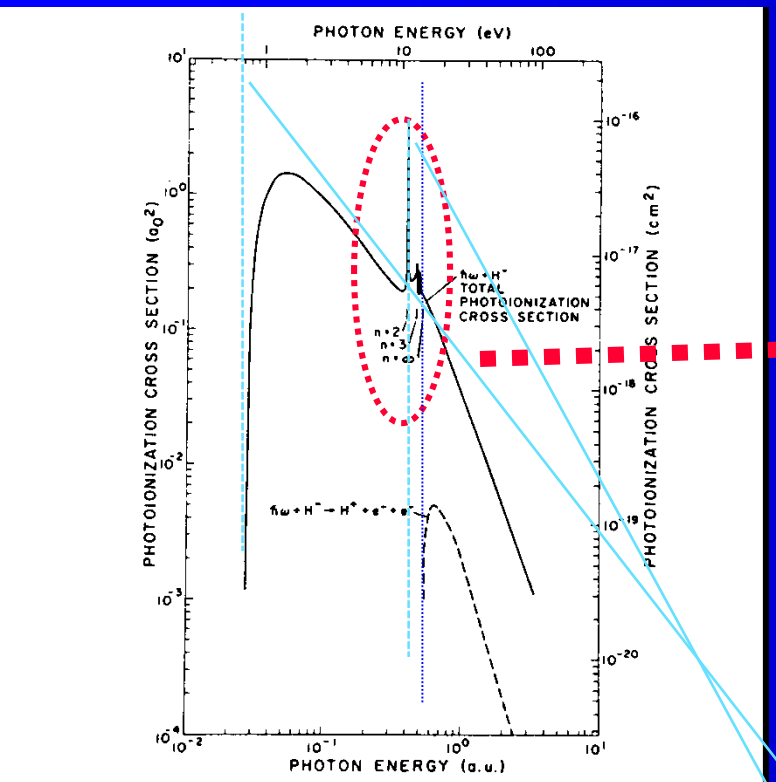

Figure 6-10-7. Theoretical photodetachment cross sections for H^-. [From Broad and Reinhardt (1976).]

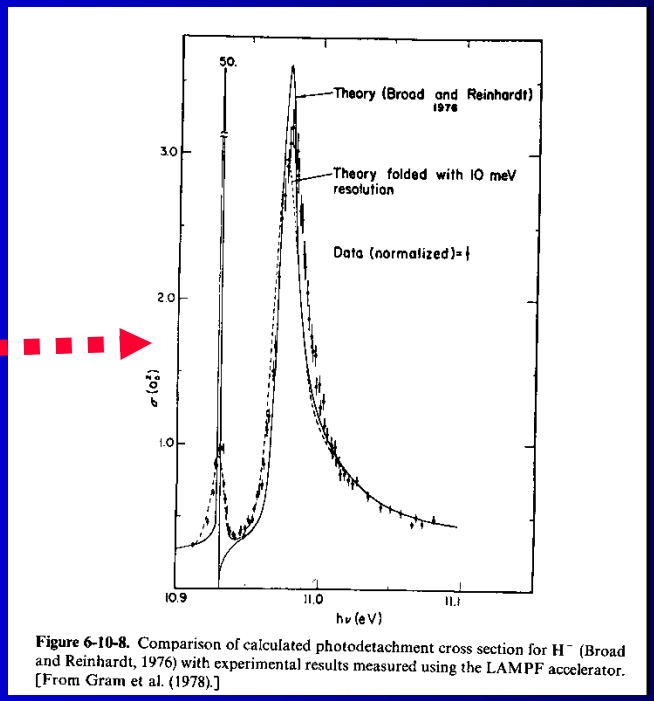

Figure 6-10-8. Comparison of calculated photodetachment cross section for H^- (Broad and Reinhardt, 1976) with experimental results measured using the LAMPF accelerator. [From Gram et al. (1978).]

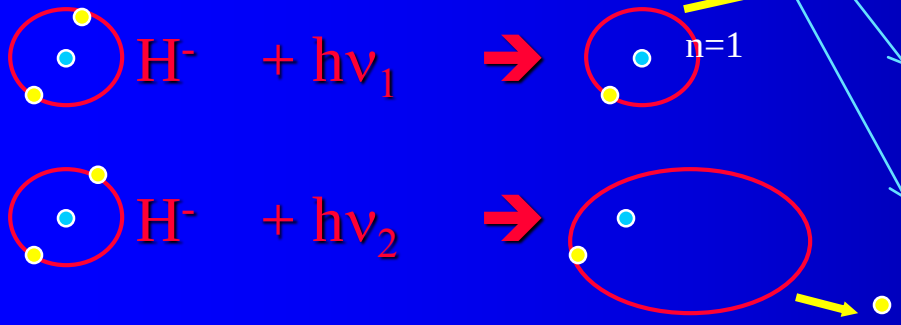

Photodetachment $O_2^- + h\nu \rightarrow O_2 + e$

Fig. 11.8 shows a typical arrangement used in the study of photodetachment from NO^- and O_2^- which is very similar to that used for He^-.

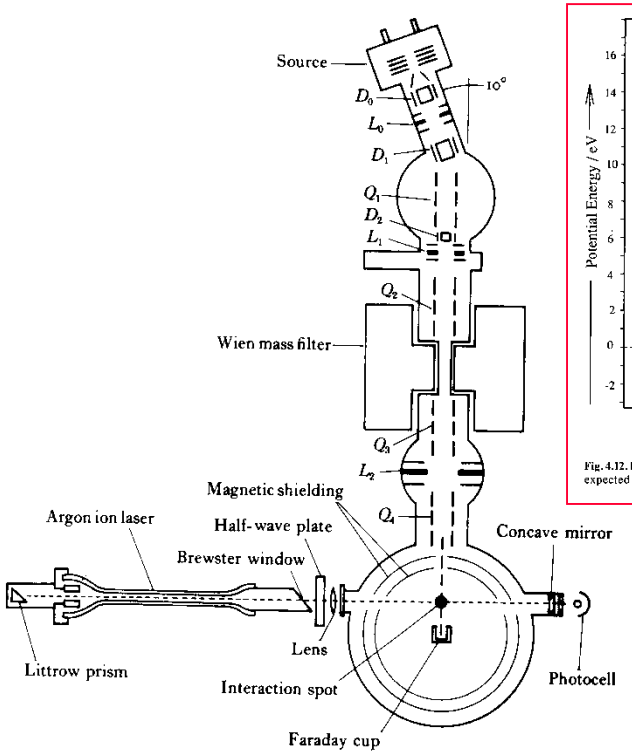

Fig. 11.8. Arrangement of the apparatus used for measurement of the angular and energy distribution of electrons resulting from photodetachment by laser light. From Siegel *et al.* (1972). D_0, D_1, D_2, vertical and horizontal deflectors; L_0, L_1, L_2 einzel lenses; Q_1, Q_2, Q_3, Q_4, twelve-element symmetrical quadrupole lenses.

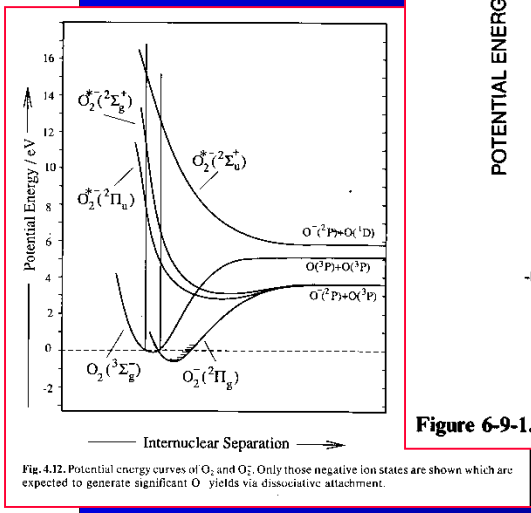

Fig. 4.12. Potential energy curves of O_2 and O_2^-. Only those negative ion states are shown which are expected to generate significant O yields via dissociative attachment.

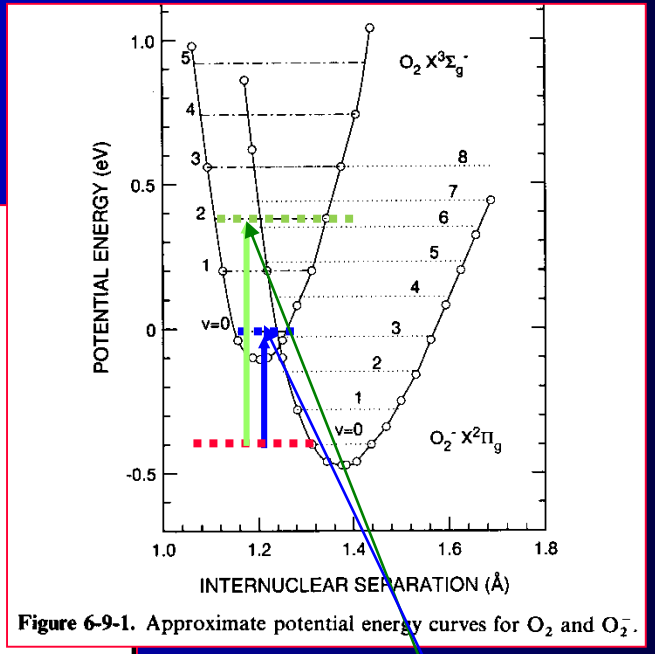

Figure 6-9-1. Approximate potential energy curves for O_2 and O_2^-.

Fig. 11.32 shows a typical photoelectron spectrum which they observed, using argon ion laser light at 4880 Å. It will be seen that there is evidence of two series of peaks, that the fourth and ninth

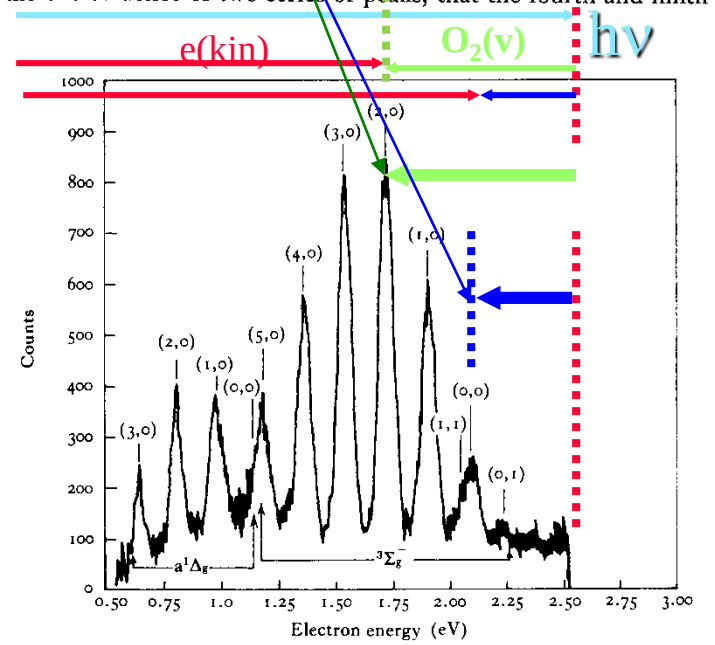

Fig. 11.32. Energy spectrum of the photoelectrons arising through photodetachment from O_2^- by argon ion laser light, as observed by Celotta *et al.* (1972).

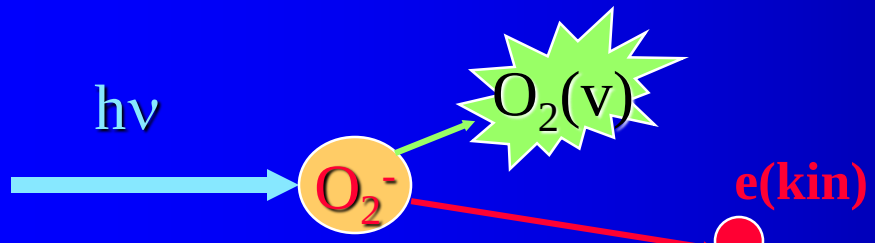

Electron spectroscopy

Hanspeter Helm - Photoelectron spectrometer - Experimental setup

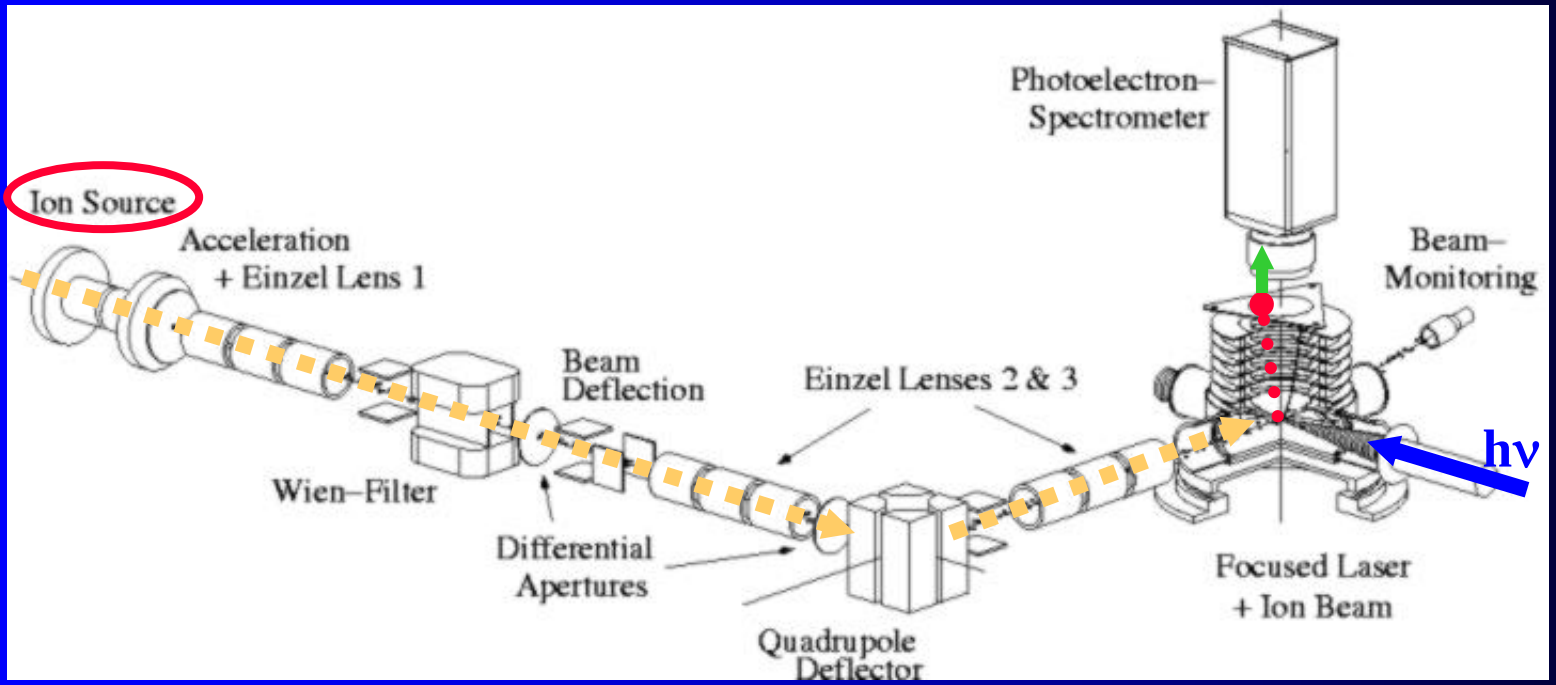

Schematical view of the fast negative ion beam imaging spectrometer. A fast beam of negative hydrogen ions is formed in a hollow cathode discharge ion source, and shaped by an einzel lens 1. The einzel lens 1 collimates the 3 keV beam for optimal passage through the Wien-Filter. The settings of the Wien-Filter also prohibit the passage of electrons co-propagating in the beam into subsequent vacuum chambers. The einzel lenses 2 and 3 serve as an electrostatic telescope to control the collimation and convergence properties of the beam in the interaction chamber. The H- flux corresponds to a current of 100 nA and arrives at the center of the photoelectron spectrometer with a beam waist of 400 m. The 90 degree beam bend in the quadrupole deflector removes neutral hydrogen atoms from the beam. These are produced by collisional detachment with residual gas atoms in the first two vacuum sections where a higher residual pressure prevails. The three vacuum sections are differentially pumped to maintain a residual pressure of 5 10^{-10} mbar in the third section during operation. Intense laser pulses of an energy of 56 J, a pulse length of 250 fs and a wavelength of 2.15 m cross the ion beam under 90 degrees and interact with atomic particles at a repetition rate of 1 kHz. We use a standard Ti:Sapphire laser system with a regenerative amplifier and an optical parametric amplifier (OPA). The outgoing pulses are linearly polarized along the ion beam propagation axis and focused at the center of the ion beam. The heart of our setup is an imaging spectrometer that was first introduced by Helm *et al*, see following box.

Hanspeter Helm Photoelectron spectrometer

The principle of our Photoelectron spectrometer is shown on the right. Electrons produced in the interaction volume by laser irradiation of atoms, ejected in a solid angle of 4 π are mapped onto a 2D position sensitive detector. The projection is achieved by homogeneous or weakly inhomogeneous electrical fields of 80 V/cm^2 in the inner spectrometer region. The detector consists of a Chevron stack of 2 inch diameter high-quality Multi-Channel Plates (MCPs) and a phosphor screen coated by a transparent, conducting gold layer. The amplified signal of an electron impact is drawn onto the phosphor screen by a potential of 2 keV to enhance in phosphorescence yield. This finite-sized light spots are accumulated and integrated by a 12 bit charge-coupled-device (CCD) camera and the data are taken by a frame grabber. The total electron yield is 10^7-10^8 spatially resolved electrons per hour acquisition time. Conventional photoelectron spectroscopy usually requires higher repetition laser systems in order to achieve similar statistics.

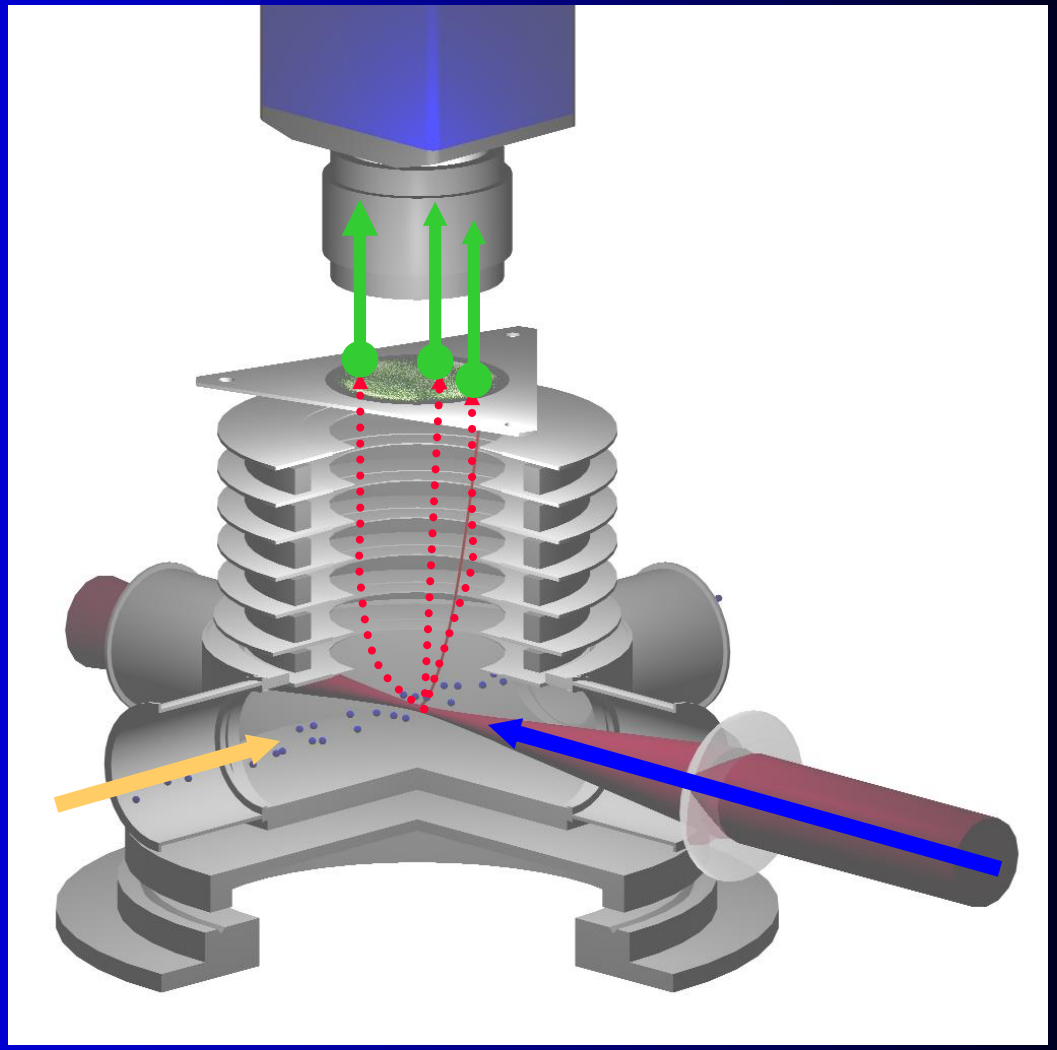

Hanspeter Helm 3D

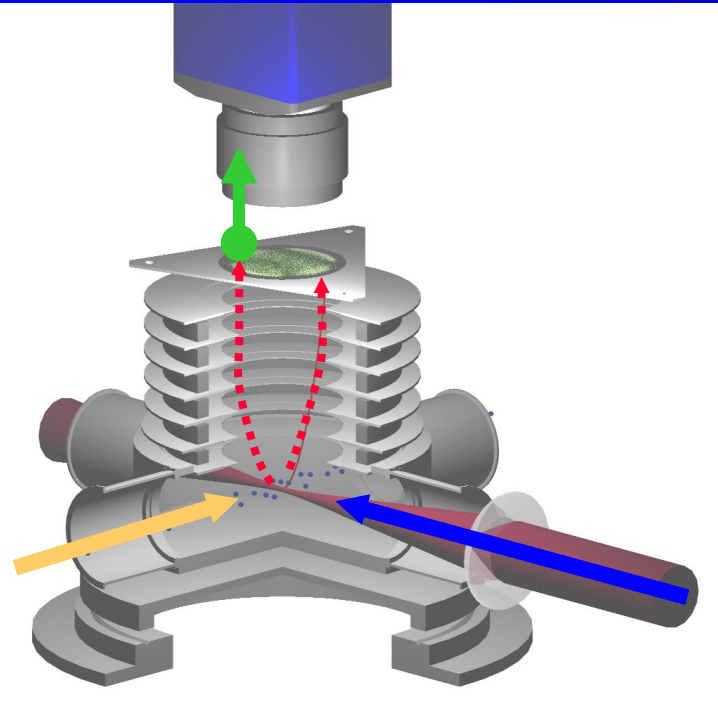

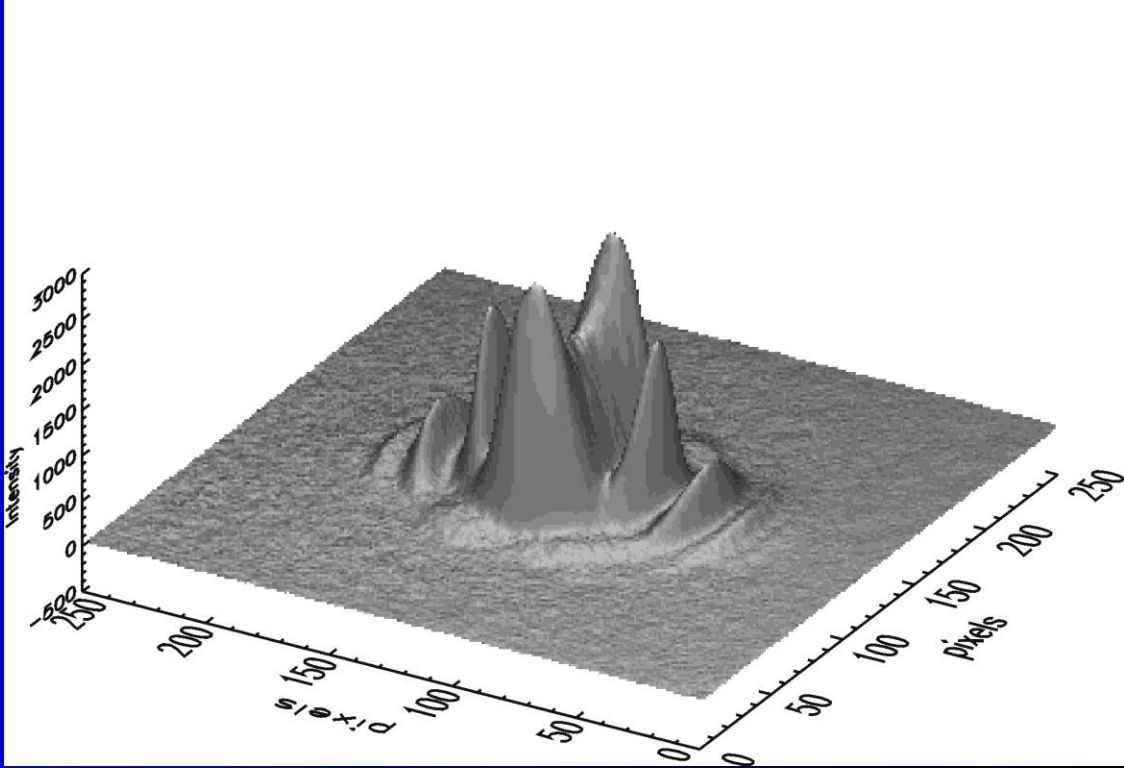

Projection of a continuous 3D electronic wavefunction in momentum space onto a 2D imaging detector. It consists of a mixture of different partial waves and discrete energies. Their energetic spacing corresponds to the photon energy of the laser (EPD Excess Photon Detachment). The modulus of the 3D wavefunction can be reconstructed using numerical inversion routines, since dipole transitions possess an intrinsic cylindrical symmetry.

22 pole trap

THE JOURNAL OF CHEMICAL PHYSICS **130**, 061105 (2009)

Absolute photodetachment cross section measurements of the O^- and OH^- anion

P. Hlavenka, R. Otto, S. Trippel, J. Mikosch,[a] M. Weidemüller,[b] and R. Wester[c]

Absolute total photodetachment cross sections of O^- and OH^- anions stored in a multipole radio frequency trap have been measured using a novel laser depletion tomography method. For OH^- the total cross sections of $8.5(1)_{stat}(3)_{syst}$ and $8.1(1)_{stat}(7)_{syst} \times 10^{-18}$ cm^2, measured at 662 and 632 nm, respectively, were found constant in the temperature range of 8–300 K. The O^- cross sections $5.9(1)_{stat}(2)_{syst}$ and $6.3(1)_{stat}(2)_{syst} \times 10^{-18}$ cm^2 measured at 170 K at 662 and 532 nm, respectively, agree within error estimations with preceding experiments and increase the accuracy of the widely used calibration standard for relative photodetachment measurements of diverse atomic and molecular species. © *2009 American Institute of Physics*. [DOI: 10.1063/1.3080809]

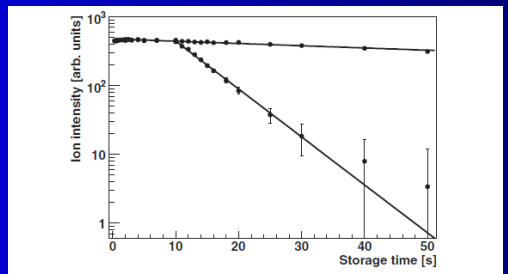

FIG. 2. Measured OH^- ion signal as a function of storage time in the trap. The upper set of points shows the signal in the absence of the photodetachment laser. The lower points show that, when the laser is switched on at 10 s, a fast additional loss channel due to photodetachment appears. The decay rates are obtained from exponential fits (solid lines).

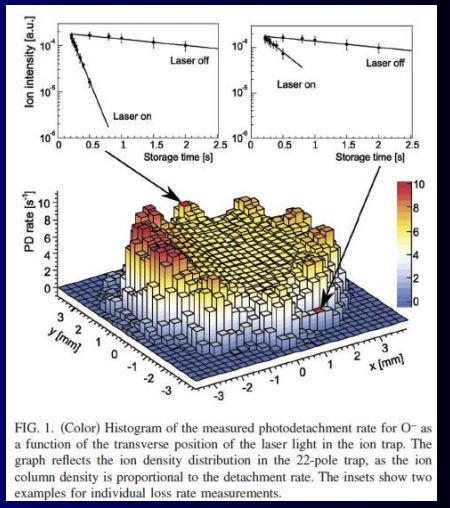

FIG. 1. (Color) Histogram of the measured photodetachment rate for O^- as a function of the transverse position of the laser light in the ion trap. The graph reflects the ion density distribution in the 22-pole trap, as the ion column density is proportional to the detachment rate. The insets show two examples for individual loss rate measurements.

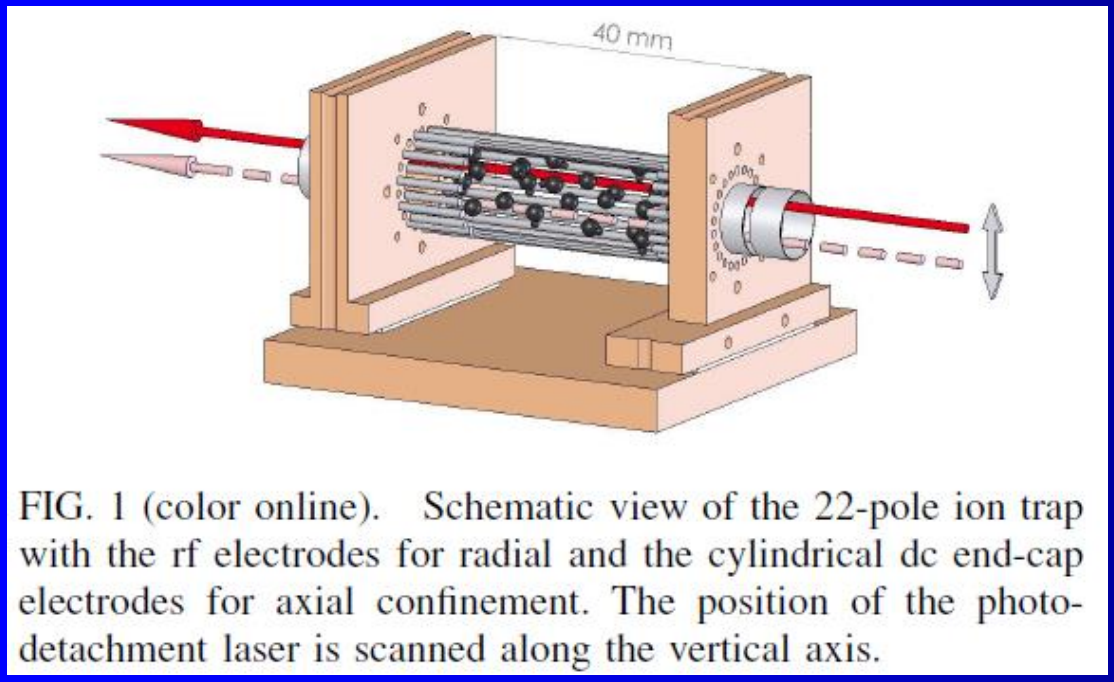

FIG. 1 (color online). Schematic view of the 22-pole ion trap with the rf electrodes for radial and the cylindrical dc end-cap electrodes for axial confinement. The position of the photo-detachment laser is scanned along the vertical axis.

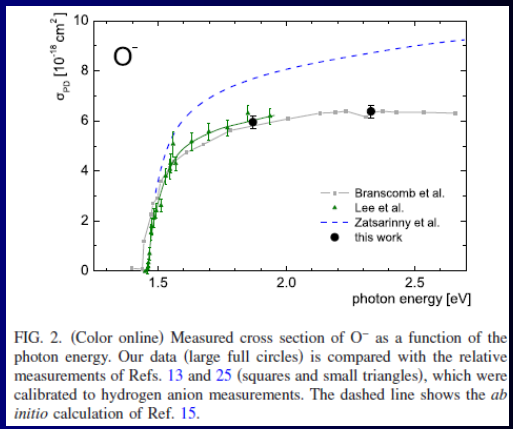

FIG. 2. (Color online) Measured cross section of O^- as a function of the photon energy. Our data (large full circles) is compared with the relative measurements of Refs. 13 and 25 (squares and small triangles), which were calibrated to hydrogen anion measurements. The dashed line shows the *ab initio* calculation of Ref. 15.

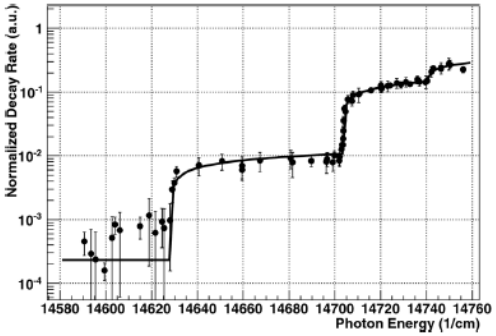

Fig. 3 Photodetachment cross section of OH^- at a trap temperature of 50 K for varying photon energy. The steps in the cross section are due to the opening of loss channels corresponding to the $J = 2$, 1 and 0 rotational states of the anion.

Starting with simple …

$e^-, H^+, H, H^-, H_2^+, H_2, \ldots . H_3^+$

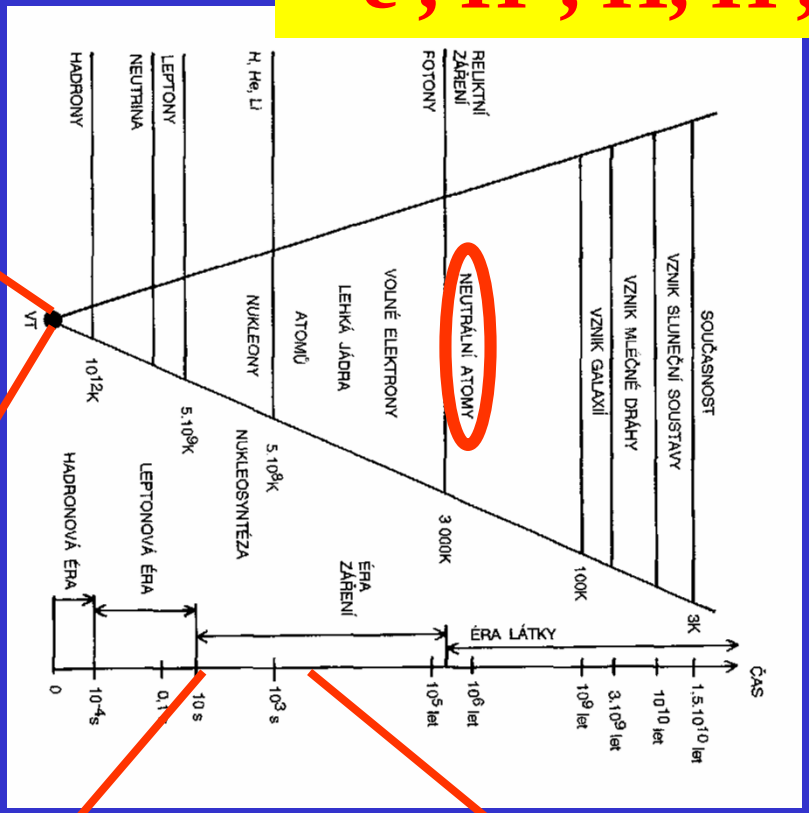

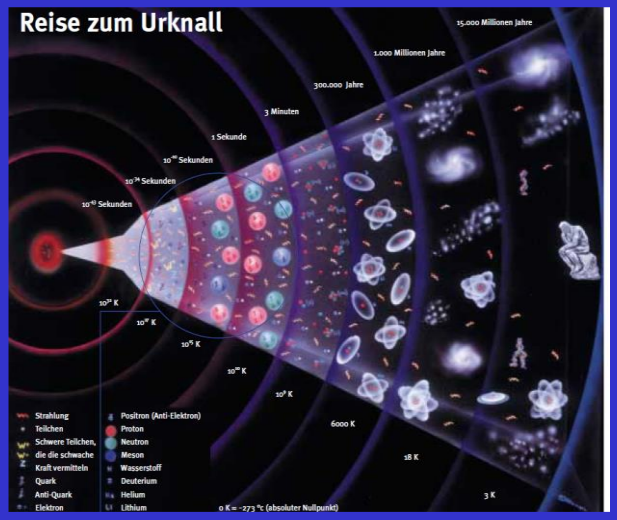

$d + n \longrightarrow H^3 + \gamma$

$H^3 + p \longrightarrow He^4 + \gamma$

$d + p \longrightarrow He^3 + \gamma$

$He^3 + n \longrightarrow He^4 + \gamma$

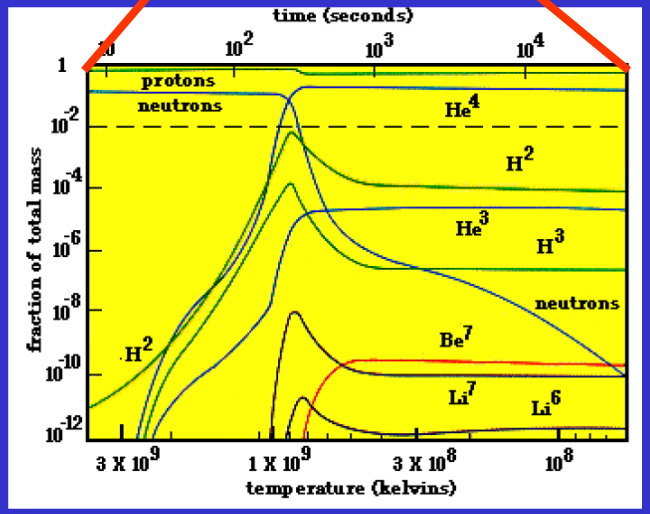

In a diffuse cosmic gas of primordial composition, molecular hydrogen (H2) forms via a sequence of reactions

$H + e^- \rightarrow H^- + \gamma$

$H^- + H \rightarrow H_2 + e^-$

H_2 molecules so formed induce the initial cooling and collapse of primordial clouds.

Hydrogen Chemistry

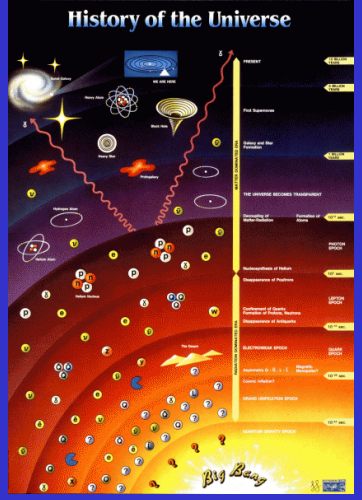

- The formation of H_2^+ and H_2 in the recombination era was first suggested by Saslaw and Zipoy (1967).

Radiative Attachment

$$H + e^- \longrightarrow H^- + \gamma$$

$$H + H^- \longrightarrow H_2 + e^-$$

Associative Detachment

Radiative Association

$$H + H^+ \longrightarrow H_2^+ + \gamma$$

$$H + H_2^+ \longrightarrow H_2 + H^+$$

Charge Transfer

MFF UK
exp. theory

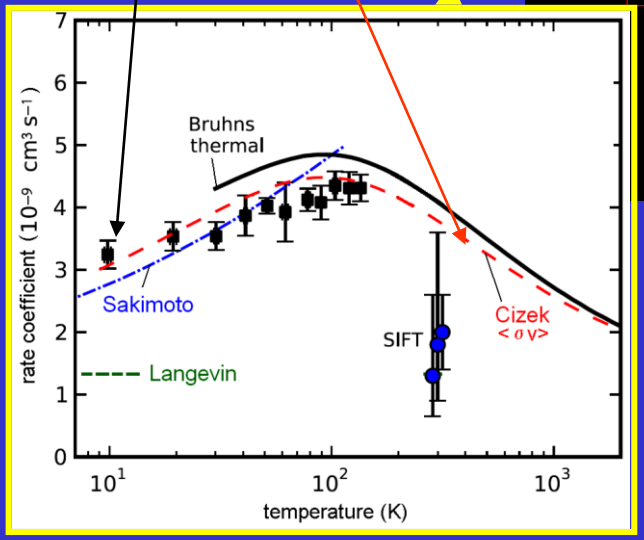

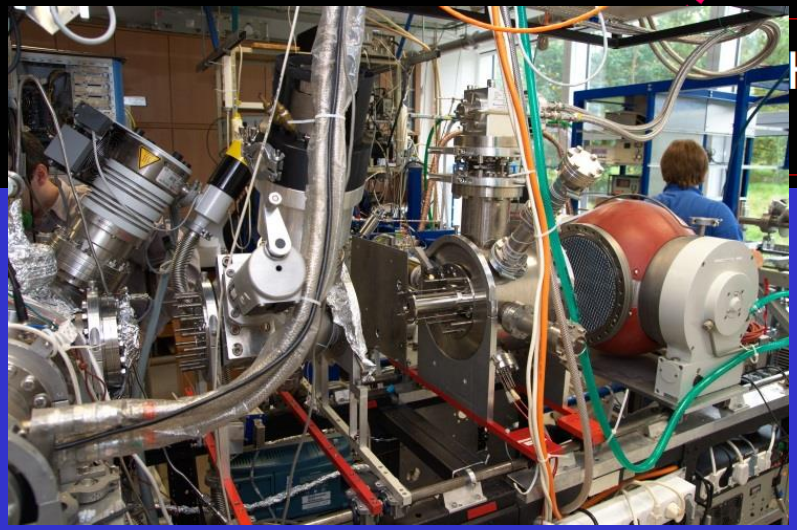

He

Chemie des frühen Universums
Prof. Dr. Dieter Gerlich

Doc. M. Čižek

Gerlich, D; Jusko, P; Roucka, S; Zymak, I; Plasil, R; Glosik, J
Ion Trap Studies of H– + H → H2 + e– Between 10 and 135 K, *Astrophys. J.*, **794** (1): , 2012.

www.sciencemag.org SCIENCE VOL 329 2 JULY 2010

Experimental Results for H_2 Formation from H^- and H and Implications for First Star Formation

H. Kreckel,[1]*† H. Bruhns,[1]‡ M. Čížek,[2] S. C. O. Glover,[3] K. A. Miller,[1] X. Urbain,[4] D. W. Savin[1]

During the epoch of first star formation, molecular hydrogen (H_2) generated via associative detachment (AD) of H^- and H is believed to have been the main coolant of primordial gas for temperatures below 10^4 kelvin. The uncertainty in the cross section for this reaction has limited our understanding of protogalaxy formation during this epoch and of the characteristic masses and cooling times for the first stars. We report precise energy-resolved measurements of the AD reaction, made with the use of a specially constructed merged-beams apparatus. Our results agreed well with the most recent theoretically calculated cross section, which we then used in cosmological simulations to demonstrate how the reduced AD uncertainty improves constraints of the predicted masses for Population III stars.

$$H^- + H \rightarrow H_2^- \rightarrow H_2 + e^-$$

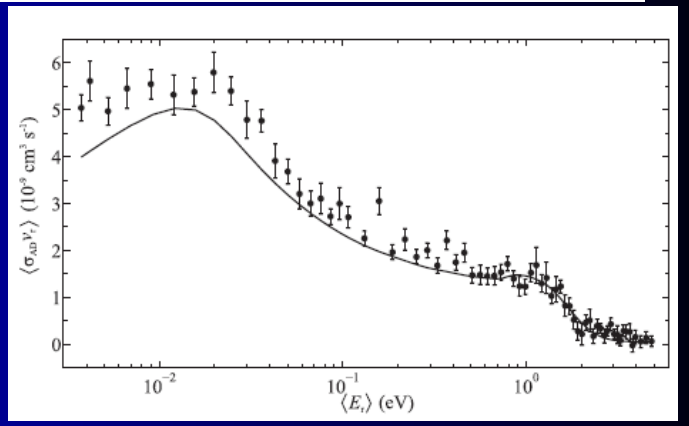

Fig. 1. Schematic of the merged-beams apparatus used to measure the H_2 associative detachment reaction. Infrared laser photons are denoted by ν_{IR}.

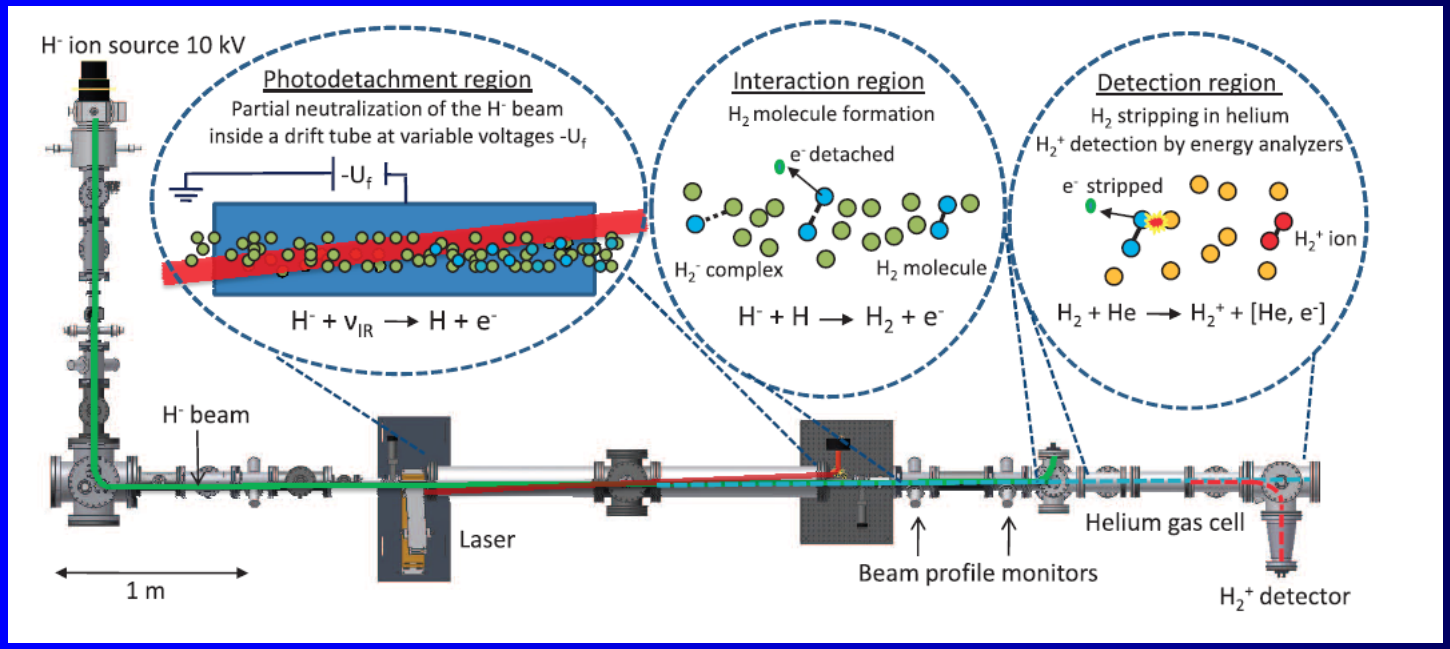

The Astrophysical Journal, 747:1 (6pp), 2012 ???
doi:10.1088/0004-637X/747/1/1

ION TRAP STUDIES OF $H^- + H \rightarrow H_2 + e^-$ BETWEEN 10 AND 135 K

Dieter Gerlich[1,2], Pavol Jusko[1], Štěpán Roučka[1], Illia Zymak[1], Radek Plašil[1], and Juraj Glosík[1]

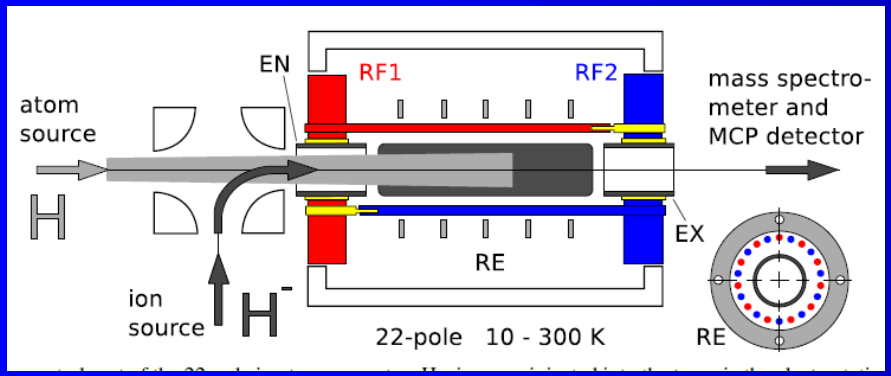

PHYSICAL REVIEW A 86, 032714 (2012)

Isotope effect for associative detachment: $H(D)^- + H(D) \rightarrow H_2(D_2) + e^-$

K. A. Miller,[1] H. Bruhns,[1,*] M. Čížek,[2] J. Eliášek,[2] R. Cabrera-Trujillo,[3] H. Kreckel,[1,†] A. P. O'Connor,[1] X. Urbain,[4] and D. W. Savin[1]

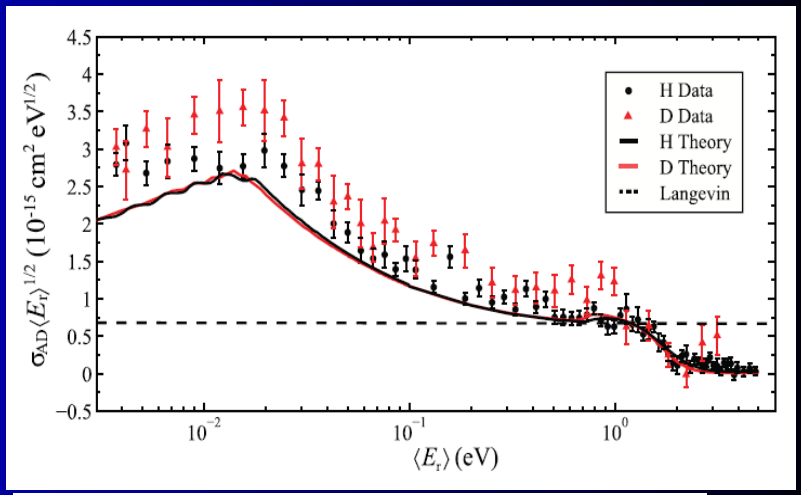

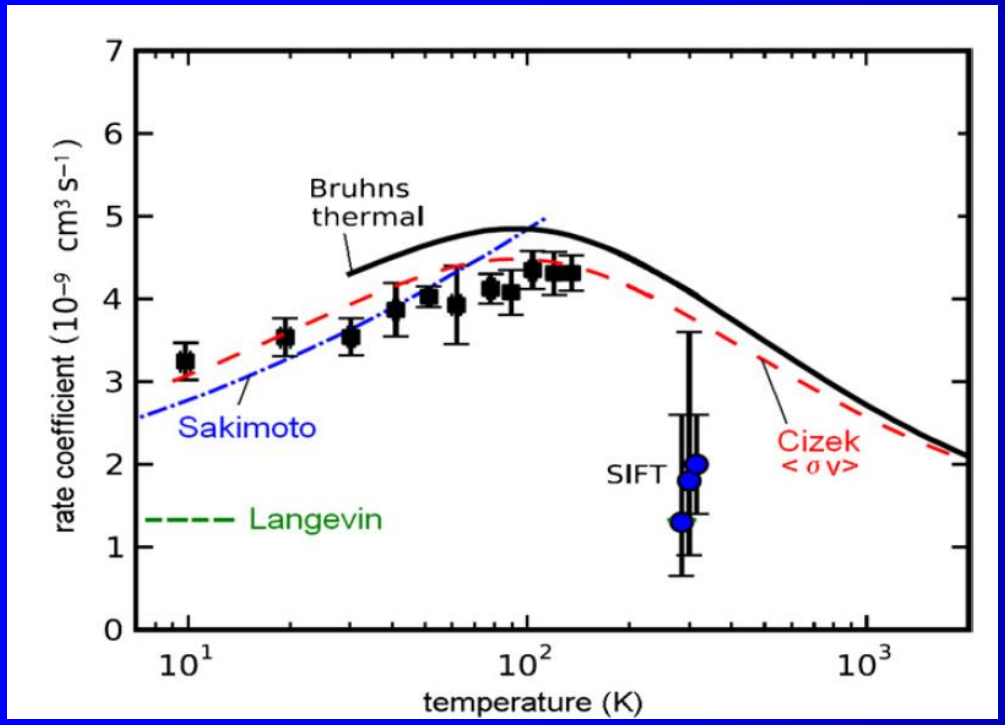

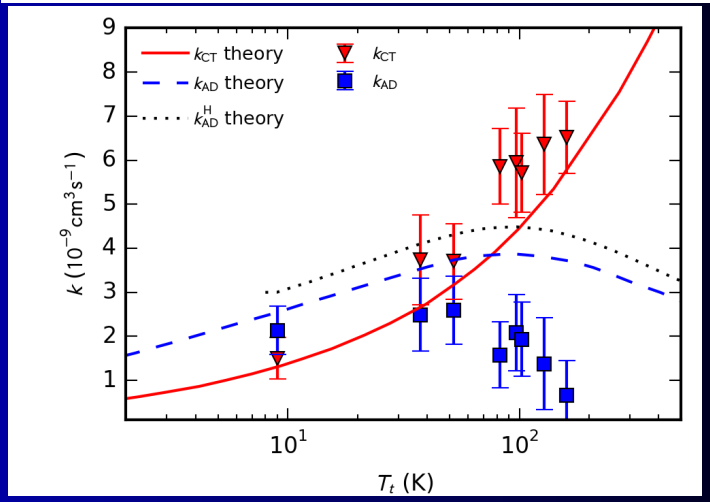

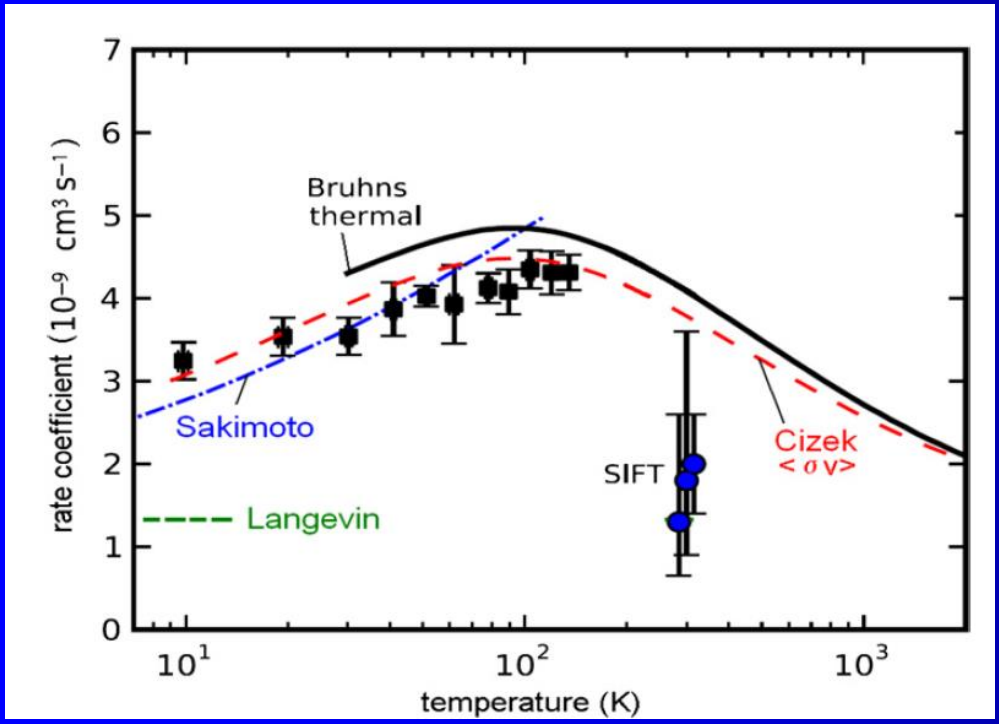
rate coefficient (10^{-9} cm^3 s^{-1})
temperature (K)
Bruhns
thermal
Sakimoto
Langevin
SIFT
Cizek
< σ v>
0
1
2
3
4
5
6
7
10^1
10^2
10^3

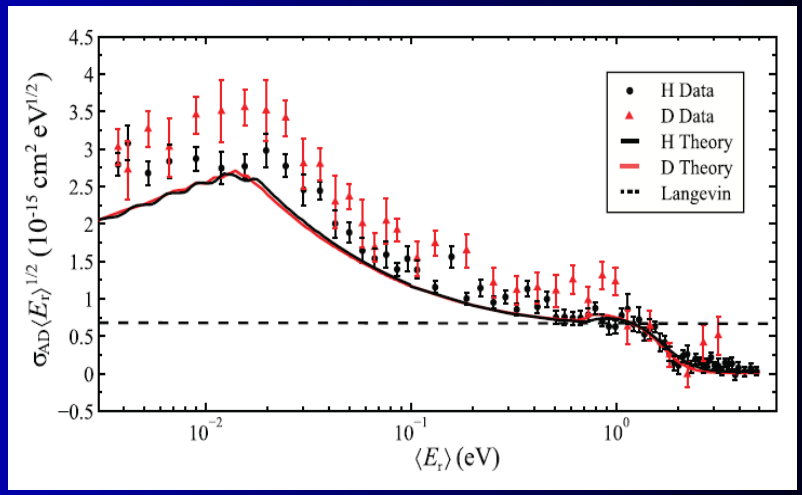
$\sigma_{AD}\langle E_t\rangle^{1/2}$ (10^{-15} cm^2 eV$^{1/2}$)
$\langle E_t\rangle$ (eV)
H Data
D Data
H Theory
D Theory
Langevin
4.5
4
3.5
3
2.5
2
1.5
1
0.5
0
−0.5
10^{-2}
10^{-1}
10^0

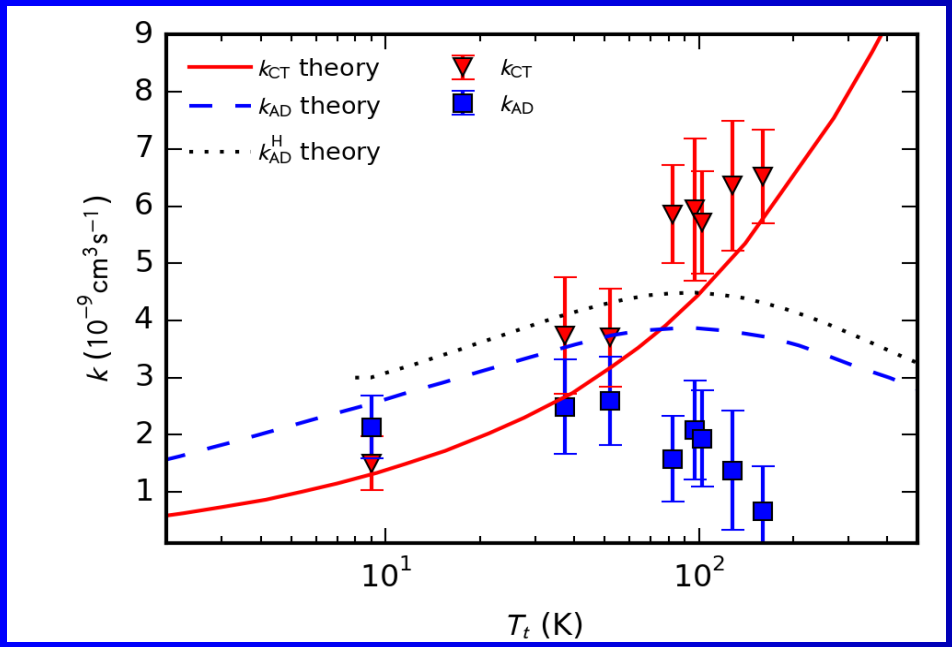
k (10^{-9}cm^{3}s^{-1})
T_t (K)
k_{CT} theory
k_{AD} theory
k^H_{AD} theory
k_{CT}
k_{AD}
1
2
3
4
5
6
7
8
9
10^1
10^2

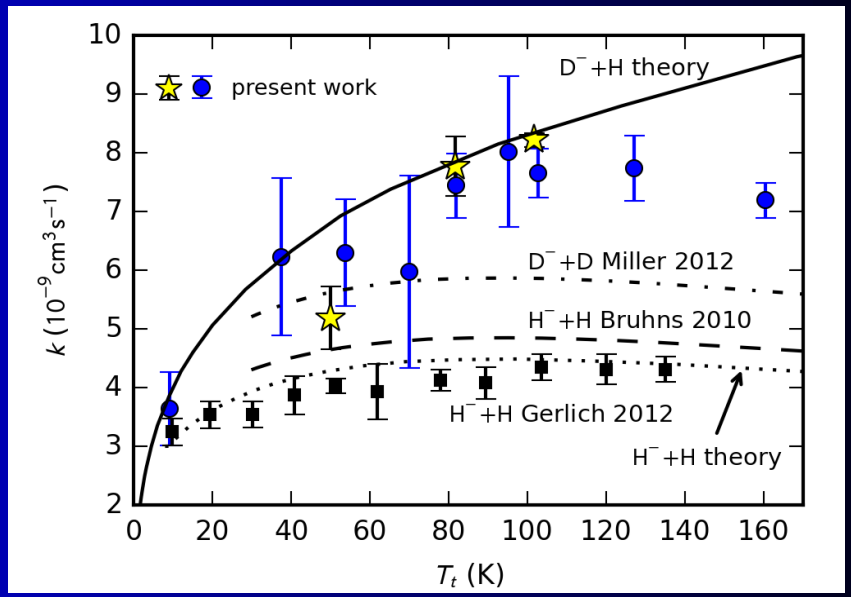
k (10^{-9}cm^{3}s^{-1})
T_t (K)
present work
D$^-$+H theory
D$^-$+D Miller 2012
H$^-$+H Bruhns 2010
H$^-$+H Gerlich 2012
H$^-$+H theory
2
3
4
5
6
7
8
9
10
0
20
40
60
80
100
120
140
160

Ion trap study of $O^- + H_2$ at low temperatures

Roučka, Š.[1]; Jusko, P.[1]; Mulin, D.[1]; Zymak, I.[1]; Plašil, R.[1]; Gerlich, D.[1]; Glosík, J.[1] Čížek, M.[2]; Houfek, K.[2]

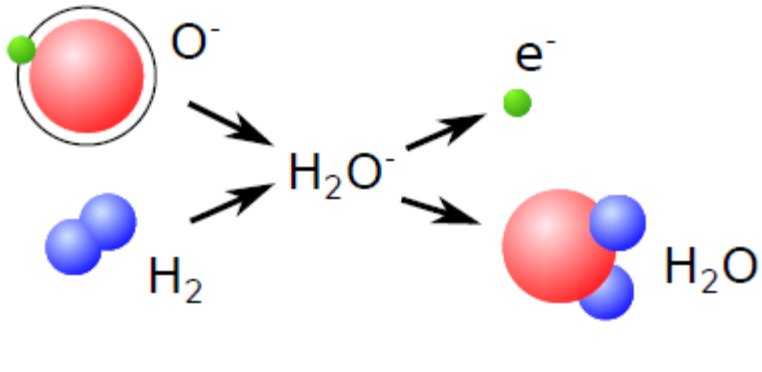

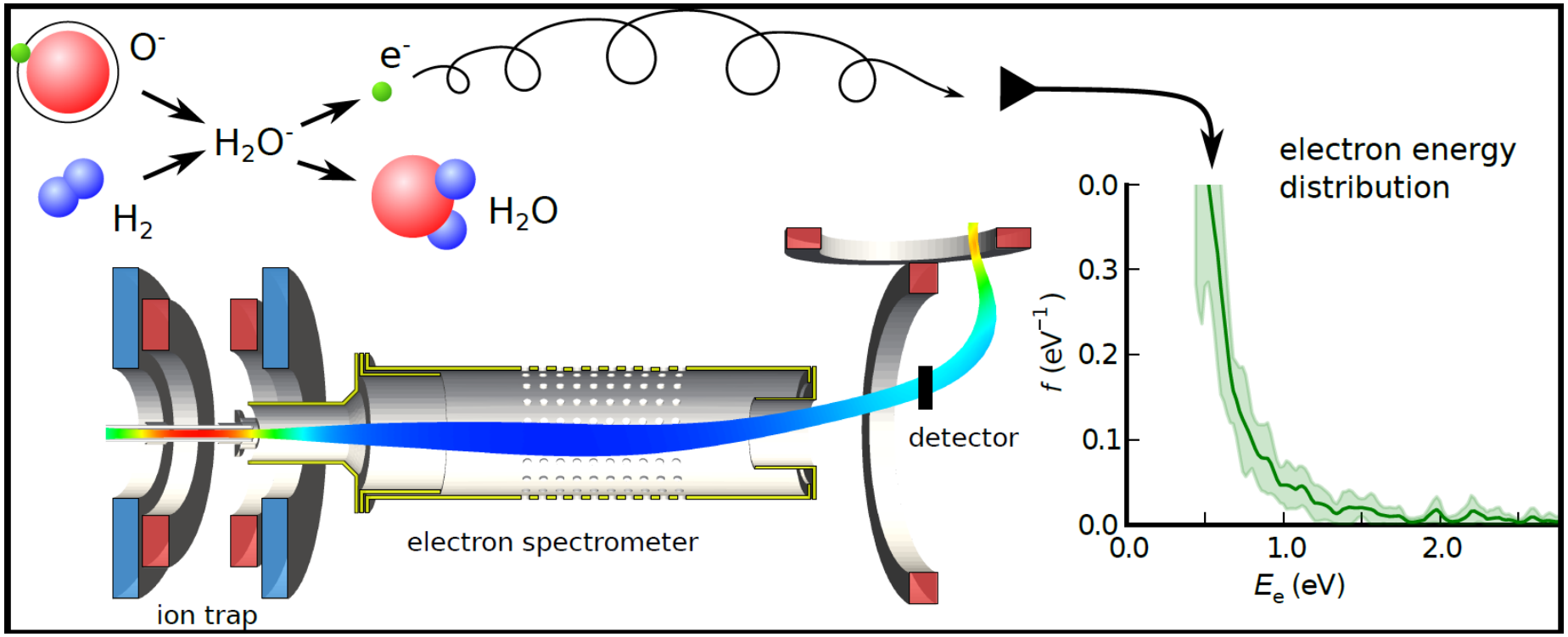
O-
e-
H2O-
H2
H2O
ion trap
electron spectrometer
detector
electron energy distribution
f (eV-1)
Ee (eV)
0.0
0.3
0.2
0.1
0.0
0.0
1.0
2.0

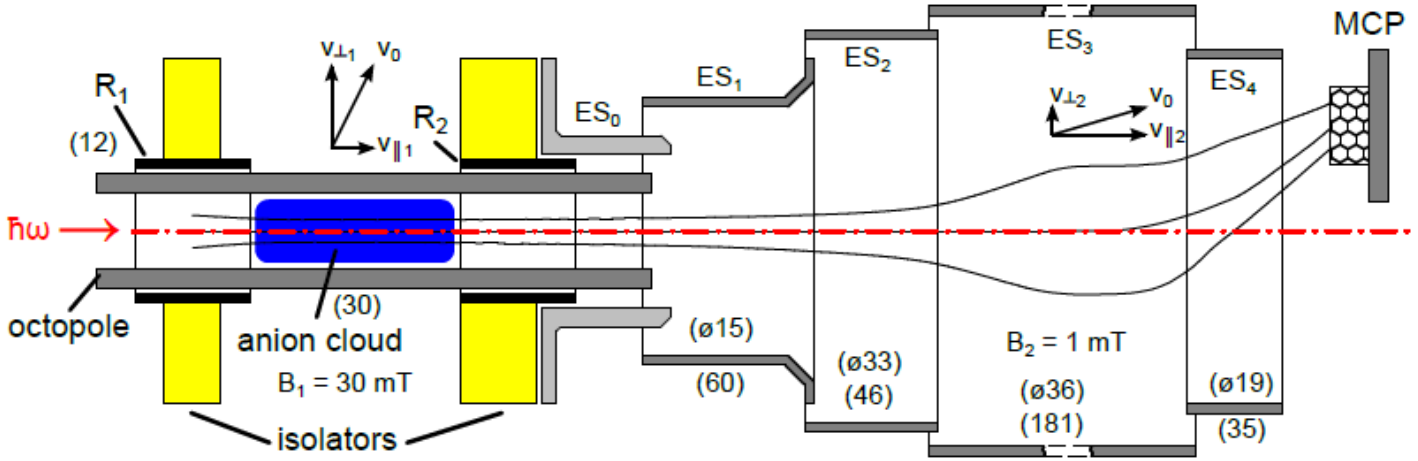
MCP
R1
(12)
v⊥1 v0
v∥1
R2
ES0
ES1
ES2
ES3
v⊥2 v0
v∥2
ES4
ħω
octopole
(30)
anion cloud
B1 = 30 mT
isolators
(ø15)
(60)
(ø33)
(46)
B2 = 1 mT
(ø36)
(181)
(ø19)
(35)

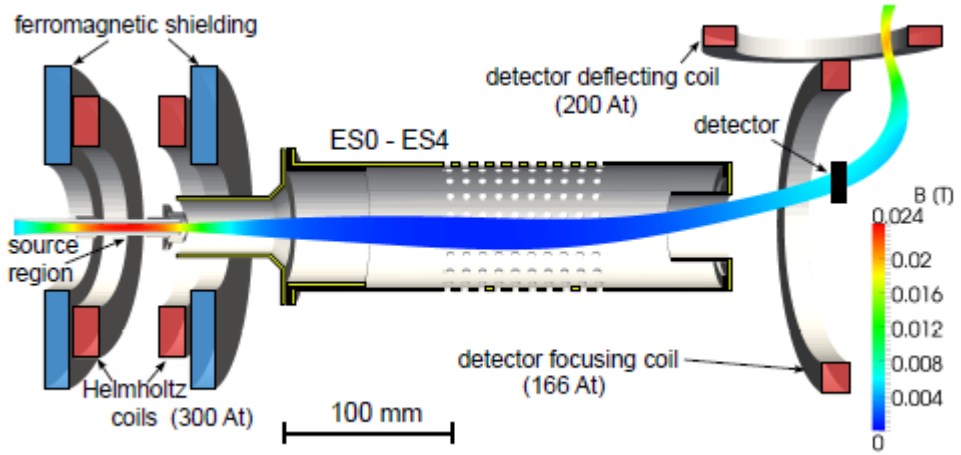
ferromagnetic shielding
detector deflecting coil
(200 At)
detector
ES0 - ES4
B (T)
0.024
0.02
0.016
0.012
0.008
0.004
0
source
region
Helmholtz
coils (300 At)
100 mm
detector focusing coil
(166 At)

ES-MPT

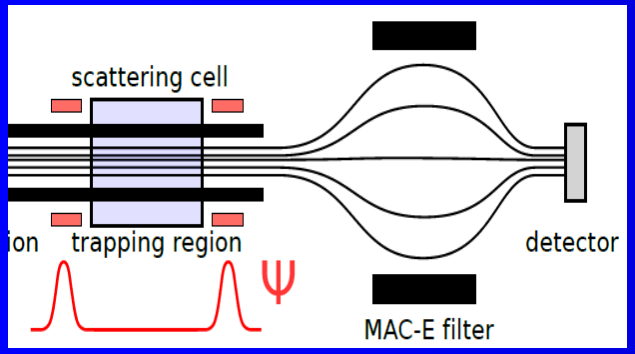

$$O^- + H_2 \Rightarrow H_2O + e^-$$

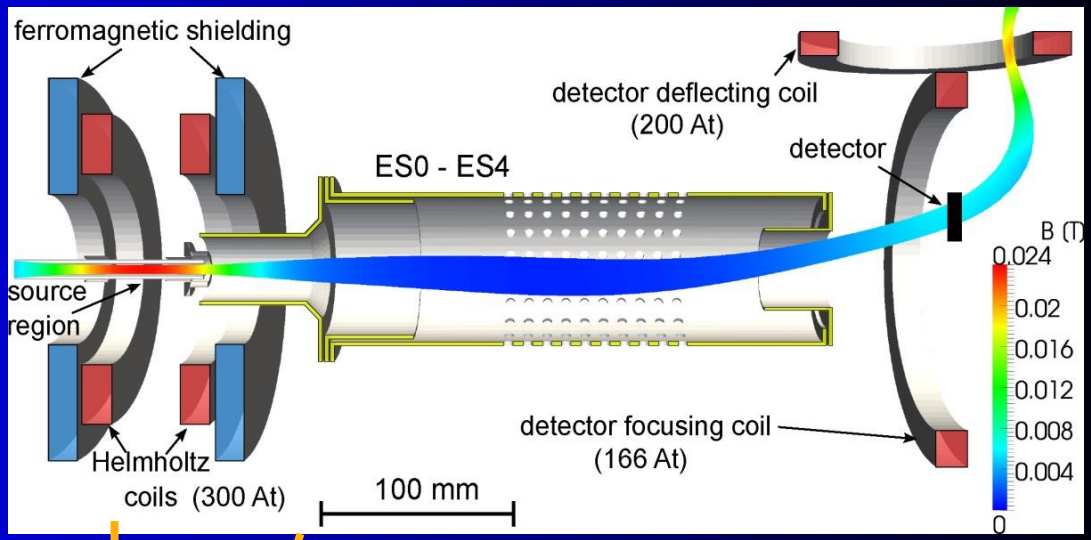

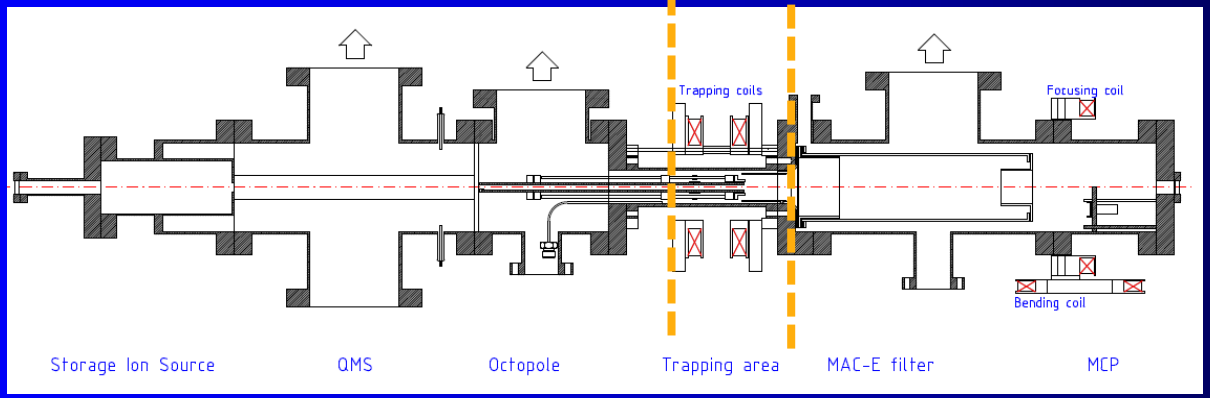

photodetachment

Experimental techniques – ion traps

22PT – 22-Pole Trap

- Measurement of reaction rate coefficients
- Temperature range 10–300 K

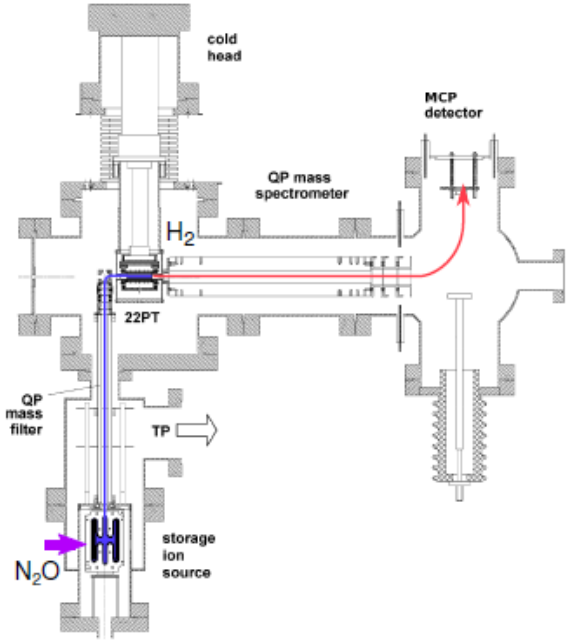

ES-MPT – Electron Spectrometer with MultiPole Trap

- Energy distribution of detached electrons
- Octopole
- Temperature 300 K

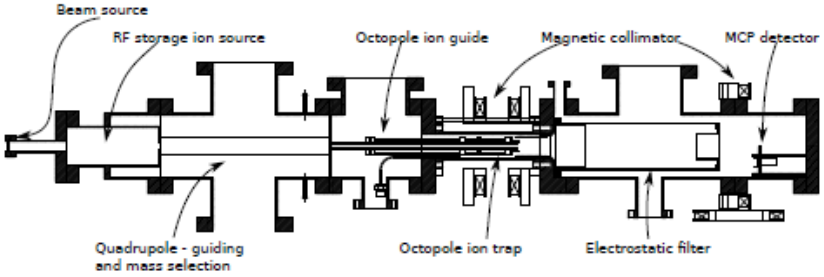

ES-MPT

Electron Spectrometer with MultiPole Trap

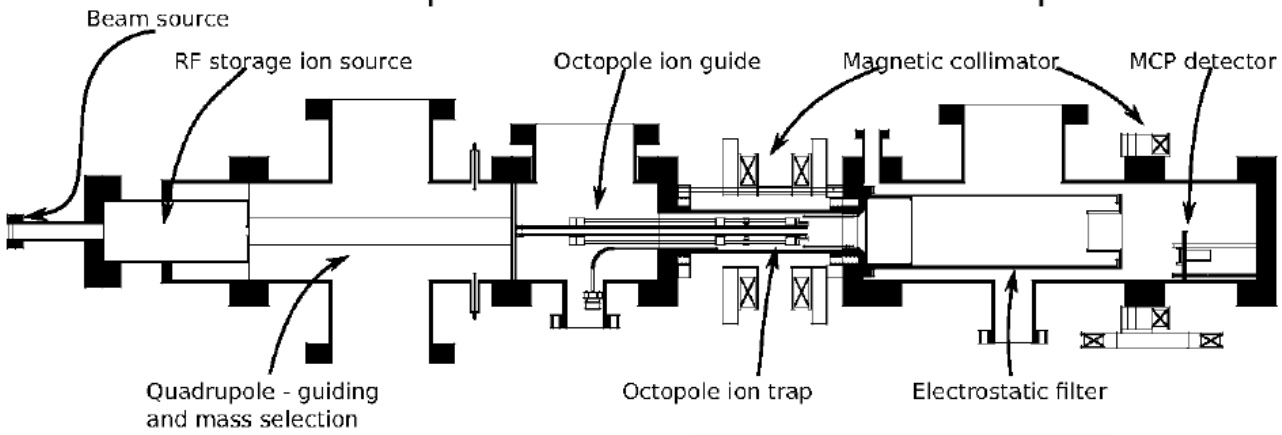

- Extraction of electrons produced in the trap
- Collimation by mag. field and energy analysis by retarding electric field

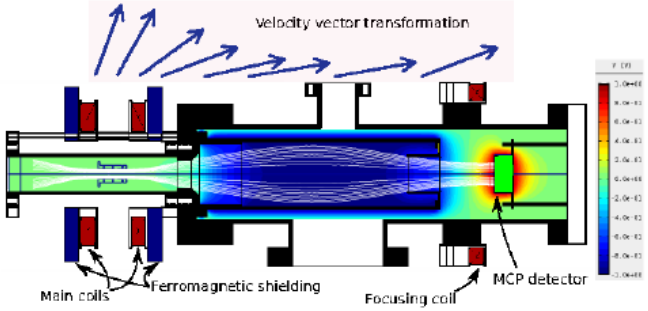

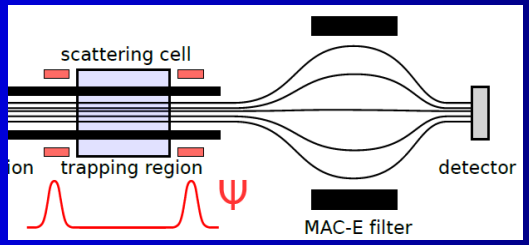

name

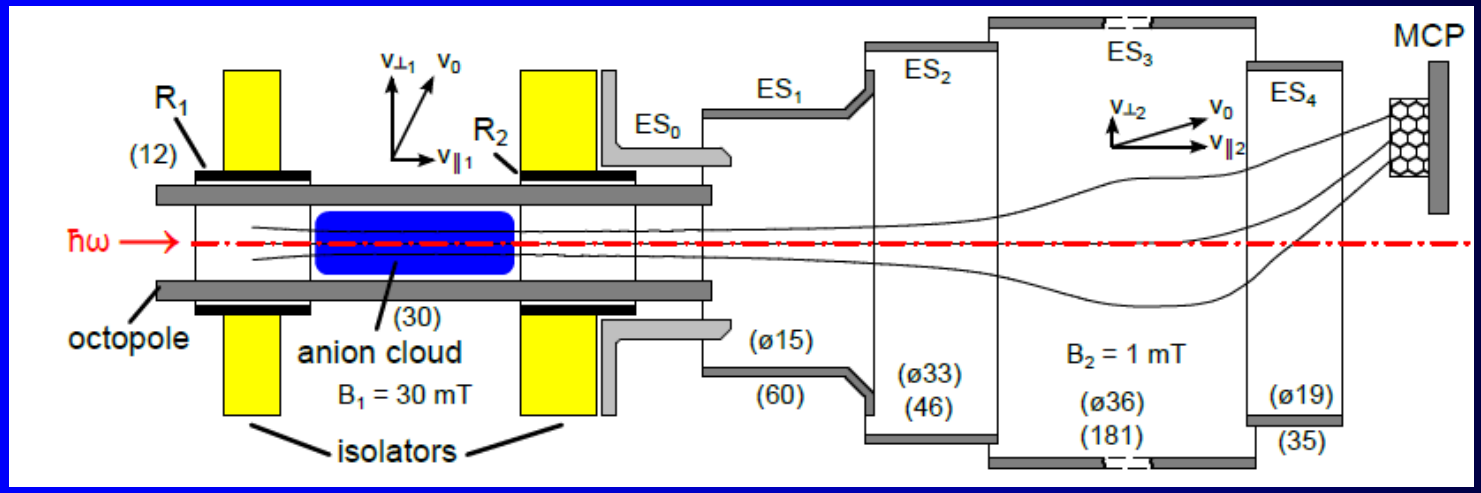
R1
(12)
v⊥1 v0
v∥1
R2
ES0
ES1
ES2
ES3
v⊥2 v0
v∥2
ES4
MCP
ħω
octopole
(30)
anion cloud
B1 = 30 mT
isolators
(ø15)
(60)
(ø33)
(46)
B2 = 1 mT
(ø36)
(181)
(ø19)
(35)

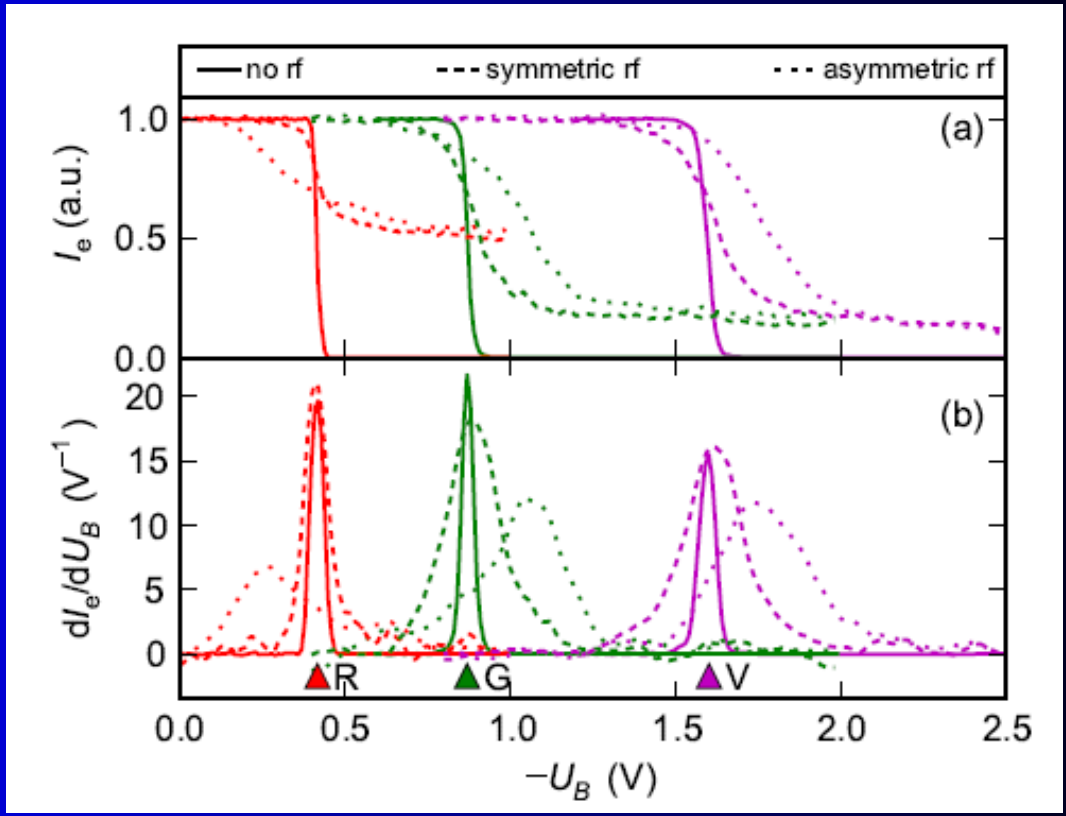
no rf
symmetric rf
asymmetric rf
(a)
(b)
Ie (a.u.)
dIe/dUB (V−1)
R
G
V
−UB (V)

Testovací měření ES-MPT

Rozlišení spektrometru — Spektrum thermionicky emitovaných elektronů

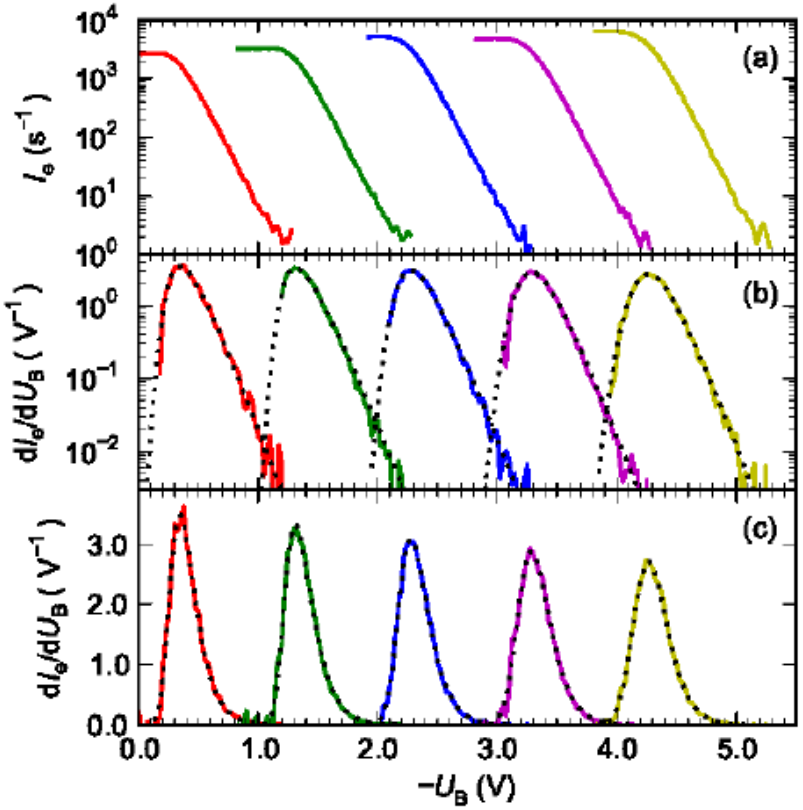

Vliv RF pole pasti — Spektrum elektronů z photodetachmentu O^-

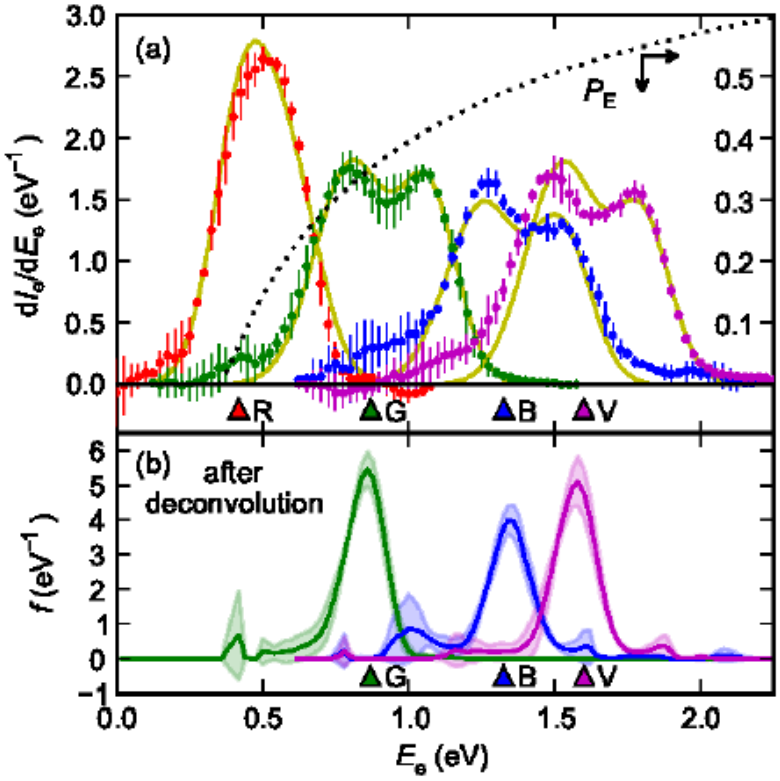

Spectra of detached electrons (ES-MPT instrument)

$$O^- + H_2 \xrightarrow{k_1} H_2O(E_i) + e^-(E_k)$$

- Momentum conservation, Franck-Condon
- Produced molecule is highly excited

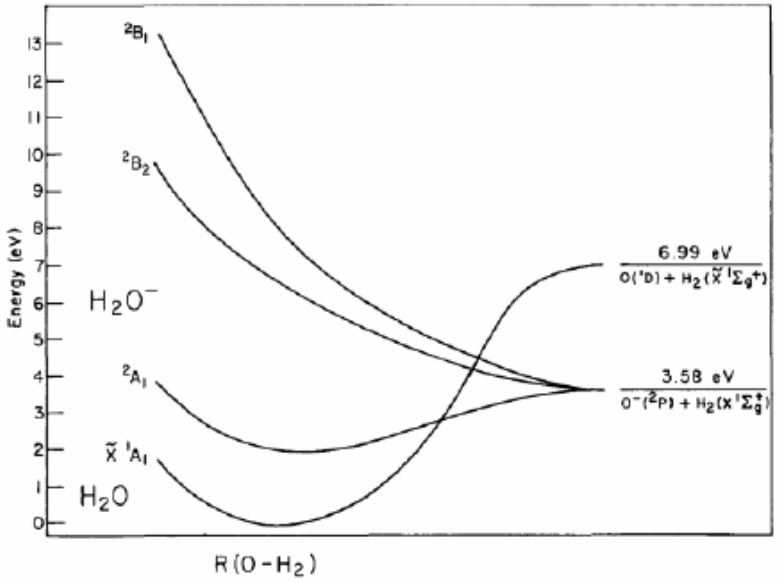

[Claydon et al. JCP 1971]

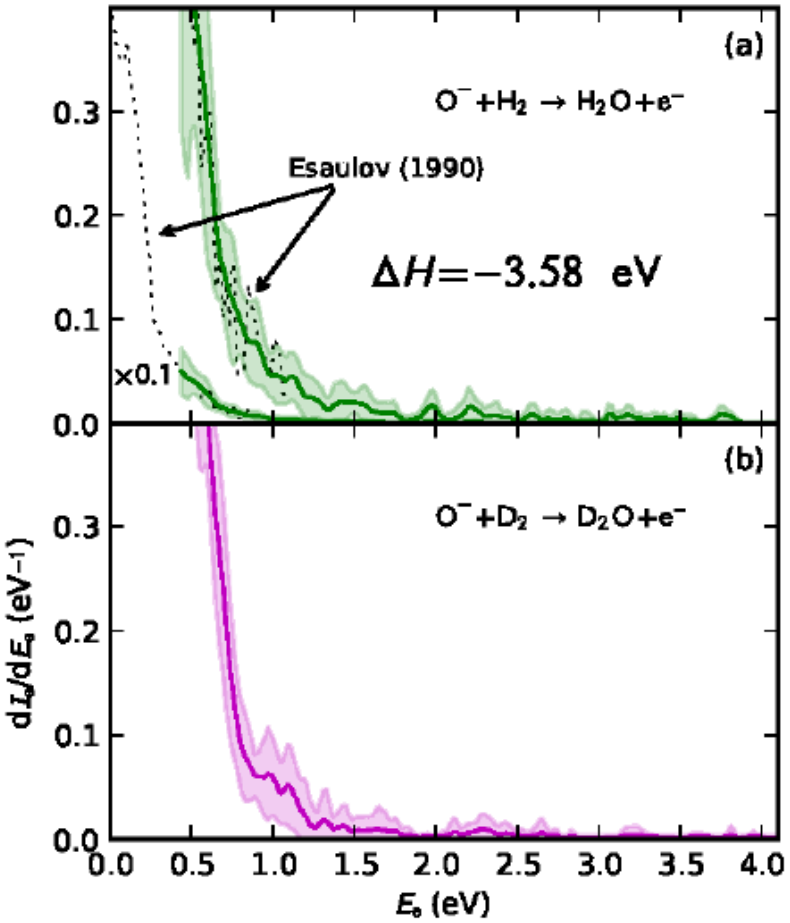

Published in [Jusko, Roučka, Plašil, Glosík; IJMS, 2013]

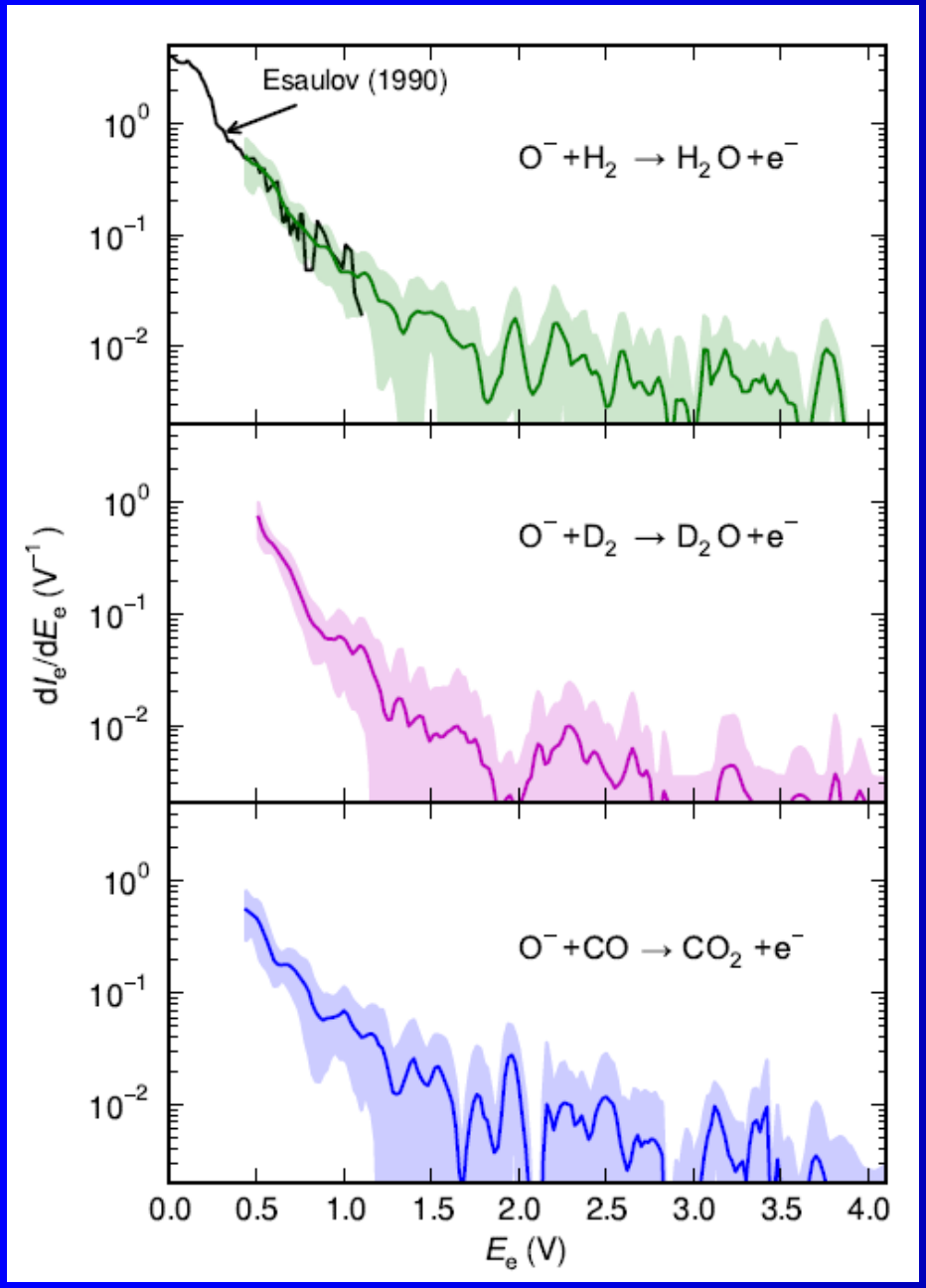

$$O^- + H_2 \rightarrow H_2O + e + 3.6\ eV$$

$$\rightarrow OH^- + H + 0.3\ eV$$

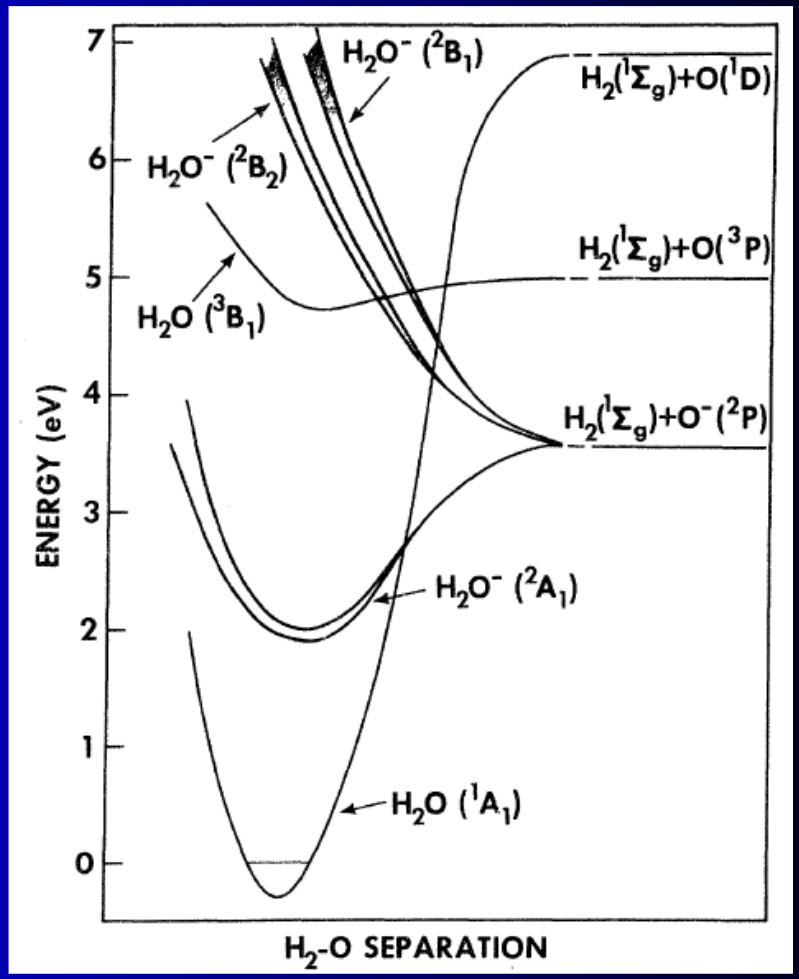

Thanks

name

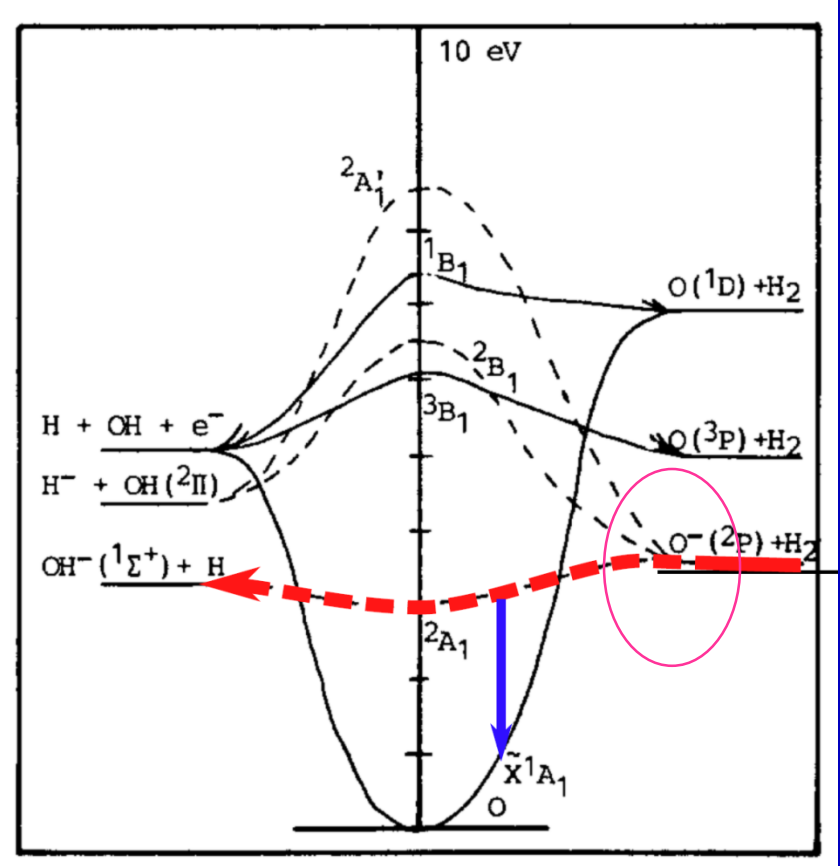
10 eV
$^2A_1'$
$^1B_1$
$^2B_1$
$^3B_1$
$^2A_1$
$\tilde{X}^1A_1$
O
O(^{1}D) +H$_2$
O(^{3}P) +H$_2$
O$^-$(^{2}P) +H$_2$
H + OH + e$^-$
H$^-$ + OH($^2\Pi$)
OH$^-$($^1\Sigma^+$) + H

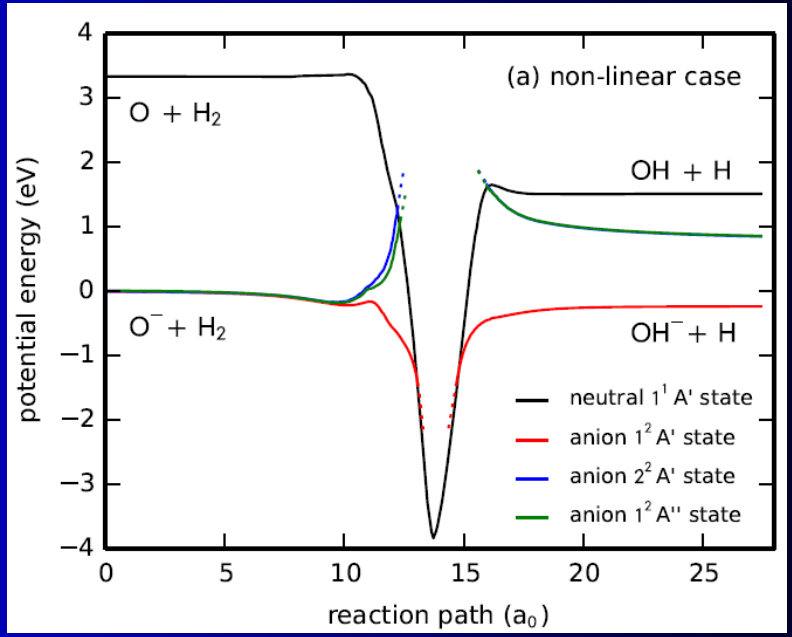
(a) non-linear case
O + H$_2$
OH + H
O$^-$ + H$_2$
OH$^-$ + H
neutral 1^{1}A' state
anion 1^{2}A' state
anion 2^{2}A' state
anion 1^{2}A'' state
potential energy (eV)
reaction path (a$_0$)

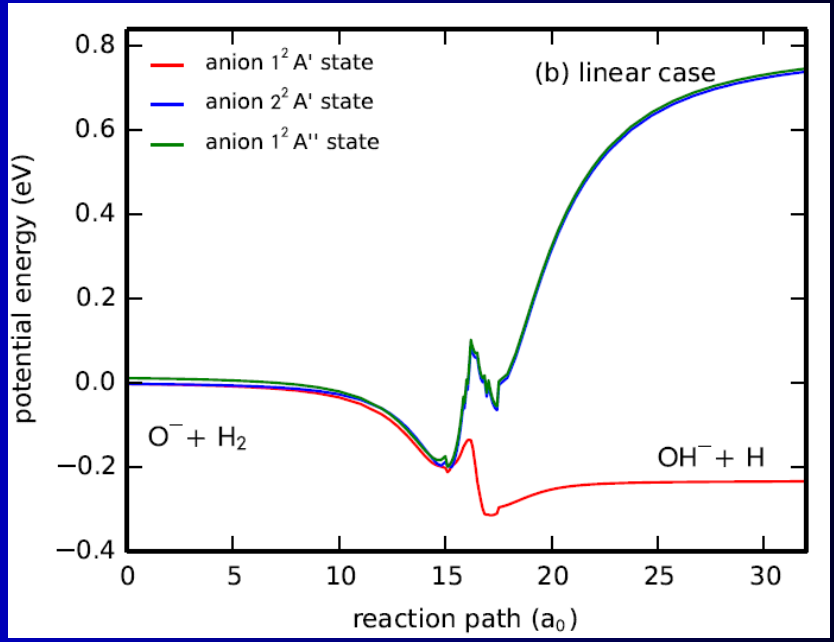
(b) linear case
anion 1^{2}A' state
anion 2^{2}A' state
anion 1^{2}A'' state
O$^-$ + H$_2$
OH$^-$ + H
potential energy (eV)
reaction path (a$_0$)

Interaction of O^- and H_2 at low temperatures

P. Jusko,[1] Š. Roučka,[1,a)] D. Mulin,[1] I. Zymak,[1] R. Plašil,[1] D. Gerlich,[1] M. Čížek,[2] K. Houfek,[2] and J. Glosík[1]

$$O^- + H_2 \xrightarrow{k_1} H_2O + e^-, \qquad \Delta H = -3.58\ \text{eV} \qquad (1)$$

rogen atom transfer

$$O^- + H_2 \xrightarrow{k_2} OH^- + H, \qquad \Delta H = -0.28\ \text{eV}, \qquad (2)$$

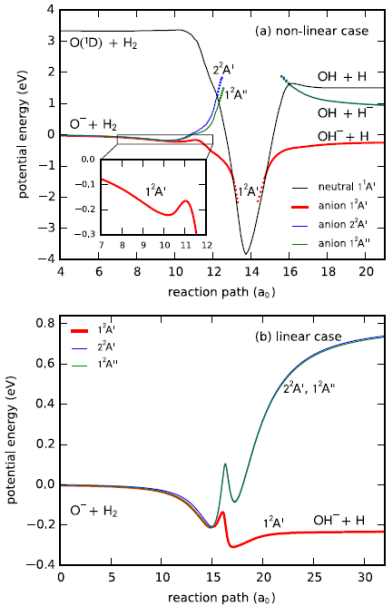

FIG. 3. Panel (a)—PES of H_2O^- and H_2O along the minimum energy path going from $O^- + H_2$ to $OH^- + H$ on the $1^2A'$ PES. The anionic curves in the autodetachment region, where they are above the neutral PES, are indicated by points. The local minimum of the $1^2A'$ PES, where some metastable H_2O^- states may exist, is magnified in the inset. In Panel (b), the path is constrained to the linear geometry, $\theta = 0°$. In this case, the potential energy of the neutral H_2O is too high—outside of the graph.

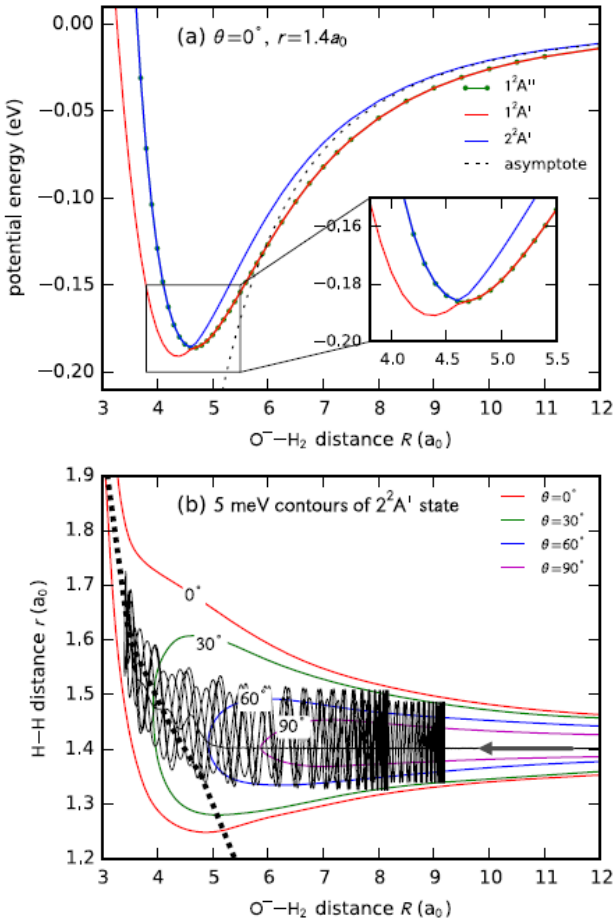

FIG. 4. Panel (a)—Section of the three potential energy surfaces for $\theta = 0°$, $r = 1.4014a_0$, showing the attraction of O^- and H_2 and the conical intersection at $4.6a_0$, coupling them. The sum of quadrupole and polarization potential is marked with a dotted line. Panel (b)—Typical classical trajectory on the $2^2A'$ PES for a collision energy of 5 meV projected on the $\theta = 0°$ plane. The conical intersection at $\theta = 0°$ is marked by the dashed line. The equipotential lines for $V = 5$ meV are also shown for the indicated values of θ. This picture shows a section of a trajectory with a duration of 700 vibrational periods of H_2. Most trajectories remain trapped for typically 10^4–10^5 vibrational periods, passing beyond the conical intersection several hundred times.

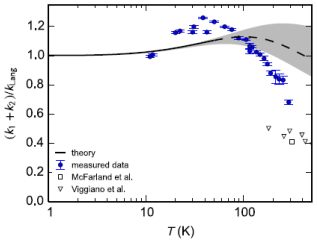

FIG. 5. Comparison of the measured total reaction rate coefficients $k_1 + k_2$ with the values calculated with the 1D capture model described in the text. The data are normalized with the Langevin capture rate coefficient. Sensitivity test of the model is indicated with the gray area. The part of the theoretical curve which is significantly sensitive to the parameters of the absorption potential, is shown as a dashed line. Experimental results of McFarland *et al.*[10] and Viggiano *et al.*[12] are shown for comparison.

Table 2
Total reaction rate coefficient estimated from temporal evolutions of electron production at 300 K (see Fig. 10). Only the statistical error is shown. The results are accurate within a factor of 2 due to systematic errors.

Reaction	k (this work) (10^{-10} cm^3 s^{-1})	k (McFarland et al. [34]) (10^{-10} cm^3 s^{-1})
$O^- + H_2$	5.4 ± 0.2	6.4
$O^- + D_2$	3.2 ± 0.1	4.6

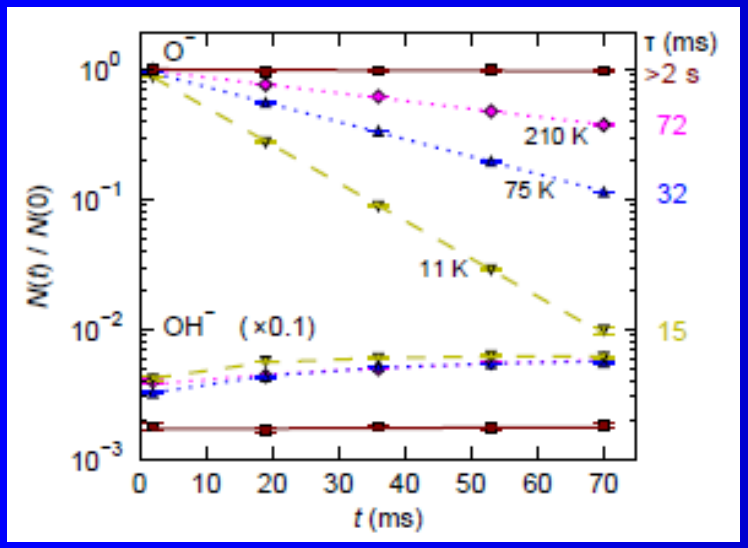
O⁻
τ (ms)
>2 s
72
32
15
210 K
75 K
11 K
OH⁻ (×0.1)
N(t) / N(0)
t (ms)

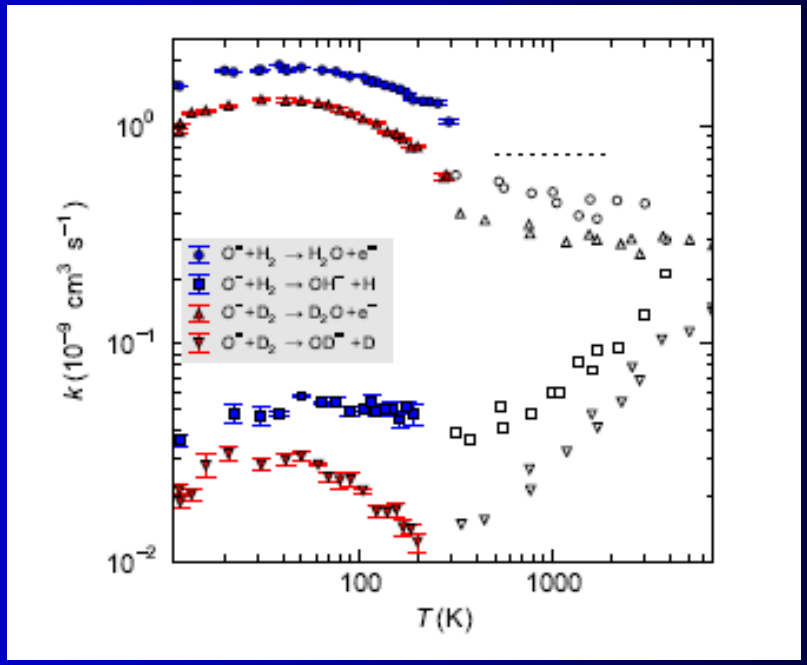
O⁻+H₂ → H₂O+e⁻
O⁻+H₂ → OH⁻ +H
O⁻+D₂ → D₂O+e⁻
O⁻+D₂ → OD⁻ +D
k (10⁻⁹ cm³ s⁻¹)
T (K)

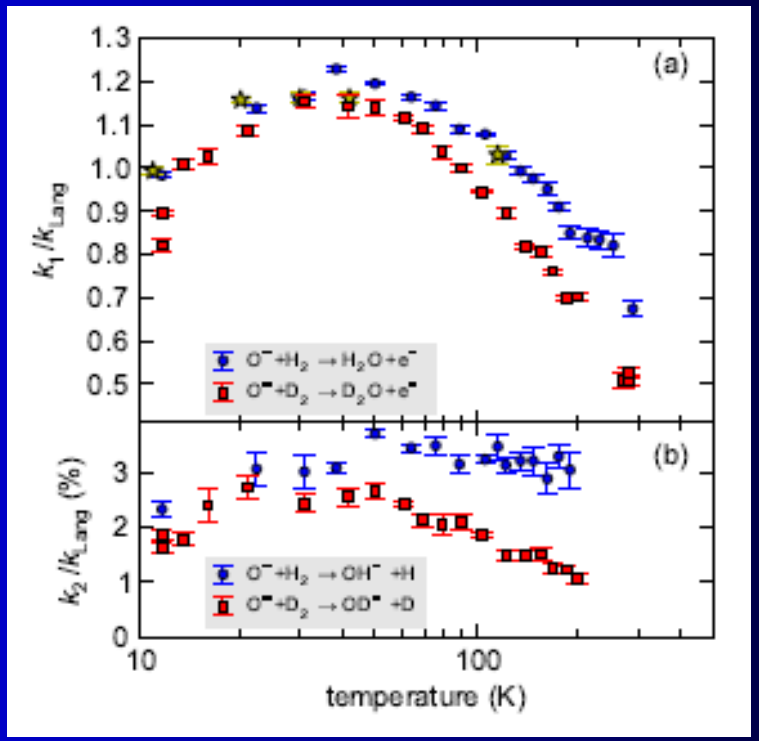
(a)
(b)
O⁻+H₂ → H₂O+e⁻
O⁻+D₂ → D₂O+e⁻
O⁻+H₂ → OH⁻ +H
O⁻+D₂ → OD⁻ +D
temperature (K)

theory